RadioAstron space VLBI imaging of the radio galaxy 3C 84 at 22 GHz

Petra Benke

Supervisors:

Docent Tuomas Savolainen

Metsähovi Radio Observatory & Department of Electronics and Nanoengineering

Aalto University

Prof. Peter H. Johansson

Deparment of Physics

University of Helsinki

Master's Thesis

Astrophysical Sciences

Particle Physics and Astrophysical Sciences

Faculty of Science

University of Helsinki

Finland

May, 2021

HELSINGIN YLIOPISTO
HELSINGFORS UNIVERSITET
UNIVERSITY OF HELSINKI
MATEMAATTIS-LUONNONTIETEELLINEN TIEDEKUNTA
MATEMATISK-NATURVETENSKAPLIGA FAKULTETEN
FACULTY OF SCIENCE

Tiedekunta – Fakultet – Faculty	Koulutusohjelma – Utbildningsprogram – Degree programme
Faculty of Science	Master's Programme in Particle Physics and Astophysical Sciences

Opintosuunta – Studieinrikting – Study track

Astrophysical Sciences

Tekijä – Författare – Author

Petra Benke

Työn nimi – Arbetets titel – Title

RadioAstron space-VLBI imaging of the radio galaxy 3C 84 at 22 GHz

Työn laji – Arbetets art – Level	Aika – Datum – Month and year	Sivumäärä – Sidoantal – Number of pages
Master	August 2021	60

Tiivistelmä – Referat – Abstract

Active galactic nuclei (AGN) are one of the most powerful sources of the luminous Universe. Radio-loud AGN exhibit prominent relativistic outflows known as jets, whose synchrotron radiation can be detected in the radio domain. The launching, evolution and variable nature of these sources is still not fully understood. We study 3C 84, because its proximity, brightness and the intermittent nature of its jet makes it a good target to investigate these open questions of the AGN phenomena.

3C 84 (optical counterpart: NGC 1275) is a Fanaroff-Riley type I radio galaxy, located in the Perseus cluster at $z = 0.0176$. Due to its close proximity, 3C 84 has been a favourable target for observations throughout the whole electromagnetic spectrum, especially for ones in the radio domain. Its most recent activity took started 2003, when a new component emerged from the core in the form of a restarted parsec-scale jet. This provided a rare opportunity to study the formation and evolution of a jet (see Nagai et al. 2010, 2014, 2017 and Suzuki et al. 2012). The highest resolution results were obtained by Giovannini et al. (2018), who imaged the source with the Global VLBI Network together with the Space Radio Telescope, RadioAstron. This enabled them to capture the limb-brightened structure of the restarted jet and measure its collimation profile from ~350 gravitational radii.

In this work I present the 22 GHz RadioAstron observations carried out 3 years later, in a similar configuration, but with a significantly different sampling of the space baselines than the ones presented in Giovannini et al. (2018). The calibration was carried out in the Astronomical Image Processing System (AIPS), whereas imaging was done in Difmap (Shepherd 1997). The aim of this thesis work was to obtain a high-resolution image of the source, measure the collimation profile of the restarted jet, and compare the results with those of Giovannini et al. (2018) and verify them, if possible.

Comparing the images of the two epochs, they both show a similar structure, with the radio core, a diffuse emission region (C2), and the hotspot (C3) at the end of the restarted jet. Edge-brightening is confirmed in the jet and the counter-jet. However, the jet has advanced ~1 mas, corresponding to the velocity of $0.946c$. C3 has moved from the center of the feature to the jet head, indicating an interaction between the jet and the clumpy external medium (Kino et al. , 2018 and Nagai et al., 2017). The base of the jet has also changed between the observation, approximately by ~20°. In the light that in the 1990s the jet pointed towards C2, then swinged westwards when the jet emerged (Suzuki et al., 2012 and Giovannini et al., 2018), and on the 2016 image has moved towards its initial position. This suggest a precessing jet, observed and modeled by Dominik et al. (2021) and Britzen et al. (2019).

Measuring the brightness temperature of the core and the hotspot shows a signifacant drop of 70% and 50% since the 2013 measurements, respectively, due to emission of jet material and the expansion of the jet.

Jet width measurements between 1200 and 19000 gravitational radii reveal a less cylindrical collimation profile, with $r \sim z_{obs}^{0.31}$ – where z_{obs} is the de-projected distance from the core and r is the width of the jet. The evolution of the restarted jet's profile from quasi-cylindrical (Giovannini et al. 2018) to less cylindrical implies that the cocoon surrounding the jet (Savolainen, 2018) cannot confine the jet material as it moves further from the core. The measured collimation profile corresponds to a slowly decreasing density, and more steeply decreasing pressure gradient in the external medium. Since the closest jet width measurement is only at 1200 gravitational radii from the core (here the jet width is 750 gravitational radii), it cannot confirm the wide jet base measured by Giovannini et al. (2018) at 350 gravitational radii. Based on this result, we arrive at the same conclusion as Giovannini et al. (2018), that the jet is either launched from the accretion disk, or it is ergosphere-launched, but undergoes a quick lateral expansion below 10^3 gravitational radii.

Avainsanat – Nyckelord – Keywords

radio astronomy - active galactic nuclei jets - RadioAstron - 3C 84

Säilytyspaikka – Förvaringställe – Where deposited

Muita tietoja – Övriga uppgifter – Additional information

Acknowledgements

Foremost, I would like to express my gratitude to my advisor, Docent Tuomas Savolainen for his guidance, feedback and patience throughout the research and writing of my thesis. Besides my supervisor, I would like to thank for Prof. Peter Johansson and my BSc thesis supervisor, Sándor Frey for their insightful comments.

Kedves Anya, Apa, Réka! A ti támogatásotok lehetővé tette hogy kövessem az álmaimat. Köszönök mindent!

I am grateful for the access to the computing resources at the Aalto University Metsähovi Radio Observatory. The RadioAstron project is led by the Astro Space Center of the Lebedev Physical Institute of the Russian Academy of Sciences and the Lavochkin Scientific and Production Association under a contract with the Russian Federal Space Agency, in collaboration with partner organizations in Russia and other countries. This research is based on observations correlated at the Bonn Correlator, jointly operated by the Max Planck Institute for Radio Astronomy (MPIfR), and the Federal Agency for Cartography and Geodesy (BKG).

Contents

1 Introduction

1.1 In a galaxy far, far away...

Active galactic nuclei (AGN) are one of the most powerful sources of the luminous Universe. Radio-loud AGN exhibit prominent relativistic outflows, known as jets, that appear perpendicular to the plane of the accretion disk that surround the central supermassive black hole. The jet's synchrotron radiation can be observed in the radio domain, so they are ideal targets for very long baseline interferometric observations (VLBI). The launching, evolution and time–variability of these objects is not fully understood. We study 3C 84, because its proximity, brightness and the intermittent nature of its jet makes it a good target to investigate the open questions of AGN phenomena.

3C 84 has been observed with radio telescopes since the sixties (Kellerman & Pauliny-Toth, 1966), and was monitored by several institutes and collaborations: the University of Michigan Radio Astronomy Observatory[1] (UMRAO) from 1965 until 2012; the Boston University Blazar Group since 2010 (Jorstad & Marscher, 2016, Jorstad et al., 2017); by Monitoring Of Jets in Active galactic nuclei with VLBA Experiments (MOJAVE) since 1995 (Lister et al., 2018) and Metsähovi Radio Observatory AGN monitoring program from the 1980s (Nagai et al., 2012).

3C 84's variable nature was already discovered in the early works of Kellermann (1966). At that time, jet activity was connected to the ejection of "mini radio lobes". Later, the radio outbursts were connected to the optical flaring events by Nesterov, Lyuty, Valtaoja (1995). With the rise of high-energy astrophysics, the source was studied in the x-ray and γ regime as well: Abdo et al. (2009) reported the discovery of high-energy γ-ray emission from 3C 84, but found no correlation between the γ-ray emission and radio outbursts.

The jet has already been observed in the 1980s. The remnants of this activity, the faint lobes are currently located ∼15-20 mas north and south from the core. A faint, parsec–scale jet pointing towards south–west was observed in the 1990s (Walker et al., 2000). Then the increased activity in 2003 started a powerful parsec-scale jet, ejected in a different direction than the jet that appeared in the 1990s. The restarted jet ends in a hotspot, denoted as C3 (Suzuki et al. 2012). The jet's evolution and structure has been studied with very long baseline interferometry by Nagai et al. (2010, 2014, 2017) and Suzuki et al. (2012). By adding the RadioAstron satellite to the ground-based antennas, Giovannini et al. (2018) presented the highest resolution results on the source. They resolved the limb-brightened structure of the jet and counter–jet in the close vicinity of the radio core. They measured jet width showed a wide base only a few hundred gravitational radii from the core, which either requires a quick lateral expanse in the jet width, or means that the jet is launched from the accretion disk rather than from the black hole ergosphere. It was also shown that the jet has an almost cylindrical collimation profile, very different from what was observed in M87.

[1] https://dept.astro.lsa.umich.edu/datasets/umrao.php

Figure 1: 3C 84, or NGC 1275 as seen by the VLA. The giant elliptical galaxy is located in the core of the Perseus cluster at z=0.0176. Image credit: NRAO.

1.2 On RadioAstron and space VLBI

RadioAstron was an international space VLBI project led by the Astro Space Center of Lebedev Physical Institute in Moscow, Russia. The payload, the Space Radio Telescope (Fig. 2), based on spacecraft Spektr-R, was designed by the Lavochkin Association. The spacecraft was launched on July 18, 2011, and was recently decommissioned after a 7-year mission on May 30, 2019.

The orbit of the satellite evolved between the apogee height of 270,000 and 370,000 km, and a perigee of 7,000 and 80,000 km with the period of 8 to 9 days. The initial inclination of the orbit was 51°. RadioAstron operated in the K (1.19–1.63 cm), C (6.2 cm), L (18 cm) and P bands (92 cm). The ground-based VLBI observations supplemented with RadioAstron could reach the fringe size of 7 μas at the highest frequency and longest baselines, which is the highest resolution that could be reached with VLBI (Kardashev et al., 2013).

Figure 2: Artist's impression of the RadioAstron Space Radio Telescope. Credit: Lavochkin Association.

1.3 Aim of the thesis

As the resolution of VLBI observations is getting finer, it became possible to observe the immediate surroundings of supermassive black holes residing in the center of not–too–distant galaxies. This high resolution enables us to study the accretion disk and jet physics, and compare the results to theory and numerical simulations, and provide better constraints on them.

The primary aim of this thesis is to confirm the results presented in Giovannini et al. (2018). The results –detection of limb–brightening in the jet and counter–jet, measured quasi–cylindrical collimation profile and the wide jet base – mentioned above may be artifacts of the poor (u,v) coverage due to the involvement of RadioAstron, the very same factor that enabled the authors to achieve ultra–high resolution during the observation. Since the space baselines of the observations discussed in this work are nearly perpendicular to that in the previous study, this enables us to test if the structures seen in 2013 were real.

The secondary aim of this work is to study the restarted jet's evolution – such as the change in the source structure, the orientation of the jet, the collimation profile – and investigate its interaction with the surrounding medium three years after the first space VLBI observations made by Giovannini et al. (2018). This is an excellent possibility, since such high spatial resolution (down to $\sim$100 gravitational radii) follow–up observation of a recently re–started jet has not been carried out before.

2 The structure and types of active galactic nuclei

2.1 Taxonomy of active galactic nuclei

The most widely accepted classification scheme for active galactic nuclei (AGN) was proposed by Urry & Padovani in 1995. The schematic structure and the main types of of AGN based on the viewing angle are shown in Fig. 3. The supermassive black hole at the center is surrounded by the accretion disk, which is the source of the(u,v)– resulting in the big blue bump in the spectral energy distribution – and X-ray emission. Broad-line and the narrow-line regions have telltale names, and are the origin of broad and narrow emission lines, respectively, depending on how deep they are located in the potential well of the black hole. The dusty torus, that surrounds the accretion disk, can also obscures the broad-line region when the system is seen from the side. Perpendicular to the plane of the accretion disk, a pair of collimated outflows of energetic particles, jets can appear, that are usually relativistically beamed due to the high velocity of the flow.

One way of classifying AGN arises from the objects' axisymmetric structure, that looks different under different viewing angles. Here I will follow the classification scheme of Urry & Padovani (1995) of radio-loud AGN, that exhibit prominent jets and lobes, observable in the radio domain. Radio loudness is defined so that the ratio of the 5 GHz flux density and B band optical flux density is greater than 10 (Kellerman et al. 1989).

Three main types of AGN can be separated based on their optical/UV spectra. Type I AGN have bright continuum emission with broad emission lines originating from hot gas moving with high velocities deep in the potential well of the central SMBH. This group contains the radio-quiet, low-luminosity Seyfert I galaxies and radio-quiet quasars that have higher luminosities. The radio-loud objects of this type are Broad-Line Radio Galaxies (BLRG) that have lower luminosity, and Steep Spectrum Radio Quasars (SSRQ) or Flat Spectrum Radio Quasars (FSRQ) with higher luminosities.

Type II AGN exhibit weaker continuum emission and have only narrow emission lines, indicating that dust obscures the inner regions of the AGN in our line of sight. Seyfert 2 type galaxies and narrow emission–line X-ray galaxies are the radio-quiet objects belonging to this class. According to the unified scheme, Seyfert 1 and 2 galaxies are the same objects seen from different angles. In accordance with this, Seyfert 2 galaxies also exhibit hidden broad–line regions, meaning that broad emission lines are present in their polarized spectra, just like in the case of Seyfert 1 objects (Du et al., 2017). Their radio-loud counterparts are Narrow-Line Radio Galaxies (NLRG), that have two morphological subclasses defined by Fanaroff & Riley (1974). Fanaroff–Riley type I (FR I) radio galaxies have symmetric jets with higher intensity close to the nucleus, while Fanaroff–Riley type II (FR II) galaxies have well collimated jets, with higher intensities in their lobes at the end of said jets. Radio–loud and radio–quiet sources are distinguished based on the presence of the radios, which misses from the latter.

Type 0 AGN all have some unusual spectral characteristics. Urry & Padovani (1995) puts blazars in this class. Blazars are sources that exhibit powerful jets that point towards our line of sight. BL Lacertae objects, a subclass of blazars have no emission lines, show rapid variability, unusually high and variable polarization and high brightness temperatures. FSRQ can also be classified as a subclass of blazars, that exhibit broad emission lines, but have blazar-like continuum emission.

In conclusion, the main difference between Type I and II AGN is the obscuration of the nuclear region, and radio galaxies differ from blazars in the alignment of the jet with our line of sight. In the next subsections I will concentrate on the properties of radio galaxies and blazars, as 3C 84 is a Fanaroff–Riley type I radio galaxy, and it is often classified as a misaligned blazar.

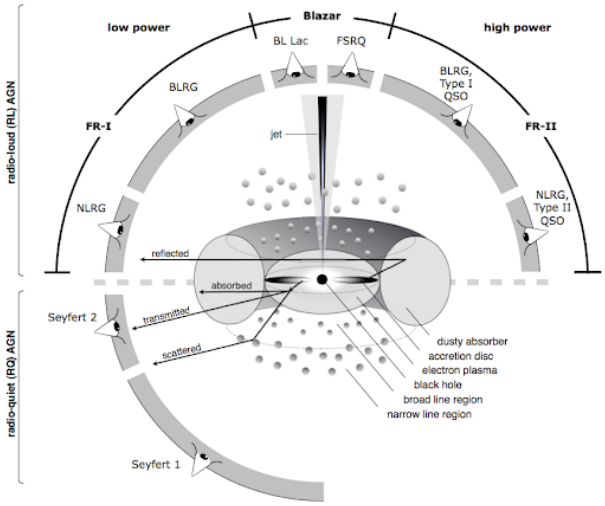

Figure 3: Schematic structure of AGN adopted from Beckmann & Shrader (2012). The supermassive black hole of 10^6 - 10^9 $M_\odot$ is surrounded by an accretion disk, obscured by a dusty torus. Perpendicular to the plane of the accretion disk, a pair of well-collimated outflows of energetic particles, jets can be formed. As a result of their axisymmetric structure, we observe different parts of AGNs under different viewing angles. The main classes based on the viewing angle are presented in the figure.

2.2 Radio galaxies

Radio galaxies are a type of AGN defined as 1.4 GHz radio power, $P_{1.4GHz} \geq 2x10^{23}$ W Hz^{-1}. Their host galaxies are mainly ellipticals. According to their optical spectra, we can distinguish broad-line (BLRG) and narrow-line (NLRG) radio galaxies, with broad and narrow emission lines in their spectra. Their radio-quiet counterparts are Seyfert 1 and 2 galaxies, respectively, but they differ in the type of their host galaxies.

According to the steepness of their radio spectra, $F_\nu \sim \nu^{-\alpha}$, where α is the spectral index, radio galaxies are divided into steep and flat spectrum sources, with the boundary of α=0.4 (Mo, van den Bosch & White, S., 2010). The flat spectrum sources tend to be compact and variable on observable timescales, whereas steep spectrum radio galaxies have extended structure.

Based on their morphology, radio galaxies can be divided into two classes (Fig. 4): Fanaroff–Riley type I galaxies generally have lower luminosities, and the jet's intensity peaks near the nucleus. Some appear as core-halo objects, often found at the center of galaxy cluster, like 3C 84. Jets usually have flat spectrum, with $\alpha \sim 0.6$, that steepens towards the jet ends. On the other hand, the higher-luminosity Fanaroff–Riley type II galaxies have lobes ending in hotspots, and more collimated jets. FR II galaxies are usually more powerful than FR I's, with $P_{1.4GHz} \geq 4x10^{25}$ W Hz^{-1}.

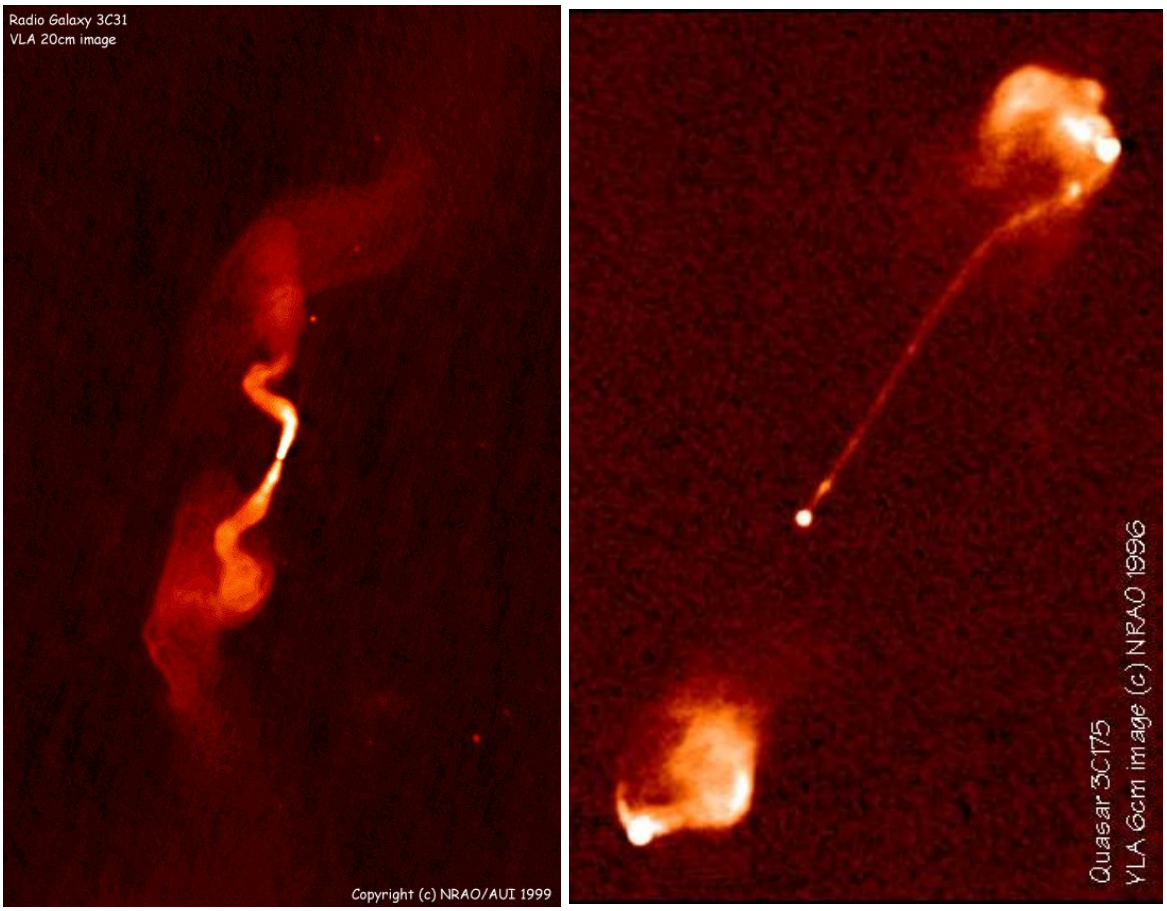

(a) 3C 31 (b) 3C 175

Figure 4: VLA images of Fanaroff-Riley type I and II AGN. In 3C 31 <50% of the flux density originates from the inner jet regions, the jet is already sub–relativistic on intermediate scales and dissipates as it moves outwards. For 3C 175, >50% of the flux density is from the lobes at the jet ends, the jet remains relativistic to large radii, and moves freely until it encounters the intergalactic matter. Images credit: NRAO.

2.3 Blazars

Blazars are a type of AGN where the relativistic jet axis has only a small angle with our line of sight. Their main characteristics are relativistic effects resulting from the jet directed towards us. The jet appears brighter due to the relativistically beamed emission, and it exhibits superluminal motion. The emission is also blue shifted, and the relativistic Doppler effect shortens the variability timescales. They show rapid variability in the optical to X-ray domain, strong polarization in the radio and optical, and high luminosity that can be explained with relativistic beaming effects (Blandford & Rees 1978). They are strong radio and γ-ray emitters, and sometimes the γ-ray luminosity can outshine the luminosity of other bands by a factor between 1 to 1000.

BL Lac objects, a subclass of blazars, usually have spectra that lacks emission lines, since the lines are weak, and are suppressed by the Doppler boosted continuum emission of the jet. FSRQ, and other type of blazars, however exhibits strong emission lines. The host galaxies of BL Lacs, similarly to FR I radio galaxies, are ellipticals, with the same average half-light radius and absolute magnitude of the FR

I hosts. An other similarity between these two galaxy types is the magnitude of their radio power, that is around $\sim 10^{25}$ W Hz^{-1}. FSRQs have host galaxies similar to FR II radio galaxies.

The continuum emission of blazars can be described with two components (Fig. 5). The low-energy component, ranging from the radio to the UV, is due to synchrotron emission, and it is strongly polarized from radio to optical. The high-energy component between the(u,v)and γ-ray regime is caused by inverse Compton scattering. The photons may originate from synchrotron emission, that are Compton scattered by the same electrons that radiated them. This process is know as synchrotron self-Compton scattering. Photons can also originate from other parts of the AGN, from the accretion disk, broad–line region or the the torus. This is known as external Compton scattering. Depending on the ratio of the X-ray to radio flux, Padovani & Giommi (1995) defines high-frequency peaked (HBL or XBL) and low-frequency peaked (LBL or RBL) BL Lacs, whether α_{rx}, the spectral index between 5 GHz and 1 keV smaller or bigger than 0.75 (Ulrich, Maraschi & Urry, 1997).

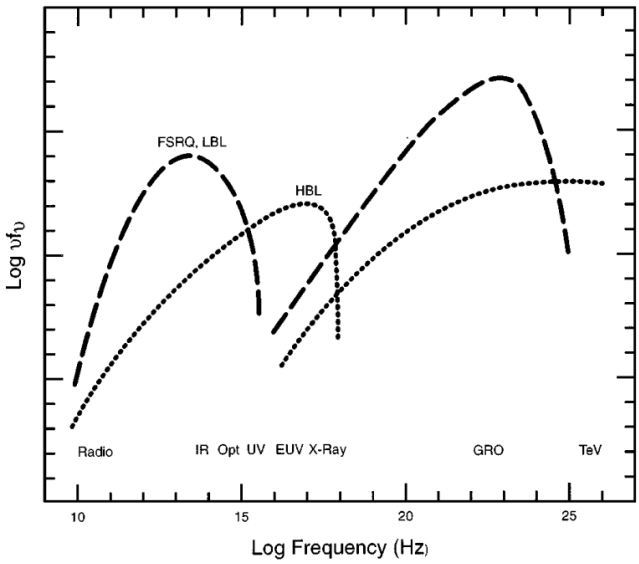

Figure 5: Schematic broadband spectra of high- (dotted line) and low-energy (dashed line) peaked blazars. The low-energy component is due to synchrotron emission, while the high-energy component is caused by the inverse process. Image credit: Ulrich, Maraschi & Urry (1997).

3 Current understanding of jet launching

3.1 Launching of black hole jets

We can observe jets not only in active galactic nuclei with supermassive black holes of several million to billion Solar masses, but in stellar-mass systems of a few Solar masses, like gamma-ray bursts and black hole binaries. If we want to describe jet launching in objects over several magnitudes of central masses and energy outputs, we need to find a process that is scale-invariant. Magnetic fields provide a straightforward explanation, as the properties of magnetically-powered outflows scale with black hole mass, and are abundant in astrophysical plasmas, are also present in the jet, the central object and the surrounding medium as well. Accreting black holes can power their outflows either through dissipation in the disk (Blandford–Payne mechanism, Blandford & Payne, 1982), supported by numerical simulations of thin accretion disks (Casse & Keppens, 2002), or in the case of a rapidly rotating black hole by the extraction of angular momentum from the black hole itself (Blandford–Znajek mechanism, Blandford & Znajek, 1977), also confirmed by numerical simulations (McKinney & Gammie, 2004 and Tchekhovskoy et al., 2011).

3.1.1 The Blandford–Znajek mechanism[2]

Based on the no hair theorem, isolated black holes can be described solely by three parameters: their mass, $M_{\rm BH}$, their spin, $S_{\rm BH}$, and their charge, $\rm Q_{BH}$. The latter can be ignored, since black holes cannot contain gravitationally significant amount of charge. Then the spacetime around the hole is given by the Kerr-metric, which in the Boyer–Lindquist coordinates reads as:

$$ds^2 = -\Big(1 - \frac{2mr}{\Sigma}\Big)dt^2 - \frac{4amr\sin^2\theta}{\sigma}dtdt\phi + \frac{\sigma}{\Delta}dr^2 + \Sigma d\theta^2 + \Big(r^2 + a^2 + \frac{2mra^2\sin^2\theta}{\Sigma}\Big)\sin^2\theta d\phi^2, \quad (1)$$

where

$$\Sigma = r^2 + a^2\cos^2\theta \quad (2)$$

$$\Delta = r^2 - 2mr + a^2. \quad (3)$$

Here m is the mass of the central object and a is its specific angular momentum.

Let's consider general orbits of particles, where (r, θ) are constant. These are not only orbits of particles in free-fall, so non-gravitational forces are needed to keep a particle on one of these orbits. The angular velocity is defined as the rate of change in the azimuthal coordinate, ϕ, with respect to the coordinate time, t:

$$\Omega = \frac{u^\phi}{u^0}, \quad (4)$$

[2]This chapter is based on: Blandford, Netzer, Woltjer & Courvoisier (1990)

where u^α is the proper velocity of the particle. The quadratic formula for Ω, using $u^{\alpha_\alpha} = -1$:

$$\Omega^2 g_{\phi\phi} + 2\Omega^2 g_{0\phi} + g_{00} + (u^0)^{-2} = 0. \tag{5}$$

The angular velocity falls between the limits:

$$\Omega_{\rm min} = \frac{-g_{0\phi} - (g_{0\phi}^2 - g_{00}g_{\phi\phi})^{1/2}}{g_{\phi\phi}} < \Omega < \frac{-g_{0\phi} + (g_{0\phi}^2 - g_{00}g_{\phi\phi})^{1/2}}{g_{\phi\phi}} = \Omega_{\rm max}. \tag{6}$$

Around a Kerr black hole, where $a > 0$ and $g_{0\phi} < 0$, $\Omega_{\rm min}$ is positive when g_{00} is positive, which condition is fulfilled when r is smaller than the static limit, $r_E = m + (m^2 - a^2\cos^2\theta)^{1/2}$. The static limit exists because of frame dragging, also known as the Lense–Thirring effect. A ring of matter orbiting around a slowly spinning black hole will precess with the frequency:

$$\Omega_{\rm P} = \frac{2S}{r^3}, \tag{7}$$

where $S = am$, the spin of the hole. The Lense–Thirring effect is important when studying the behaviour of the accretion disk.

The other well-known surface connected to black holes is the event horizon, where photons are trapped so their radius r can no longer increase. The event horizon can be found where $\Delta \to 0$:

$$r_+ = m + (m^2 - a^2)^{1/2}. \tag{8}$$

Here at r_+, the limits on Ω reach a common value that does not depend on the latitude:

$$\Omega_{\rm H} = \frac{a}{2mr_+} = \frac{a}{r_+^2 + a^2}. \tag{9}$$

$\Omega_{\rm H}$ is the angular velocity of the black hole. The region between r_+ and r_E, i. e. the event horizon and the static limit is called the ergosphere. Particles moving in this region, with orbits only crossing the event horizon, but not the static limit, can have a negative total energy. If such a particle crosses the event horizon, it will cause the mass of the black hole to decrease. This is known as the Penrose process, that shows it is possible to extract spin energy from a rotating black hole.

The irreducible mass, or the mass of the hole that cannot decrease as mass is added to the hole, is given by:

$$m_{\rm i} = \left(\frac{A}{16\pi}\right)^{1/2}, \tag{10}$$

A is the area of the event horizon:

$$A = \int d\theta d\phi (g_{\theta\theta} g_{\phi\phi})^{1/2} = 8\pi m r_+. \tag{11}$$

From Eq. 10, the total mass of the hole can be written as:

$$m = \frac{m_{\rm i}}{(1 - 4m_{\rm i}^2\Omega_{\rm H}^2)^{1/2}}; \quad \Omega_{\rm H} < \frac{1}{\sqrt{8}m_{\rm i}}. \tag{12}$$

The upper limit on $\Omega_{\rm H}$ is needed to ensure that $a < m$. From the equation above, a bound on the reducible mass can be calculated:

$$m - m_{\rm i} < 0.29m, \tag{13}$$

meaning that up to 29% of the rest mass energy of a Kerr black hole can be extracted.

One way to do this is via the electromagnetic field. Based on the no hair theorem, isolated black holes cannot have electromagnetic field on them. But if a hole is placed in a uniform electric field, the event horizon becomes an equipotential surface, and behaves like an electrical conductor. However, the event horizon is not a perfect conductor, so when the surrounding magnetised plasma falls over the event horizon, remnants of a rapidly varying and decaying electromagnetic field will still be present at the event horizon. From Maxwell's equation:

$$\frac{\partial \mathbf{B}}{\partial t} = -\nabla \times \mathbf{E} \sim -\frac{E}{m} \sim -\frac{JR_{\rm H}}{m} \sim -\frac{BR_{\rm H}}{4\pi m}, \tag{14}$$

where $R_{\rm H}$ is the surface electrical resistance of the horizon. Equating this with $-B/t_{\rm decay}$, where $t_{\rm decay}$ is the decay timescale of the electromagnetic field at the event horizon, the first and last terms determine $R_{\rm H}$ as:

$$R_{\rm H} \approx= 4\pi = 377\Omega. \tag{15}$$

So the surface electrical resistance of the event horizon is 377 Ohm.

When a spinning black hole is embedded in a magnetic field, since it is a conductor, unipolar induction will a cause a potential difference to develop between the equator and the poles. The potential difference is:

$$V \sim \Omega_{\rm H} m^2 B \sim \Omega_{\rm H} \Phi \tag{16}$$

where Φ is the magnetic flux threading the hole. If there is a current flowing externally between the equator and the poles, it can either dissipate or do work on the plasma surrounding the hole. In both ways, the electromagnetic field extracts energy from the spin of the central object.

Let's consider two adjacent field surfaces in an axisymmetric field distribution. Then the poloidal component of the current flow can be decomposed into superposed circuits with current I flowing through them. The flux difference between the surfaces is $\Delta\Phi$. The potential difference between the the two surfaces at the event horizon:

$$\Delta V_{\rm H} = \frac{(\Omega_{\rm H} - \Omega)\Delta\Phi}{2\pi} = I\Delta R_{\rm H}, \tag{17}$$

and the across the load:

$$\Delta V_{\rm L} = \frac{(\Omega - \Omega_{\rm L})\Delta\Phi}{2\pi} = I\Delta R_{\rm L}, \tag{18}$$

where Ω is the angular velocity the field lines. Ω is constant along a field line. By eliminating the current I, we can combine these equations, and obtain the intermediate angular frequency between the that of the load and the black hole:

$$\Omega = \frac{\Omega_{\rm H}\Delta R_{\rm L} + \Omega_{\rm L}\Delta R_{\rm H}}{\Delta R_{\rm L} + \Delta R_{\rm H}}. \tag{19}$$

As a result of the electromagnetic force exerted on the black hole, a torque, ΔG will decrease its angular momentum at a rate:

$$\Delta G = \frac{I\Delta\Phi}{2\pi} = \frac{I^2(\Delta R_{\rm H} - \Delta R_{\rm L})}{\Omega_{\rm H} - \Omega_{\rm L}}, \tag{20}$$

and it will be supplied to the load via the magnetic field. By rearranging this, we get the energy equation:

$$-\Delta G\Omega_{\rm H} + \Delta G\Omega_{\rm L} + I^2\Delta R_{\rm H} - I^2\Delta R_{\rm L} = 0. \tag{21}$$

The first two terms give the work done by the torque on the hole and the load, and the latter half of the equation gives the power dissipated through the hole and the load. Since there is no external energy source, the sum of these powers must vanish.

These equations are correct under the force-free approximation, and show that a significant amount of energy can be extracted from the black hole spin via a magnetic field generated by external currents. The black hole will lose energy, and this energy will be dissipated in the load. There is also dissipation in the black hole itself, and although its gravitational mass will decrease, the irreducible mass will increase.

Accretion onto the black hole is usually accompanied by powerful outflows, that may or may not be collimated. If they are not collimated, we call them winds. They are common signs of the ongoing accretion in young stellar objects. Collimated outflow are called jets, and are mostly associated with active galactic nuclei. These outflows are capable of reaching ultrarelativictic speeds and Lorentz factors of $\gamma \sim 10$, and are generated deep in the potential well of the central black hole. Many of the jets are well-collimated by the time they reach the distance of ~ 1 pc from the core, which requires strong forces to collimate the particle flow. In contrast to other models, the Blandford–Znajek mechanism can account for all the features in a natural manner. The first general relativistic magnetohydrodynamic (GRMHD) simulations to capture the mechanism were carried out by McKinney & Gammie (2004). In agreement with VLBI observations, they identified the main regions surrounding an accreting black hole: the accretion disk, plunging region, corona and the funnel and wind regions. GRMHD simulations performed by Tchekhovskoy et al. (2011) proved that black holes are capable of accumulate a large–scale magnetic flux, and producing powerful outflows, as observed by Ghisellini et al. (2010), via extracting energy from the rotating black hole.

3.1.2 The Blandford–Payne mechanism[3]

Outflows can also be launched from from the accretion disk around the black hole. The disk and its surroundings can be divided into force-free and not force-free parts based on the relative importance of the magnetic field energy density (Fig. 6). Since the magnetic field is anchored to the accretion disk, the energy density is smaller than the rotational energy, making this region not force-free. Let's assume that the vertical field strength at the disk surface is sufficiently large. Above and below the disk the magnetic energy density is larger than the thermal and rotational energies, making this region force-free.

[3]This chapter is based on: Spruit (1996).

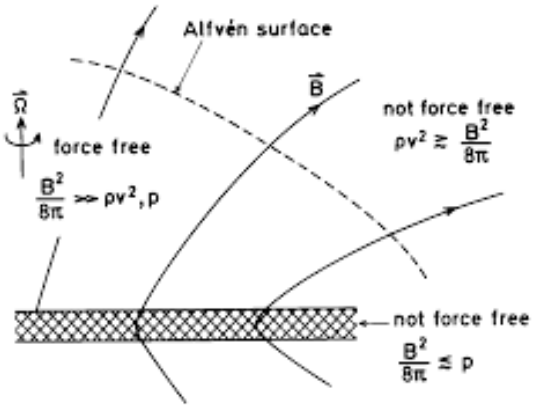

Figure 6: Force-free and non-force free magnetic field regions of the disk wind. Image from Spruit (1996)

As the field is anchored in the accretion disk, due to differential rotation, the loops generated will be sheared, and some of them will remain open. The field strength will drop in the accelerated flow, and acceleration stops at the Alfvén-surface, when the flow speed reaches its local Alfvén speed. After the Alfvén-surface the force-free approximation is no longer valid.

In the case of a cool disk with Keplerian rotation and negligible thickness surrounded by ionized gas, we can expect ideal MHD conditions to hold. Near the disk surface the disk atmosphere corotates with the field lines due to the large field strength. The acceleration of the plasma attached to the field lines is analogous to the bead-on-a-wire scenario. As a result of the Keplerian disk rotation, the gravitational force is balanced at the base of the field line by the centrifugal force. The centrifugal force along the field line increases as we are moving away from the axis, and when it exceeds the gravitational force, the plasma along the line will be accelerated outwards. When the field is no longer able to enforce corotation at the Alfvén surface, the acceleration stops. Beyond this point, the field lines get wound up due to the gas lagging behind the field line rotation, as it can be seen in Fig. 7. With each rotation of the base point we acquire a new loop of the field line in a spiral formation with pitch v/Ω.

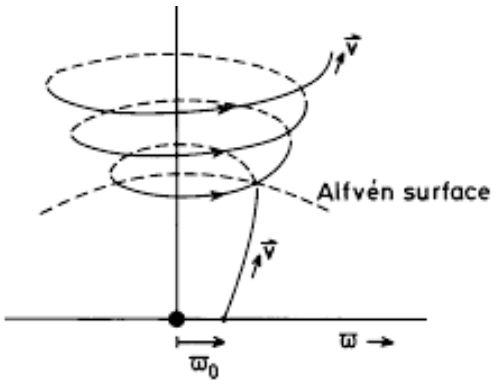

Figure 7: Evolution of a field line over the Alfvén surface. The field line gets wound up due to the gas lagging behind the field line rotation, so with each rotation of the base point we acquire a new loop. Image from Spruit (1996).

This model is attractive because apart from explaining the origin of the outflow, it also extracts angular momentum from the disk, allowing the gas to accrete with efficiency:

$$\frac{\dot{M}_w}{\dot{M}_a} = \frac{1}{2}\Big(\frac{r_0}{r_A}\Big)^2, \tag{22}$$

where $\dot{M}_w$ is the mass flux of a field line with foot point r_0, $\dot{M}_a$ is the accretion rate and r_A is the radius of the Alfvén surface. Since r_A is always larger than r_0, only a fraction of the mass flux in the disk can be carried away by the outflow.

The formation of the wind can be divided into three stages. The wind is launched near the disk surface, where the structure of the disk and magnetic field configuration will determine how much mass is launched into the flow. After being launched, until the Alfvén surface, the acceleration of the flow is controlled by gravitational and centrifugal forces. After acceleration, the flow is collimated by hoop stress of the toroidal magnetic field, that directs the poloidal field lines towards the outflow axis. This effect is important when the strength of the poloidal field approximately equals or exceeds that of the poloidal field. When the poloidal field dominates, its internal equilibrium is responsible for shaping the magnetic field configuration. MHD and relativistic MHD simulations of Ferreira (1997) and Porth & Fendt (2010) confirm that jets accelerated by the Blandford–Payne mechanism are collimated by hoop stress of the toroidal magnetic field component, and this happens before they could reach relativistic speeds.

3.2 Numerical simulations of AGN jets[4]

The opportunity to test theoretical results on the structure, formation and environment of jets emerged when the first supercomputers appeared, enabling researchers to numerically solve the equations governing the evolution of the system. The more powerful and widely available supercomputers together with user-friendly, publicly available codes resulted in the quick rise of computational astrophysics, and today simulations are an essential part of investigating jets. Below I summarize the main results of the field that are connected to the launching, evolution and feedback of AGN jets.

Astrophysical jets can be described by the one-dimensional fluid model (Begelman et al., 1984), where the quasi–parallel flow of plasma is embedded in the background medium. The magnetic field plays an important role in making the flow fluidlike, so when large-scale magnetic stresses become dynamically important, one has to turn to magnetohydrodynamics (MHD). When general relativistic effects are included, we talk about general relativistic MHD (GRMHD).

The first jet simulation was performed in 1977, by Rayburn. It investigated the interaction between a fluid jet and the uniform ambient medium, and found that a jet forms a forward bow shock and inflates a cocoon in the external medium. The reverse shock indicates the end of the supersonic jet flow, described by the twin–exhaust model of Blandford & Rees (1974). These results were supplemented by the work of Norman (1982), who found a chain of quasi-stationary shocks forming in the jet body as a result of the interaction with the cocoon.

The first studies that accounted for jet collimation by the external medium found that the pressure exerted on the fluid jet by the surrounding medium forms conical shocks in the jet body (Sanders, 1983).

[4]This chapter is based on: Komissarov & Porth (2021)

Knots (collimation shocks) in the jet of M87 are also formed this way (Falle & Wilson, 1985). Collimation can be induced by the pressure of the jet–inflated cocoon (Falle, 1991). The jet of 3C 84 is confined by such interaction, hence the observed quasi–cylindrical profile (Giovannini et al., 2018).

The first attempts at numerical simulations on jet launching appeared in the 1990s. The first robust detection of the Blandford–Znajek mechanism was published in 2004 by McKinney & Gammie. The numerical simulations follow the evolution of a Kerr black hole surrounded by a weakly magnetized plasma torus (Fishbone & Moncrief, 1976) under ideal MHD conditions. The model can be divided into five regions (Fig. 8), based on the ratio of average pressure to average magnetic pressure. The highest density region marks the Keplerian disk. The funnel, a highly magnetized, evacuated region is located near the pole, and the wind region forms a cone of material near the funnel's edge. Collimated poloidal field lines in the funnel enable matter to escape through this region to form jets. The edge–brightened jet of 3C 84 (Giovannini et al, 2018) shows a similar funnel structure, since the low–density spine region shows little to no emission. The corona falls between the funnel and the accretion disk, whereas the plunging region is between the disk and the event horizon.

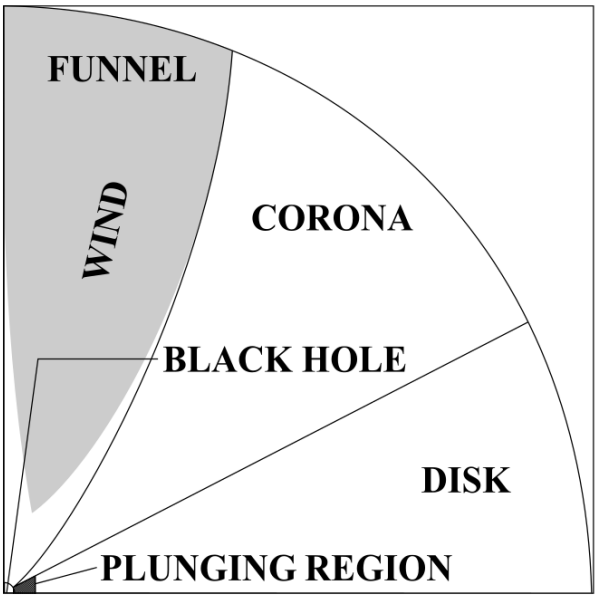

Figure 8: Based on ratio of average pressure to average magnetic pressure, McKinney & Gammie (2004) differentiate five regions around an accreting black hole. The Keplerian disk is matter-dominated, whereas the funnel around the pole is magnetically dominated. Here the the magnetic field is collimated and and forms outflow or jet. The corona is located in the in the low density upper layers of the disk. Finally, the plunging region is located between the disk edge and the black hole event horizon, and the wind region is at the corona-funnel boundary.

After demonstrating the black holes are capable of powering jets, the simulations turned towards investigating how powerful these jets can be. GRMHD simulations performed by Tchekhovskoy et al. (2011) show that black holes can accumulate large-scale magnetic flux via accretion from the disk, and the accumulated flux is capable of obstructing the gas infall, leading to magnetically-arrested disks (MADs). Recently a MAD have been found at the center of the M87 galaxy. 230 GHz polarimetric observations of the Event Horizon Telescope investigating the immediate surroundings of the M87 black hole find that

estimates of average density, magnetic field strength and temperature of the disk material are consistent with simulation results of MADs (The Event Horizon Telescope Collaboration, 2021).

The simulation with the MAD initial condition produce jets reaching ∼300% efficiency. Jet efficiency is defined as the ratio of the black hole spindown power and the accretion power. The high efficiency of MADs not only proves the Blandford–Znajek mechanism, i.e., that energy extraction is possible from a rotating black hole, but it is also consistent with observations of Fernandes et al. (2011) on jet efficiency in radio galaxies.

As described in the previous section, jets can also be launched from the accretion disk surrounding the central compact object, known as the Blandford–Payne mechanism (Blandford & Payne, 1982). The first simulations to capture such outflows were carried out by Casse & Keppens (2002, 2004). In their MHD simulations of a thin accretion disk launches jets that reach trans–Alfvénic and magnetosonic speeds. These outflows were accelerated by the magneto–centrifugal effect, while the toroidal component of the magnetic field was responsible for the collimation via hoop stress.

Simulations on collimation and acceleration of these outflows (Porth & Fendt, 2010) indicate that collimation via hoop stress happens before the outflow reach relativistic speeds. They also report a spine–sheath structure – a subrelativistic flow originating from the disk enveloping a reletivistic jet – observed in several AGN.

Although GRMHD codes are now available for both jet–launching models, the interaction between ergosphere– and disk–launched jets is rarely modeled, since it is very difficult to constrain the properties of the accretion disk. The modeling of these interactions would be fascinating, since it could provide explanation for example for the limb–brightened structure of jets, like in the case of 3C 84 (Nagai et al., 2014 and Giovannini et al., 2018).

How do observations complement results of numerical simulations? Ultra-high resolution VLBI observations, either achieved by extremely long baselines – space VLBI –, or by mm–VLBI – Event Horizon Telescope –, enable us to image jets in the vicinity of their formation sites. This easy we can test simulation results observationally. Polarization measurements provide us with an insight to the magnetic field structure (see the implied radial magnetic field in the external medium of 3C 84 in Nagai et al., 2017 and the MAD in M87 observed by the Even Horizon Collaboration, 2021). The jet width profile enables us to test which launching mechanism formed the jet. A wide jet base suggest that the jet is formed via the Blandford–Payne mechanism (Blandford & Payne, 1982), and is launched from the accretion disk. Ergosphere–launched jets, however, have a narrower base compared to their disk–launched counterparts. Giovannini et al. (2018) presented jet width measurements from only a few hundred gravitational radii, $r_{\rm g}$ from the core. In this work, I attempt to repeat their measurements on the new RadioAstron data, and confirm their results. Measuring the collimation profile and acceleration of the jet flow can also test the values predicted by simulations. The emission structure, like the limb–brightening observed in 3C 84 (Nagai et al., 2004 and Giovannini et al., 2018) and nearby radio galaxies in ultra–high resolution could also be an interesting aspect of comparison between simulations and observations, but this is not yet possible because particle acceleration is not fully understood (Hardcastle, 2015).

4 Very long baseline interferometry

The Earth's atmosphere is transparent in three wavelength ranges, so electromagnetic radiation outside from our planet's atmosphere can reach us, observers. The optical transmission window falls between 300 and 1100 nm, the infrared one between 8 and 14 μm, and finally the radio window is between 1 cm and 11 m, complemented by small, relatively transparent windows in the mm–regime. These atmospheric transmission windows enabled these fields of astronomy to evolve faster than the ones requiring satellites for observations. Still, radio astronomy only appeared in the 1930's, when Karl Jansky, the engineer of Bell Telephone Laboratories discovered galactic synchroton radiation originating from the galactic center. Jansky's pioneering work was followed by Grote Reber, who built the first parabolic antenna used for astronomical observations. Radio astronomy truly started after World War II., and had several notable discoveries in the past 80 years, involving the discovery of the cosmic microwave background in 1964 by Penzias and Wilson, the discovery of pulsars by Jocelyn Bell in 1967, or the first image of a black hole in the center of M87.

Nowadays, the term radio astronomy is used to refer to mostly telescopes using heterodyne technology. In a heterodyne receiver, observed sky frequencies are converted to lower frequency signals by mixing them with a known signal, artificially created by a local oscillator (LO). The output can then be amplified and analyzed more easily, while retaining the original phase and amplitude information of our observation.

4.1 The quest for resolution[5]

In imaging, the angular resolution is directly proportional to the observing wavelength, and inversely proportional to the diameter of the telescope:

$$\theta \propto \frac{\lambda}{D}. \tag{23}$$

In the case of radio astronomy, we are observing in the long wavelength end of the electromagnetic spectrum, where $\lambda \geq 1$ mm. To compensate for the large wavelength, we need to increase the diameter of our instruments. However, we are only capable of building fully steerable radio telescopes up to $\sim$100 m in diameter (Effelsberg, Green Bank), or fixed, filled-aperture antennas with steerable receivers (the ill-fated Arecibo Telescope, and the Five-hundred-meter Aperture Spherical radio Telescope/FAST). Still, radio telescopes with these impressive sizes only reach the same resolution as our eyes do in the optical domain, or more precisely, our 2 mm pupils have 1' angular resolution at $\lambda = 5000$ Å. The same resolution would be achieved by a 140 m diameter telescope observing at $\lambda = 4$ cm. However, it is possible to coherently combine the output of two reflectors, so the resolving power will be $\theta \approx \lambda$/D, where the diameter d of the reflectors is significantly smaller than their separation D, $d \ll D$.

Aperture synthesis is a technique that aims to reproduce the imaging properties of a large antenna by combining the signal of multiple, smaller antennas.

The power response of a uniformly illuminated, circular, parabolic antenna can be described with the full width at half maximum (FWHM) or full width to half power (FWHP) of the main beam, which is approximately FWHP$\approx \lambda/D$. The first null is also located around $\sim \lambda/D$. Since our telescopes are

[5]This chapter is based on: Wilson, Rohlfs & Hüttemeister (2013) and Perley, Schwab & Bridle (1989).

not ideal, there is always response outside the main beam, and these secondary maxima are called side lobes. In the case of an interferometer,the response is obtained from the multiplication and averaging of the outputs of the two antennas. Here the main beam and side lobes are collectively called fringes, because in an ideal case, there is no decrease in power with increasing angular offset from the axes of the antennas. In order to improve the dynamic range of the observations by suppressing the total power output of each antenna, the fringes are centered around zero angular offset, although this way we lose some of the information, like the total power. By increasing the separation, i.e., baseline between the antennas, the FWHP of the fringes decrease, so finer and finer source structure can be detected.

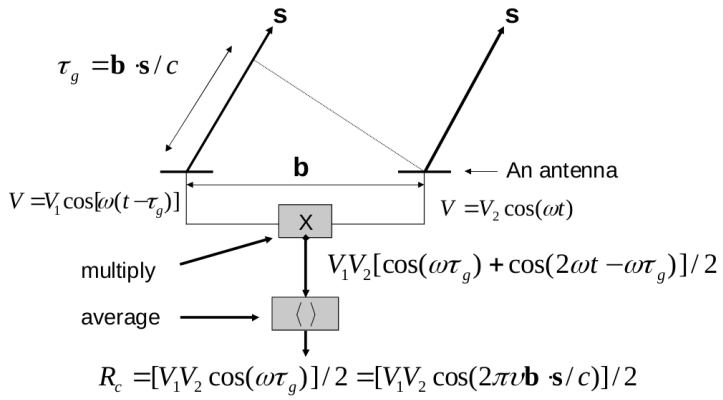

Figure 9: Schematic structure of a two-element interferometer. Image credit: Perley, Schwab & Bridle (1989).

Let's consider an ideal, stationary two-element interferometer whose schematic structure is seen in Fig. 9. The radiation is assumed to be quasi-monochromatic, with finite, small bandwidth dν, and single polarization. Then, the amplitude and phase of the field can be considered constants for periods of dt $<$ dν^{-1}:

$$E_\nu(t) = A\cos(2\pi\nu t + \phi). \tag{24}$$

The electric fields are assumed to originate from a small solid angle $d\Omega$, around a direction $\mathbf{s}$, within a finite bandwidth $d\nu$ at frequency ν. The two identical instruments in our measurement are separated by a baseline vector $\mathbf{b}$. Due to the separation between the antennas, the wave front reaches the more distant telescope with a delay, called the geometric time delay:

$$\tau_{\rm g} = \frac{\mathbf{b}\cdot\mathbf{s}}{c}. \tag{25}$$

The instrumental delay $\tau_{\rm i}$, on the other hand, arises from the signal propagating through the antenna electronics. Here we ignore this effect. The phase corresponding to the extra distance the wave travels is defined as:

$$\Theta = \omega\tau_{\rm g} = \frac{2\pi\mathbf{b}\cdot\mathbf{s}}{\lambda}, \tag{26}$$

where ω is the angular frequency of the signal. The voltage output of the first antenna is:

$$V_1 = A_1\cos(\omega t), \tag{27}$$

and the second, more distant antenna:

$$V_2 = A_2 \cos\left(\omega(t - \tau_{\rm g})\right). \tag{28}$$

These outputs are correlated, first going through a voltage multiplier followed by an integrator, that averages the signal. After multiplication, we get:

$$R_{\rm c}(\tau) = \frac{A_1 A_2}{2}[\cos\left(\omega\tau_{\rm g}\right) + \cos\left(2\omega t - \omega\tau_{\rm g}\right)]. \tag{29}$$

The averaged product will depend on the received power, $P = A_1 A_2/2$ and the geometric delay $\tau_{\rm g}$ that includes the baseline orientation and source direction as well:

$$R_{\rm c}(\tau) = P\cos\left(\omega\tau_{\rm g}\right) = P\cos\left(\frac{2\pi\mathbf{b}\cdot\mathbf{s}}{\lambda}\right) = Pe^{i\omega\tau_{\rm g}} \tag{30}$$

The mutual correlation function, $R_{\rm c}$ will vary due to the change of source orientation, $\mathbf{s}$ because of the rotation of the Earth. On the other hand, $R_{\rm c}$ is not a function of the observing time (unless the source varies rapidly), the location of the baseline, or the actual phase of the incoming signal if the emission is far-field. The strength of the product depends on the antenna collecting areas and the electronic gains.

By introducing a 90°phase shift before the signal reaches the correlator, we get a sinusoidal signal after multiplication:

$$R_{\rm s}(\tau) = \frac{A_1 A_2}{2}[\sin\left(\omega\tau_{\rm g}\right) + \sin\left(2\omega t - \omega\tau_{\rm g}\right)], \tag{31}$$

and after averaging:

$$R_{\rm s}(\tau) = P\sin\left(\omega\tau_{\rm g}\right) = P\sin\left(\frac{2\pi\mathbf{b}\cdot\mathbf{s}}{\lambda}\right) \tag{32}$$

The response from an extended source is obtained by summing the responses at each antenna to all the emission over the sky, multiplying the two, then averaging:

$$R_{\rm c} = \Big\langle \int\int V_1 d\Omega \times \int\int V_2 d\Omega \Big\rangle. \tag{33}$$

Providing that the emission is spatially incoherent, changing the order of averaging and the integrals, we have:

$$R_{\rm c} = \int\int I_\nu(\mathbf{s})\cos\left(2\pi\nu\mathbf{b}\cdot\mathbf{s}/c\right)d\Omega \tag{34}$$

The correlator projects a cosinusoidal coherence pattern with angular scale $\sim \lambda/b$ rad on the source, and after multiplying its brightness with this pattern, it sums the the result over the source extent. The orientation of the pattern is set by the geometry of the baseline, and the fringe separation is determined by the observing frequency and baseline length.

Since any real function, $I(s)$, can be expressed as the sum of two real functions with specific symmetries, the sky brightness can be written as a sum of an even ($I_{\rm e}(s) = I_{\rm e}(-s)$) and odd ($I_{\rm o}(s) = -I_{\rm o}(-s)$) function: $I(s) = I_{\rm e}(s) + I_{\rm o}(s)$.

So when we are using the cosine correlator, we only see the even part of the brightness distribution:

$$R_{\rm c} = \int\int (I_{\rm o}(\mathbf{s}) + I_{\rm e}(\mathbf{s})) \cos{(2\pi\nu \mathbf{b}\cdot\mathbf{s}/c)} d\Omega = \int\int I_{\rm e}(\mathbf{s}) \cos{(2\pi\nu \mathbf{b}\cdot\mathbf{s}/c)} d\Omega, \tag{35}$$

and we are unable to fully recover the source brightness. This is the reason, why we introduced the sine correlator:

$$R_{\rm s} = \int\int (I_{\rm o}(\mathbf{s}) + I_{\rm e}(\mathbf{s})) \cos{(2\pi\nu \mathbf{b}\cdot\mathbf{s}/c)} d\Omega = \int\int I_{\rm o}(\mathbf{s}) \cos{(2\pi\nu \mathbf{b}\cdot\mathbf{s}/c)} d\Omega. \tag{36}$$

It is possible to define the complex visibility function from the two independent correlator outputs as the following:

$$V = R_{\rm c} - {\rm i}R_{\rm s} = Ie^{-{\rm i}\phi}, \tag{37}$$

with sky brightness

$$I = \sqrt{R_{\rm c}^2 + R_{\rm s}^2} \tag{38}$$

and

$$\phi = \tan^{-1}\left(\frac{R_{\rm s}}{R_{\rm c}}\right). \tag{39}$$

This leads to the relationship between the sky brightness I, and the response V of an interferometer:

$$V_\nu(\mathbf{b}) = R_{\rm c} - {\rm i}R_{\rm s} = \int\int I_\nu(\mathbf{s}) e^{-2\pi {\rm i}\nu \mathbf{b}\cdot\mathbf{s}/c} d\Omega, \tag{40}$$

where the visibility is the 2D Fourier transform of the brightness distribution.

In the above derivation we did not take instrumental delay into account, that arises due to signal propagation through the electronics, and can be adjusted, so it equals the geometric delay. The instrumental delay is given by:

$$\tau_i = \frac{\mathbf{b}\cdot\mathbf{s}_0}{c}, \tag{41}$$

where $\mathbf{s}_{\rm o}$ is a reference direction. The signal from the first antenna after introducing a time delay as defined above:

$$V_1 = A_1 \cos{(\omega(t-\tau_i))}, \tag{42}$$

and from the second, more distant one:

$$V_2 = A_2 \cos{(\omega(t-\tau_{\rm g}))}. \tag{43}$$

After multiplying and averaging the signals, we get:

$$R_{\rm c}(\tau) = P\cos{(\omega(\tau_i - \tau_{\rm g}))} = P\cos\left(\frac{2\pi\mathbf{b}\cdot(\mathbf{s}-\mathbf{s}_0)}{\lambda}\right) = Pe^{i\omega(\tau_i-\tau_{\rm g})}. \tag{44}$$

With the introduction of time delay defined in Eq. 41, $\mathbf{s}_0$ is established as the delay tracking center. We receive the maximum power towards the direction of $\mathbf{s}_0$.

4.2 Very long baseline interferometry[6]

Since the development of atomic clocks and phase-stable oscillators, we are not required to connect the elements of our array with optical cables to transmit the local oscillator signal. With the precise time marks provided by the atomic clocks and local oscillators at each station, the antennas are capable of making independent observations, whose data are recorded, and will be correlated later. In some cases, e-VLBI is available, when the data are transmitted via the internet, and are correlated in real-time. Since the baselines are not limited by the length of the optical cables, they can span over several thousands of kilometers, and we can have baselines up to the diameter of the Earth. Alternatively, we can place antennas on satellites as well, so not even the size of our planet will limit our baselines (space VLBI).

With VLBI, we are capable of detecting non-thermal emitters, like active galactic nuclei, pulsars, masers, supernova remnants or magnetically active stars. We can measure their flux, determine the small-scale structure or their precise location (International Celestial Reference Frame/ICRF), obtain their kinematics or distance, or test the signal propagation through the interstellar medium and our atmosphere, and determine antenna location, geodesy.

During the correlation, the signals are aligned in time, and the local oscillator offsets, geometric delays, clock rate offsets and the differential Doppler shift that arises from the rotation of the Earth are accounted for. Then the coherence function is calculated for each baseline. The amplitude and phase of the coherence function give the visibilites measured at a connected interferometer. Currently, there are two types of correlators (XF and FX) in use at different networks, that are distinguished based on the order they perform cross-correlation (X) and Fourier transformation (F) of the data (Titov, Melnikov & Lopez, 2020).

VLBI only differs from connected element interferometry in a few aspects. VLBI uses separate clocks for each station, which results in unknown instrumental phase at every station as well as drifts in this phase. Since the antennas are located several kilometers from each other, the atmosphere (ionosphere and troposphere) is different for each station. Opposed to the connected interferometers, VLBI networks tend to be inhomogeneous, so the calibration of the antennas is more difficult. The phase fluctuations are similar to those of a connected interferometer, but the gradients are worse. VLBI calibrators are poor, because the point sources are variable, and all the bright sources are somewhat resolved, so they need to be imaged before they could be used as calibrators. As a result of this, VLBI uses system temperature, $T_{\rm sys}$ and gain curves for calibration. Geometric model errors from source positions, station locations and the orientation of the Earth can lead to phase gradients, that need to be fringe fitted.

Characteristic scales of a VLBI experiment depend on the sizes of telescopes and their separation. The angular resolution, $\theta \sim \lambda/B_{\rm max}$ depends on $B_{\rm max}$, the longest baseline in the array. The maximum angular scale is $\sim \lambda/2B_{\rm min}$, where $B_{\rm min}$ is the shortest baseline in the array. The target is resolved, if it is larger than the maximum angular scale. Our network is sensitive to angular sizes $\lambda/B_{\rm max} < \theta < \lambda/B_{\rm min}$. The field of view (FOV) of a single antenna is $\sim \lambda/\mathrm{D}$, where D is the diameter of the dish. If the source is more extended than the FOV, then it can be observed with using multiple pointing centers in a mosaic. Since the shortest baseline is larger than the diameter of the antennas, interferometers are not sensitive

[6]This chapter is based on: Wilson, Rohlfs & Hüttemeister (2013)

to large angular scales and cannot recover the total flux density of resolved sources.

Finally, the sensitivity of a synthesis image recorded with N identical antennas observing with $\Delta\nu$ bandwidth for integration time $t_{\rm int}$, is given by:

$$\Delta I_{\rm m} = \frac{1}{\eta_{\rm s}} \frac{SEFD}{\sqrt{N(N-1) \times \Delta\nu \times t_{\rm int}}}. \tag{45}$$

ΔI_m is given in units of Jy/beam, $SEFD$ is system equivalent flux density, i.e., the flux density of a source that would double the observed system temperature, and is assumed to be the same value for all N antennas. It is defined as $SEFD = T_{\rm sys}/G$, where G is the telescope gain. Lastly, $\eta_{\rm s}$ is the system's efficiency. The image sensitivity $\Delta I_{\rm m}$ is the RMS thermal noise expected in a single-polarization image. If simultaneous dual polarization data are available, then for an image of Stokes I, the total intensity:

$$\Delta I = \frac{\Delta I_{\rm m}}{\sqrt{2}}. \tag{46}$$

$\Delta I_{\rm m}$ can also be expressed in the terms of RMS brightness temperature, $\Delta T_{\rm b}$ in Kelvins:

$$\Delta T_{\rm n} \sim 320 \times \Delta I_{\rm m} \sim (B^{\rm km}_{\rm max})^2. \tag{47}$$

4.3 The most notable VLBI arrays and space radio telescopes

The Very Long Baseline Array (Zensus, Diamond, Napier, 1995) consist of ten 25 meter telescopes spread across the United States. They observe in the 0.3 GHz – 96 GHz (90 cm — 3 mm) frequency range, and are capable of reaching 0.17 - 22 milliarcseconds resolution. The longest baseline is 8611 km, between Mauna Kea on Hawaii and St. Croix in the Virgin Islands. The telescopes operate as a VLBI array full time, and are occasionally supplemented by the GBT, the VLA, Effelsberg and recently-damaged Arecibo telescope, and together they form the High Sensitivity Array. A disadvantage of the array is its limited coverage of the southern sky.

The European VLBI Network (Zensus & Ros, 2014), on the other hand consist of antennas that also make single dish measurements, and the only operate as an array for ∼3 months a year. The network consists of 22 antennas with varying sizes, from 10 up to 100 meters in diameter, and they observe in the 0.3–43 GHz frequency range. The telescopes are mainly located in Europe and Asia, with instruments in South Africa and Puerto Rico (although Arecibos has been recently damaged). The longest baseline is ∼10000 km. EVN's disadvantage is that it is a heterogeneous set of antennas, and it has a limited coverage of the southern sky.

The Australian Long Baseline Array (Tingay, 2003) utilises the ATNF telescopes (Parkes, ATCA and Mopra), and the Hobart and Ceduna antennas operated by the University of Tasmania, observing between 1.3 and 22 GHz, covering the southern sky. Occasionally other antennas are added to the array, so LBA, similarly to EVN, is quite heterogeneous. The baselines span ∼3000 km.

The East-Asian VLBI Network (EAVN) (An, Sohn & Imai, 2018) consists of 3 separate arrays. The Korean VLBI Network (KVN) has 4 antennas capable of observing at 22, 43, 86, 129 GHz simultaneously. The Japanese VLBI Network consists of 12 dishes, 4 of those belonging to the VLBI Exploration of Radio

Astrometry (VERA) project. These stations are capable to observe between 2 and 43 GHz. The Chinese VLBI Network adds 4 antennas to EAVN.

The Event Horizon Telescope (EHT) (Johnson et al., 2015) is currently the highest resolution interferometer, aiming for the direct imaging of black hole shadows (like in the case of M87). The array operates at 230 and 345 GHz, and is capable of reaching 20 microarcsecond resolution.

The first dedicated space VLBI telescope was HALCA (Hirabayashi et al., 1998), a project of the Japan Aerospace Exploration Agency, JAXA. The 8 m telescope was launched on February 12, 1997, and retired after a nearly 9-year long mission on November 30, 2005. The telescope was put on a highly elliptical orbit with perigee of 560 km perigee, apogee of 21,000 km and 31 °inclination. The receiver was sensitive to three frequency bands, 1.60/1.73GHz, 4.7/5.0GHz, and 22.0/22.3GHz, but the 22 GHz band was not used for observations due to the loss of sensitivity caused by vibration at launch. HALCA conducted VLBI observations in combination with VLBI networks on the ground. The most notable results of the VLBI Space Observatory Programme (VSOP) were observing the jet from quasar PKS0637-752 with a resolution of 0.2 milliarsecond and a jet from M87 Galaxy with 1 milliarsecond resolution.

The RadioAstron (Kardashev et al., 2013) project was led by Astro Space Center (ASC) of Lebedev Physical Institute of Russian Academy of Sciences (RAS) in collaboration with other institutions. The satellite was launched on July 18, 2011, and it was decommissioned on May 30, 2019 due to equipment failure. The telescope was able to provide interferometer baselines up to 350,000 km, more than ten times larger than that of HALCA. The elliptical orbit of the satellite evolved due to weak gravitational perturbations from the Moon and the Sun. The perigee radius varied from 10,000 to 70,000 kilometers, the apogee radius from 310,000 to 390,000 kilometers, with inclination of 51.6 °. The telescope operated in four frequency bands, 1.3, 6, 18, and 92 cm, the corresponding resolutions of 7, 35, 100, and 500 microarcseconds, respectively. For more details see Table 1. The scientific goals of the mission were the following: to study the central engine of AGN and physical processes near supermassive black holes; investigate the structure and dynamics of star and planets forming regions in our Galaxy and in AGN by studying maser and mega-maser radio emission; observing the scintillations of pulsars and building of high accuracy astronomical reference system of coordinates. RadioAstron was aiming to carry out these observations with unprecedented angular resolution down to a few microarcseconds at 22 GHz. The nominal resolution at this frequency is 7 microarcsecond, the highest resolution of an astronomical instrument ever. In real observations, RadioAstron achieved fringe detection at 8 microarcsecond resolution, which is very close to the theoretical maximum of the instrument.

Band	P	L	C	K
Observing frequency (GHz)	0.327	1.665	4.830	18.392-25.112
Bandwidth (MHz) for each polarization	4	32	32	32
System temperature (K)	70	50	50	60
Antenna efficiency	0.3	0.5	0.5	0.3
SRT sensitivity (Jy)	8200	3500	3500	7000
Maximum resolution (μas)	530	100	35	7

Table 1: Parameters of the RadioAstron receiver system from Kardashev et al. (2013).

5 Observational history of 3C 84

The Fanaroff–Riley type I radio galaxy (Fanaroff & Riley 1974) 3C 84 (optical counterpart: NGC 1275) is a giant elliptical galaxy in the center of the Perseus cluster. Located at redshift 0.0176, its proximity offers a unique opportunity for radio astronomers to study its most striking feature, a two-sided parsec-scale jet, resolved as a one-sided sub-parsec scale structure. The galaxy's Seyfert-like nucleus (Sosa-Brito et al., 2001) harbours a supermassive black hole (SMBH) of 5×10^8 - 2×10^9 $M_\odot$. 3C 84 is often classified as a misaligned blazar.

5.1 Signs of previous activity

3C 84 was a target of radio observations since the 1960's. Kellermann and Pauliny-Toth already noticed its variable nature in flux density and angular diameter (Kellerman & Pauliny-Toth 1966, Kellerman et al., 1971) in the '60s. Some interesting results from this era involve the detection of the counterjet belonging to the VLBI component emitted during the 1959's outburst (Walker, 1994 and Vermeulen, 1994), and the discovery of a correlation between the optical and radio activity (Nesterov, Lyuty & Valtaoja, 1995). Based on the light curve observed by the Metsähovi Radio Observatory, the Crimean Astrophysical Observatory at 22, 37 and 87 GHz, optical UBV data of the Sternberg State Astronomical Institute of Moscow University and archival data, spanning over three decades, the authors conclude that radio outbursts follow optical flaring events with 5-6 years on average, and optical flares appear every ∼8 years. The origin of this variability is the jet, where the faster (∼0.5 mas yr^{-1}) knots cause the shorter timescale variations, while the slowly (0.33–0.39 mas yr^{-1}) expanding plasma of the jet is responsible for the 8 year separation between flaring events. However, in the light of recent activity, these timescales do not hold anymore.

The remnants of earlier activity in 1959 are seen as diffuse emission features located 100 mas and 250 mas. These lobes are propagating with the velocity of 0.3 mas yr^{-1}. Its speed is estimated to fall between 0.3 and 0.5c. Its counterjet, discovered independently by Vermeulen, Readhead, & Backer (1994) and Walker, Romney, & Benson (1994), extended 8 mas from the core at the time of the observations, but has moved northwards since. They also reported that it has a strongly inverted spectral index, explained by free-free absorption due to ionized plasma along the line of sight of the feature.

The observations of Walker et al. (2000) were carried out with the VLBA, occasionally adding a single dish from VLA. The observations were made in 1995 January and October, at 2.3, 5.0, 8.4, 15.4, 22, and 43 GHz. The 2.3 GHz images clearly show the southern feature, and the faint remains of previous outbursts not visible in the higher resolution images, not like the northern counterjet.

The spectral index ($F_\nu \sim \nu^{-\alpha}$) of the southern feature α 0.7, is typical of AGN jets. The northern feature, however exhibits a more variable spectral index, that changes spatially and with frequency, and can reach $\alpha \sim$ -4 between 5 and 8.4 GHz. This steeply inverted spectral index together with the extended nature of the source, suggest free-free absorption, accompanied by some other absorption mechanism to account for the great difference between the optically thick synchrotron spectral index of -2.5 and the spectral index of -4. Other processes that can be responsible for the effect are stimulated Raman scattering or Razin-Tsytovich effect. Raman scattering is an inelastic scattering, that occurs when the

incident photons interact with the molecules, so energy is either gained or lost, and the scattered photons are shifted in frequency. The effect is ruled out because the brightness temperature is inadequately low for the process. Razin-Tsytovich effect is a reduction of the synchrotron emission from a relativistic electron due to the refractive index of the surrounding medium being less than one. The radio source spectrum will show a sharp cut-off below a frequency of $\sim 20n_{\rm e}/B$ MHz, where n_e is the electron density in electrons per cubic meter and B is the magnetic field strength in tesla. Since the effect operates in the emitting region, rather than along the line of sight, it is not adequate to explain the difference between the southern and northern features.

Similarly to the counterjet, the core also has an inverted spectrum, that can be explained with either synchrotron self-absorption, or free-free absorption. After aligning the images, they constructed a two-dimensional distribution of the free-free absorption. Based on these images, the two-dimensional distribution shows a gradient with distance from the core. The absorption is larger near the radio core, and decreases northward on in the counterjet.

Although these observations are not in the direct scope of this thesis work, they give a base of comparison for the properties of the new emission component, and are often cited when describing the environment of the parsec–scale jet.

5.2 Studies on recent activity

5.2.1 The emergence of the new emission feature

The latest activity of 3C 84 was recorded in 2003, when a new VLBI component emerged from the central parsec region of the galaxy. The parsec-scale jet was detected in the data of the Boston University Blazar Group by Suzuki et al. (2012). The appearance of the new VLBI component coincides with the detection of γ-ray emission by Abdo et al. (2009), but there is no unambiguous evidence that the two would be related.

The new jet was first reported in 2010 by Nagai et al. The authors used archival data from VLBI Exploration of Radio Astrometry (VERA) between 2006 and 2008 May at 22.2 GHz. In this dataset, the new emission feature, denoted as C3 first appears in 2007. In the 22 GHz light curve observed by the Effelseberg radio telescope between 1994 and 2010, the flux density of the source decreases until 2004, and after a 2-year gap in the observational data, the flux density starts to rise again in 2006. These observations are consistent with the measurements of the University of Michigan Radio Astronomy Observatory seen in Fig. 11. By measuring the separation between the radio core and the C3 component by fitting Gaussian components to the emission features, the authors were able to determine the apparent speed of the feature to be 0.20 ± 0.01 mas yr^{-1}, and the projected speed is $0.23\pm0.01c$. This gives a constraint on the viewing angle, that is $<45°$. The authors deduce that the jet has emerged with a relativistic speed, then decelerated to sub–relativistic speeds over the projected distance of 0.8 mas or 0-28 pc.

Suzuki et al. (2012) used the observational data of this work, supplemented with new VLBA 43 GHz data obtained between January, 2002 and November, 2008, and archival data of the Metsähovi 14 m radio telescope between 2001 December and 2008 December. The VLBI component, C3 is already visible

in the 43 GHz images in November, 2003, whereas with the lower resolution 22 GHz images they were only able to detect it in 2007. During the time of the observation C3 became gradually brighter, and its separation increased from the core, consistently with previous results (Nagai et al., 2010).

To evaluate the evolution of the jet and measure its speed, they compared the position of the peak brightness of C3 to the radio core (Fig. 10), then parametrized the motion of the jet as a second order polynomial in the parallel and perpendicular directions. From the peak positions marked on the figure, it can be seen that C3 is moving on a different trajectory than suggested by the direction of the sub–parsec jet. The jet direction has also changed since the 1990s. This swinging jet motion will be discussed later in connection with results of this work. The speed at the time of the emergence is 0.09 ± 0.04 mas yr^{-1}, and accelerates to 0.41 ± 0.07 mas yr^{-1} by 27 November, 2007, the detection in Nagai et al. (2010). These values correspond to the apparent speeds of $\beta_{\rm app} = 0.10 \pm 0.05$ and 0.47 ± 0.08 mas yr^{-1}, respectively.

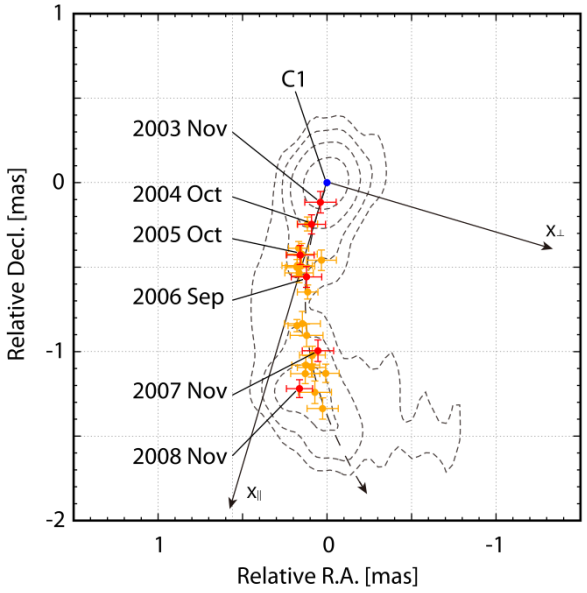

Figure 10: Change in the peak positions of C3 through the observational epochs in Suzuki et al. (2012). The dashed line represents the motion of the peak position, and the change in coordinates are computed in the frame defined by the $x_{\rm par}$ and $x_{\rm perp}$ axes.

Using the archival 37 GHz data of the Metsähovi radio telescope (León–Tavares et al., 2011) and flux densities of the three emission components determined from the 43 GHz maps of the source, the authors constructed light curves between 2002 and 2009 (Fig. 11). The light curve show similar trends, but the total flux density measured by Metsähovi is always ~ 5 Jy higher than the total flux density from the 43 GHz data, suggesting that the variability arises from the central region. The flux density rises from the beginning of the observations, more rapidly after 2007.

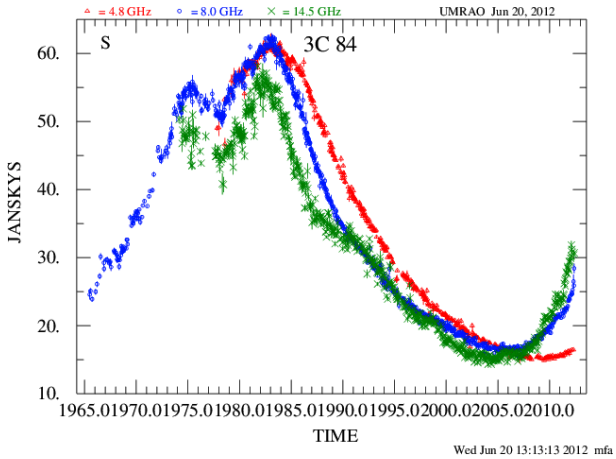

(a) The longest spanning light curve measured UMRAO monitoring program between 1965 and 2012 at 4.8, 8 and 14.5 GHz.

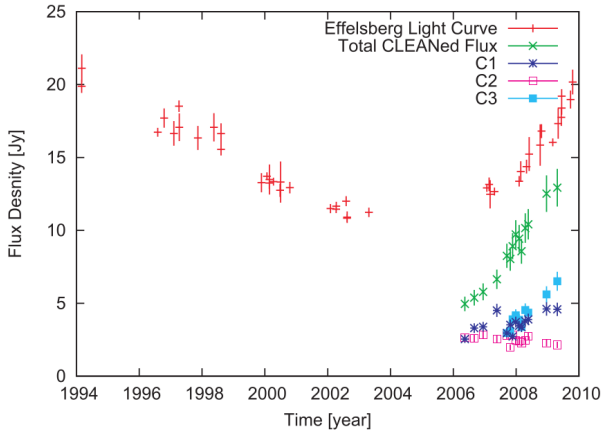

(b) Light curves obtained by Effelesberg at 22 GHz (plus signs), of total cleaned flux density of VERA observation also at 22.2 GHz (crosses), and light curves of components C1 (asterisks), C2 (open squares) and C3 (filled squares). From Nagai et al. (2010).

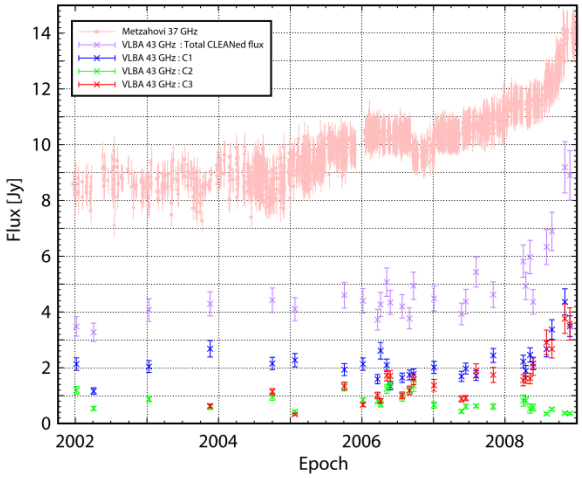

(c) Light curves obtained with VLBI and single-dish measurements (Suzuki et al., 2012), marked by the magenta and pink points, respectively. Blue points stand for C1, green for C2, and red for C3.

Figure 11: Light curves of 3C 84. All three of them show a similar trend of increasing flux density in the beginning of the 2000's, marking the emergence of the parsec–scale jet.

The highest resolution observations were carried out by Giovannini et al. (2018), who observed 3C 84 on September 21, 2013, with the Global VLBI Network and RadioAstron, reaching the baselines of 16 Earth radii. They observations resolve the two-sided sub–parsec scale structure already 30 microarcseconds from the radio core. The sub-parsec scale structure consists of the radio core, C1, the diffuse, slowly moving emission feature, C2, the restarted jet spanning 3 mas to the south, moving with the velocity of $<0.5c$, ending in a hotspot, C3. There is also an indication of the counter-jet northwards from the core. The images of the central parsec region are shown in Fig. 12.

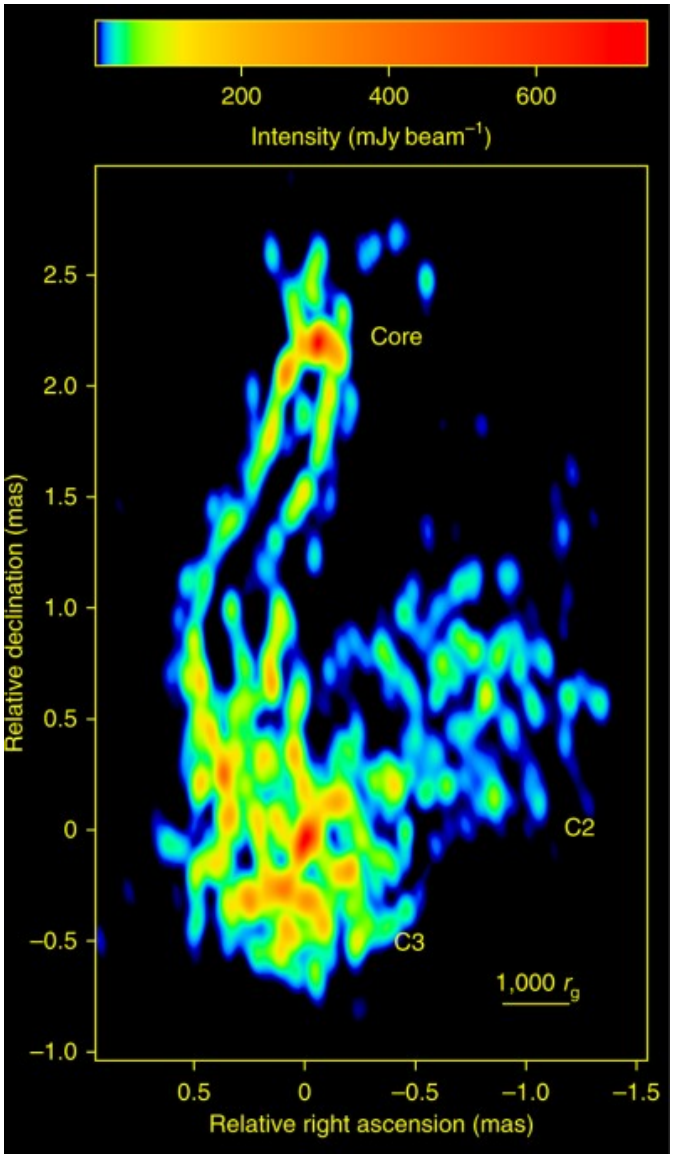

Figure 12: Image of the central parsec region of 3C 84 from Giovannini et al. (2018). The main features are marked on the image. C2 is a slowly moving, diffuse emission feature, and C3 is the hotspot at the end of the parsec-scale jet. The half-power beam width (HPBW) is 0.10 × 0.05 mas. The image has a noise level of 1.4 mJy/beam and peak intensity of 0.75 Jy/beam.

Abdo et al. (2009) reports the detection of γ-ray emission consistent with a point source originating from 3C 84. Their observed the galaxy with the Large Area Telescope (LAT) on the Fermi Gamma-ray Space Telescope between August 4 and December 5 in 2008. The galaxy was previously observed with EGRET, but was not detected as a γ-ray source. The upper flux limit of these observations were $F_\gamma < 3.72 \times 10^{-8}$ (>100 MeV) cm^{-2} s^{-1}, whereas the Fermi observations determine the flux to be $F_\gamma < (2.1 \pm 0.23) \times 10^{-7}$ (>100 MeV) cm^{-2} s^{-1}, seven factors higher than the EGRET upper limit. This suggests that 3C 84 is variable on timescales of years to decades, and the emission originates from a region with the size of R $\leq$ ct $\approx$ 0.3 pc. Abdo et al. (2009) also constructed the spectrum of the galaxy between 200 MeV to 25 GeV with a single power-law: $F(E) = k(E/E_0)^{-\Gamma}$. The fit parameters were k=(2.45±0.26)×10^{-9}, E_0=100 MeV and Γ=2.17±0.05, where Γ is the photon index.

5.2.2 Long-term programs involving 3C 84

3C 84 was monitored by several research groups throughout the decades. The first program was started by UMRAO in 1965, and was finished in 2012. The program utilizes a 26 meter telescope which operates at 4.8, 8 and 14.5 GHz with bandwidths 560, 760, and 1600 MHz, respectively. The light curve produced show two-week averages of the total flux density in the three observing frequencies, but only the 8 GHz measurements span over the whole time range of the program. The flux density reached its maximum around 1984, then faded until 2005, when the flux density started to rise again, probably marking the launching of the new jet.

The Monitoring Of Jets in Active galactic nuclei with VLBA Experiments or MOJAVE program monitors radio brightness and polarization variations in active galactic nuclei jets of the northern sky (Lister et al., 2018). Their observations on 3C 84 started in 1995. They regularly observe the source with the VLBA at 15 GHz, provide total intensity images and report the fraction of linear polarization and electric vector position angles (EVPA).

The Boston University Blazar Group ((Jorstad & Marscher, 2016, Jorstad et al., 2017)) is conducting a multi-frequency observations of blazars, where the 43 GHz VLBA measurements are supplemented by optical and γ-ray data. They started to monitor 3C 84 in 2010, and similarly to MOJAVE they provide Stokes I, P and EVPA maps.

These monitoring programs are crucial part of studying the variable nature of AGN jets, because the provide a consistent dataset spanning over several decades, that enable us to study the sources' evolution on timescales longer than general VLBI observations .

5.2.3 Detection of the counterjet

Fujita & Nagai (2016) reported the detection of a counterjet (Fig. 13) based on the calibrated data of the MOJAVE and the Boston University Blazar Group obtained with the VLBA at 15 GHz on the January 22, 2016 and at 43 GHz on December 5, 2015. The image of the central region shows a lobe-like feature extending southward, ending in a hotspot. They detect the northern feature with peak brightness of 17 mJy beam^{-1} and 17σ at 15 GHz, and 23 mJy beam^{-1} and 24σ at 43 GHz. The estimated apparent velocity of the southern component is β_a=0.23±0.001 (Nagai et al 2010). The ratio of the apparent lengths of the jet and the counterjet are derived from the 43 GHz image, where the

positions are determined with Gaussian fits, and the apparent length ratio is given by the distance from the core to C3, and the distance from the core to N1. The derived ratio is, D=1.22±0.16. They obtain inclination angle of θ=65±16° and normalized jet velocity, β=0.23±0.02. Viewing angle estimates for the recent activity range from 18°to 65°(Nagai et al., 2014: 25°, Giovannini et al., 2018: 18°and 45°, and in the currently discussed paper 65°), whereas the previous activity had viewing angle of <45°(Walker et al. 2000).

The derived the spectral indices for the emission features are: α_{C3}=0.91, typical for synchrotron emitting regions, and α_{N1}=-1.61, indicating an inverted spectrum. Together with the large inclination angle, this suggests that the black hole is surrounded by an optically thick accretion disk, perpendicular to the jet axis, and it obscures the northern component.

The derived brightness ratio, on the other hand, does not match the with the observed values. The observed brightness ratio at 15 GHz is R_{obs}=600, and at 43 GHz R_{obs}=45, indicating that the northern feature is absorbed by the accretion disk. These all suggest free-free absorption, similarly as in Walker et al. (2000).

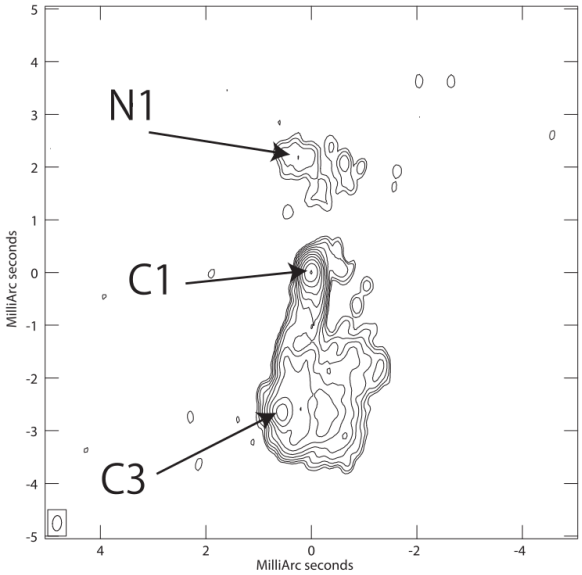

Figure 13: VLBA image of 3C 84 at 43 GHz from Fujita & Nagai (2017). The core, the southern hotspot and the northern feature are indicated as C1, C3 and N1, respectively. The contour levels are 2.9 mJy × (1, 2, 4, . . . , 1024). Beam FWHM is 0.289 × 0.171 mas at a position angle of -4.93°.

5.2.4 Limb brightening and collimation profile measurements

Limb– or edge–brightening is feature of AGN jets, where the outer layer, sheath of the jet appears brighter than the inner region called spine. It is due to this spine-sheath structure in the jet, where a slow, cylindrical flow of denser plasma envelops a flow of ultra-relativistic material. It is possible that the high-energy emission originates from the spine, and the sheath is responsible for the radio emission. In this scenario FRI galaxies, that exhibit lower Lorentz factors and intrinsic jet powers, are sheath-dominated, while BL Lac objects are spine-dominated (Hovatta et al., 2009). The spine-sheath interaction also reconcile the difference between the observed low Lorentz factors and the high energy

emission modelled in the SEDs of TeV BL Lacs (Ghisellini et al., 2005). The origin of this transverse structure is not yet clear. The sheath might originate from the accretion disk, whereas the the spine is launched from the ergosphere of the central black hole (Boccardi et al., 2016).

The limb brightened structure is interpreted to be a result of a higher Doppler factor or a higher synchrotron emissivity in the sheath compared to the spine. In the case of a fast spine and slower sheath, if the jet points away from the line of sight at a relatively large angle, than the slower sheath can be Doppler boosted to become brighter than the high-velocity spine (Giovannini, 2003). This scenario works well for explaining the structure of Mrk 421 and Mrk 501 (Giroletti et al., 2006). Alternatively, the limbs can acquire a higher synchrotron emissivity. The higher emissivity can be caused by shear acceleration of electrons at the jet boundary (Sahayanathan, 2009) or a pileup of material along the jet boundary (Zakamska et al., 2008). Limb brightening can also be explained by Kelvin–Helmholtz instability acting at the jet boundary (Kovalev et al., 2007). A transverse velocity structure can also account for limb brightening. In this case, the jet exhibits a transverse gradient in the bulk Lorentz factor, with the Lorentz factor decreasing towards the edges (Piner et al., 2010). Finally, a helically wrapped filament around the jet, like in the case of M87 (Owen et al., 1989), can also account for the brightened limbs.

Nagai et al. (2014) observed 3C 84's restarted jet with the Very Long Baseline Array at 43 GHz on January 24, 2013. They report the first detection of a limb-brightened structure in the parsec-scale jet, indicating a change in the transverse structure.

The image is shown in Fig. 14. The main emission features are denoted as usual. The one-sided jet structure along with the limb-brightening is clearly visible along the restarted jet. Comparing their results with images of the Boston University's Blazar Group (Jorstad & Marscher, 2016, Jorstad et al., 2017), they find that limb-brightening was already present at the beginning of the monitoring program on November 1, 2010, but it appeared after April, 1999 (Lister, 2001). Since the limb-brightened structure appeared during the epoch of enhanced γ-ray emission, and ridge-brightening was present during the γ-quiet phase, this transition is best explained by a change in the transverse velocity structure in the spine-sheath model.

The outflow velocity of the limb brightened region can be estimated with the assumption that the transverse brightness is uniform, and it is only affected by transverse velocity structure, resulting in the variation of the Doppler factor in the axisymmetric layers. Based on these assumptions, the Doppler factor will be at its maximum in the jet sheath. The Doppler factor reaches its maximum where the bulk Lorentz factor is about 2.4, so the velocity of the sheath is $\Gamma \sim 2.4$ and the spine's is $\Gamma > 2.4$. These velocity constraints depend on viewing angle of the jet, but it cannot be measured, unless the counter-jet is detected. The non-detection of the counter-jet is due to the Doppler effect and free-free absorption (Walker et al., 2000) Since the Lorentz factor of the sheath is somewhat faster than the velocity of C3 measured with VLBI in the previous papers, it suggests that C3 is a terminal hotspot, and does not directly reflect the flow's properties.

In the observations of Giovannini et al. (2018) the two limbs are already resolved at a projected distance of 30 milliarcseconds (see Fig. 14) from the core, ten times closer from the core than achieved in previous observations. They interpret the structure as a result of a change in the transverse velocity structure, a change in emissivity or interaction with the surrounding medium, or the superposition of

these effects. Since the spine becomes brighter as it approaches the hotspot , the flow is either slowing down or particle acceleration in C3 results in increased emissivity as shocks are formed where the jet meets the interstellar medium.

The good resolution of the calibrated image in Nagai et al. (2014) enabled the authors to measure the jet collimation profile in slices at every 0.15 mas from the radio core along PA 10°, up to 1.5 mas. Two Gaussian components were fitted on the jet edges, and the separation between their peaks represents the width of the jet. The first slice was represented by a single Gaussian, due to the lack if resolution. Here, the FWHM of the Gaussian fit is interpreted as the jet width.

According to Komissarov et al. (2009), the jet profile is parabolic when the external pressure scales with the distance from the radio core as $p_{\rm ext} \sim z_{\rm obs}^{-a}$, and a <2. The jet is conical when a >2. For the jet width, the relation is $W_{\rm j} \sim z_{\rm obs}^{a/4}$. The jet width profile of 3C 84 between 10^3-10^5 r$_g$ can be fitted with a power-law with index of 0.25±0.03 (Fig. 15). This quasi–cylindrical collimation profile opposed to M87's parabolic one suggests different circumnuclear environments in the two galaxies.

Giovannini et al. (2018) performed the same analysis, and measured the collimation profile of the jet between the de-projected distance of 350 and 8000 $r_{\rm g}$ in perpendicular slices in the jet direction. The collimation profile (Fig. 15) is almost cylindrical $r \propto z_{\rm obs}^{0.17\pm0.01}$, which is in good agreement to the measurements above. The first two collimation profiles available in the literature, for M87 in Nakamura et al. (2018), $r \propto z_{\rm obs}^{0.56\pm0.01}$ between the de-projected distance of 200 and $4{\times}10^5$ $r_{\rm g}$, and for Cygnus A in Boccardi et al. (2016), $r \propto z_{\rm obs}^{0.55\pm0.07}$ between 500 and 10^4 $r_{\rm g}$. These are both parabolic, opposed to the cylindrical profile of 3C 84, that could be due to the young dynamic age of the restarted jet. On the other hand, kiloparsec scale jets can create cavities forming a constant pressure cocoon (Rayburn, 1977) that is capable of recollimating the flow into a cylindrical shape before it enters hotspot. 5 GHz observations carried out with RadioAstron (Savolainen, 2018) confirm the existence of a low–intensity cocoon around the jet. They argue that in this scenario C3 corresponds kiloparsec–scale hotspots.

The apparent jet opening angle is measured to be α_o=2 arctan$(r/z_{\rm obs})$ = 130±10°, and the intrinsic opening angle is α_1=2arctan[tan$(\alpha_o/2)$sinθ]∝70°. This is the largest intrinsic opening angle measured so far in radio galaxies. The most important result of Giovannini et al. (2018) is the measured wide jet width, $r \approx 250$ $r_{\rm g}$ at ≈350 $r_{\rm g}$ from the core. This suggest that the jet is either launched from the accretion disk or in the case it is launched from the ergosphere, it expands extremely rapidly in lateral direction below ∼100 $r_{\rm g}$. This results is directly connected to distinction between the Blandford–Znajek and Blandford–Payne mechanisms, and these results could be tested in this thesis.

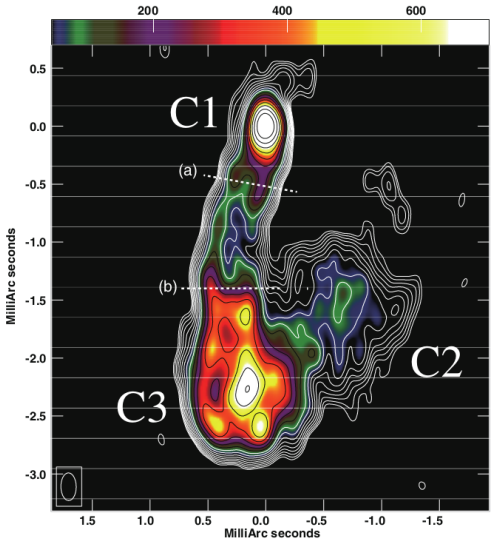

(a) 43 GHz map of 3C 84 from Nagai et al. (2014). The contours are at 5.43 mJy beam^{-1} × (-1.41, 1, 1.41, 2.83, 4, 5.66, 8, 11.3, 16, 22.6, 32, 45.3, 64, 90.5, 128, 181, 256) , and the peak intensity is 2.17 Jy beam^{-1}. The FWHM of the convolved beam is 0.24 x 0.13 mas at the position angle 0.69°.

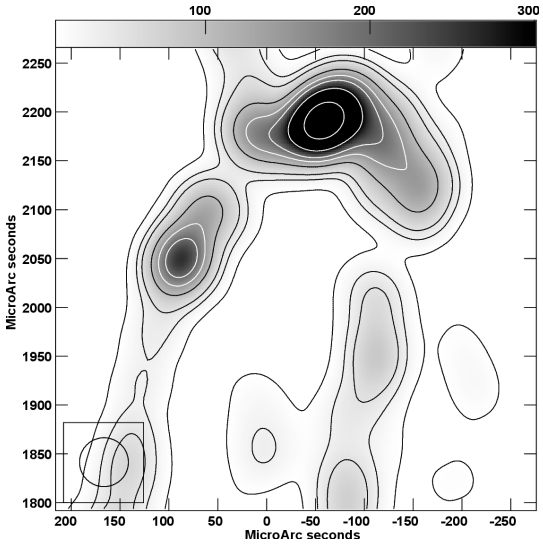

(b) Innermost region of the parsec-scale jet observed by Giovannini et al. (2018). HPBW is 0.05 × 0.05 mas. The noise level is 1.5 mJy/beam and the peak intensity is 0.66 Jy/beam. Contours are at 10, 30, 50, 100, 150, 200, 300, 500 mJy/beam.

Figure 14: Limb-brightened structure of the parsec-scale jet.

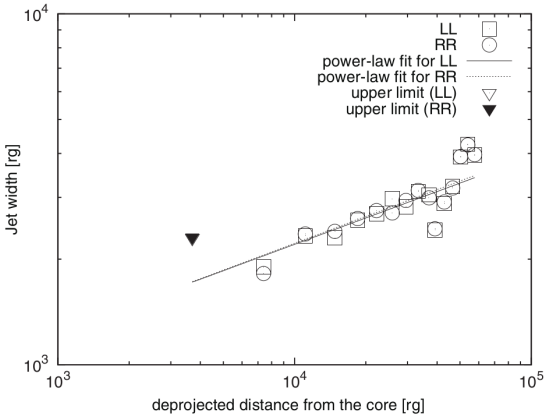

(a) Collimation profile of the restarted jet from Nagai et al. (2014). The filled triangle is the upper limit for the first jet width measurement. The open squares and circles represent the jet width measurements in the RR and LL maps. The x axis is the de-projected distance with the viewing angle of 25°and black hole mass of 3.4 × 10^8 $M_\odot$. The lines represent the power-law fits with indices 0.25±0.03.

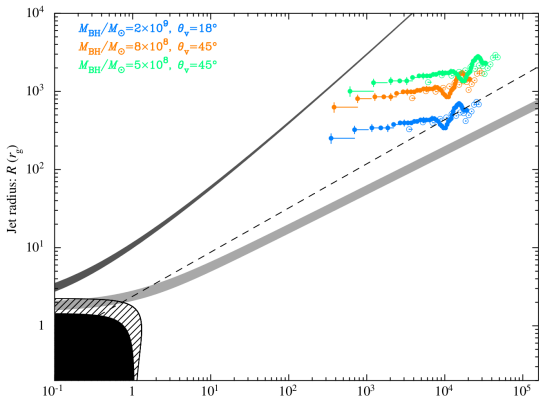

(b) Jet width profile as a function of de-projected distance from Giovannini et al. (2018). Filled points are RadioAstron data, while the others are from Nagai et al. (2014) with three different assumptions on jet viewing angle and black hole mass. The dashed line is the power-law collimation profile for M87 (Nakamura et al. 2018), and the hatched area represents the ergosphere for a black hole with spin parameter a = 0.998.

Figure 15: Jet width profile measurements of Nagai et al. (2014) and Giovannini et al. (2018) both estimate the collimation profile to be cylindrical, that is probably due to the young dynamical age of the jet.

5.2.5 Spectral energy distribution of 3C 84

The detection of high energy emission orignating from 3C 84 enabled Abdo et al. (2009) to construct a broadband spectral energy distribution (SED) from the radio (RATAN-600), radio core (MOJAVE), optical (MITSuME), optical/UV (Swift/UVOT), radio to X-ray (NED), nonthermal X-ray nuclear emission (Balmaverde et al., 2006), hard X-ray (Swift/BAT, based on Ajello et al. 2009), gamma (EGRET upper limit from Reimer et al., 2003), Whipple upper limit (Perkins et al., 2006), and Fermi data. Since the γ-ray, optical and low-frequency radio fluxes have similar magnitudes, the SED is comparable to those of low-frequency-peaked BL Lac objects described in the AGN unification section. They use two models to fit the SED.

The first is a one-zone synchrotron self-Compton model with a jetted outflow and (Finke et al., 2008), designed for analysis of the broadband data from high-energy peaked BL Lacs, by assuming that the synchrotron radiation is originating from isotropically distributed electrons in the randomly oriented magnetic field of a relativistic blazar jet. This model, with bulk Lorentz factor Γ=1.8, Doppler factor δ=2.3, observing angle θ=25° gives a result that is consistent with the mildly relativistic outflow of 3C 84.

The second fit was the decelerating flow model of Georganopoulos & Kazanas (2003), where the TeV emission originates from a decelerating jet. This assumption resolves the contradiction between theory - BL Lacs are the small viewing angle ($\theta \sim 1/\Gamma$) counterparts of FR I radio galaxies (Urry & Padovani, 1995) - and observation - small apparent velocities measured in subparsec regions of TeV BL Lacs (Marscher, 1999). In this model the 'synchrotron photons from the slower regions of the flow are Compton-scattered by energetic electrons in the faster, upstream part of the flow'. The bulk Lorentz factor decelerates from Γ_{max}=10 to Γ_{min}=2 over the distance of 5x10^{17} cm.

The SEDs resulting from these fits are shown in Fig. 16. For more detailed description of the SED models see Abdo et al. (2009) and the references therein.

Although these fits seem to describe the observational results accurately, Nagai et al. (2010) argues that the one-zone SSC is not adequate for the C3 component based on their measured sub-relativistic speed (projected speed of 0.23±0.01c) of the feature. This contradiction can be resolved by introducing a spine-sheath structure, where the faster spine is responsible for the Tev emission by inverse Compton scattering the radio photons originating from the surrounding slower sheath (Ghisellini et al., 2005) This spine-sheath structure was indeed detected in later works of Nagai et al. (2014) and Giovannini (2018), and it exists in M87 (Kovalev et al., 2007) and Mrk 501 (Giroletti et al., 2004).

Suzuki et al. (2012) also attempted to fit the SED with the one-zone SSC model on the data presented in Abdo et al. (2009), adding an extra component from their 43 GHz VLBA observations on August 27, 2008. The apparent velocity was $\beta_{\rm app}$=0.44c at this epoch. Adopting the same viewing angle of the previous fit, 25°, the intrinsic jet speed gives β=0.54c, corresponding to a bulk Lorentz factor Γ=1.19, and Doppler factor δ=1.65. The Gaussian model fit determines the size of C3 to be ∼0.2-0.3 mas.

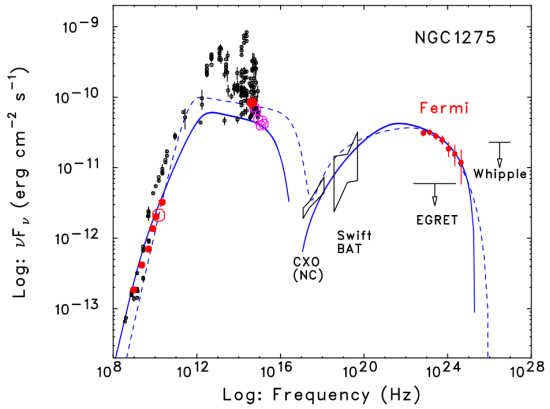

(a) SED from Abdo et al. (2009) constructed from multiband data. The one-zone SSC model is plotted with dashed, while the decelerating flow model is plotted with solid curves. The observational data: RATAN-600 in filled red circle, MOJAVE in open red circle, MIT-SuME in red, Swift/ UVOT in open magenta circle. For references see the text.

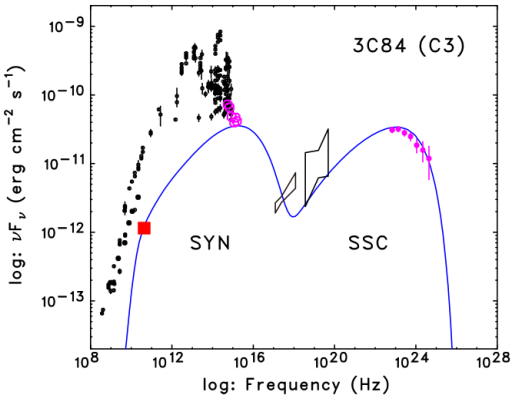

(b) SED from Suzuki et al. (2012). The black and magenta markers are from Abdo et al. (2009), and the red square is the VLBA flux density of C3. The blue line is the fitted one-zone SSC with parameters. Based on the fit, C3 in itself cannot account for the synchrotron and self-Compton emission in the model.

Figure 16: Spectral energy distribution of 3C 84.

The results of Suzuki et al. (2012) (size of the emitting region, R=1.45x10^{17} cm; mean magnetic field strength, B = 0.37 G; normalization factor, $q_e = 5{\times}10^{-7}$ cm^{-3} s^{-1}; power-law index s = 1.2; and γ_{min}=1 and γ_{max}= 7.5$\times$10^4 are the maximum and minimum Lorentz factor for the injection spectrum) are inconsistent with the previous fit parameters (Fig. 16). When they adopt the same minimum Lorentz factor for the injection spectrum (Kino et al., 2002), the resulting spectral index significantly differs from the observed value between 22 and 43 GHz. By raising the Lorentz factor they get the fit shown in Fig 16, but the spectral index still not matches the observed value. Based on this, C3 in itself cannot account for the synchrotron and self-Compton emission in the model.

5.2.6 Polarimetric observations

VLBA 43 GHz polarimetric observations of Nagai et al. (2017) reveal significant polarized emission originating from the hotspot at the end of the parsec-scale jet (Fig. 17). They used data from five epochs of the Boston University Blazar Group's monitoring program (Jorstad & Marscher, 2016, Jorstad et al., 2017), and detected polarization percentage between 1 and 3% throughout all epochs in a compact region. The enhancement of polarized emission coincides with the hotspot's movement from the western to the eastern limb of the jet. Consistently with numerical simulations of Wagner et al. (2012), these facts suggest an inhomogeneous ambient medium, that causes the movement of the termination shock.

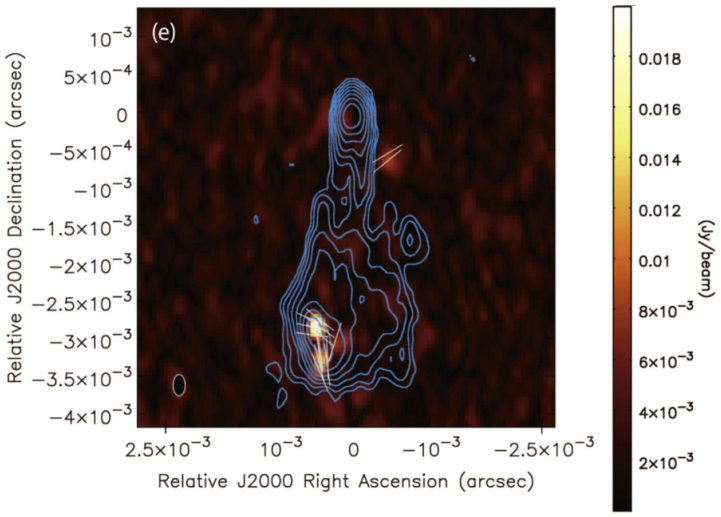

Figure 17: VLBA image of 3C 84 on April 22, 2016 (Nagai et al., 2017), showing the polarized emission from the hotspot. The polarized intensity is shown in color, and the total intensity is marked with the cyan contours with levels $3\sigma\times$ (-1, 1, 2, 4, ..., 2048). The polarization position angles are indicated by the white vectors, and the restoring beam size is 0.28 × 0.16 mas at a position angle of 0°.

The electric vector position angle (EVPA), corrected for Faraday rotation, changes over a timescale of a month, indicating a rapid change in the projected magnetic field direction within the hotspot.

The rotation measure (RM) is determined to be of order $\sim 10^5$ rad m^{-2} $\sim$1 pc from the base of the jet, that is slightly variable on monthly timescales. The variation timescale suggest that the size of the hotspot is $\sim$ 0.07 mas, similar to the 0.05 mas in Giovannini et al. (2018). The measured RM is two orders higher than the RM of 7000 rad m^{-2} reported by Taylor et al. (2006), from the 10 mas ($\sim$8 pc) scale lobe in 2004, and is the same order as the RM (9x10^5 rad m^{-2}) derived from millimeter interferometric observations by Plambeck et al. (2014). The decrease in RM indicates that the Faraday screen must be located between 1 and 8 pc.

The most likely cause that can account for the decrease in the RM is a radiatively inefficient accretion flow (RIAF, Narayan & Yi, 1995). that also gives accurate estimate for the accretion rate calculated from the bolometric luminosity. RIAFs in 3C 84 are suggested by its low bolometric luminosity, which is only 0.4% of the Eddington luminosity. Based on numerical simulations (Merloni & Fabian, 2002), RIAFs can coexist with cold ($T_e \sim 10^4$ K), disk-like accretion flows, detected by Walker et al. (2000) via identifying the free-free absorption in the counter jet, together with an inhomogeneous gas distribution around the black hole (Fujita et al., 2016). These features can be present at the same time in a stratified structure.

The difference in the RM can also be explained by a gas clump with size of the limb width ($\sim$0.1 mas) sitting on the hotspot. Introducing this inhomogeneous ambient medium, they can also account for the movement of the hotpot from the western to the eastern limb. Compared to the mean electron density of 8.1 cm^{-3} on parsec scales derived by Fujita & Nagai (2017), the gas clump has an electron density three orders of magnitude higher, 2×10^4 cm^{-3}, consistent with the one inferred for the narrow-line region (Osterbrock, 1991). The inhomogeneous gas density of the cloud can also account for the slight variation of the RM.

From the positive sign of the RM reported by Nagai et al. (2017), Taylor et al. (2006) and Plambeck et al. (2014), the magnetic field configuration is implied to point towards the observer at three different locations, suggesting a radial magnetic field in the ambient medium. From the equipartition magnetic field of 24 μG and radial magnetic field configuration $B(r) \sim r^{-2}$, the field strength at 1 $r_{\rm S}$ is $1.6{\times}10^4$ G, the same order of magnitude as the magnetic field strength measured in at the jet base of BL Lacs (O'Sullivan & Gabuzda 2009).

6 Observations

The observations were made in 2016, between September 11, 13:00 UT and September 12, 19:00 UT, with the total observing time of 30 hours. The participating ground telescopes in the 5/22 GHz observations were 10 Very Long Baseline Array (VLBA) stations, 3 Korean VLBI Network (KVN) stations, 16 European VLBI Network (EVN) stations, supplemented with RadioAstron. The characteristics of the antennas that produced data are presented in Table 4. In addition to the target, two calibration sources were observed (Table 2). The observations were carried out with dual (leaft and right) circular polarizations in two sub–bands called intermediate frequencies (IFs), with 16 MHz bandwidth and 256 spectral channels each. The spectral channels had 62.5 kHz bandwidth (Table 3). The recording rate of the RadioAstron satellite was 128 Mbps, whereas the ground array antennas recorded data with a 256 Mbps rate. The data were correlated with a 0.25 integration time at the Max-Planck-Institut für Radioastronomie in Bonn, Germany using a DiFX software correlator that had been modified to allow correctly calculating the path delays for an orbiting antenna taking into account special and general relativistic effects (Deller et al. 2007, 2011, Bruni et al. 2016.).

Source	Type	RA(2000.0)	Dec(2000.0)
0316+413	target	03:19:48.1601	41:30:42.106
0300+470	primary calibrator	03:03:35.2422	47:16:16.275
1823+568	secondary calibrator	18:24:07.0684	56:51:01.491

Table 2: Observed sources.

Sub–band (IF)	Frequency (GHz)	Bandwidth (kHz)	Channel separation (kHz)
1	22.22	16000.001	62.5
2	22.236	16000.001	62.5

Table 3: Properties of the two sub-bands/IFs of the observation.

Antenna	Latitude	Longitude	Country	Diameter (m)	SEFD at 22 GHz (Jy)
Badary	51°46' 11.6" N	102°14' 4.95" E	Russia	32	710
Brewster	48°7' 52.21" N	119°40' 59.7" W	USA	25	640
Effelsberg	50°31' 29.4" N	6°53' 01.0" E	Germany	100	90
Fort Davis	30°38' 6.77" N	103°56' 41.38" W	USA	25	640
Hartebesthoeek	25°53' 25" S	27°41' 08"E	South Africa	26	3000
Hancock	42°56' 1.03" N	71°59' 12.52" W	USA	25	640
Kitt Peak	31°57' 22.51" N	111°36' 44.5" W	USA	25	640
Tamna	33°17' 18' N	126°27' 43" E	South Korea	21	1288
Ulsan	35°32' 33" N	129°15' 04" E	South Korea	21	1288
Yonsei	37°33' 44" N	126°56' 35" E	South Korea	21	1288
Los Alamos	35°46' 31.04" N	106°14' 44.12" W	USA	25	640
Medicina	44°31' 15" N	11°38' 49" E	Italy	32	700
Metsähovi	60°13' 05" N	24°23' 38" E	Finland	14	2608
Mauna Kea	19°48' 5.72" N	155°27' 20.92" W	USA	25	640
North Liberty	41°46' 17.94" N	91°34' 26.88" W	USA	25	640
Noto	36°52' 34" N	14°59' 21" E	Italy	32	800
Onsala	57°23' 35" N 11°	55' 04" E	Sweden	25	1380
Owens Valley	37°13' 54.34" N	118°16' 37.7" W	USA	25	640
Pie Town	34°18' 3.85" N	108°7' 8.83" W	USA	25	640
RadioAstron	-	-	Russia	10	46700 (LCP) 36800 (RCP)
St. Croix	17°45' 23.47" N	64°35' 1.54" W	USA	25	640
Svetloe	60°31' 56" N	29°46' 54" E	Russia	32	710
Yebes	40°24' 30" N	3°41' 15" W	Spain	40	200
Zelenchuskaja	43°47' 16.2" N	41°33' 52.6" E	Russia	32	710

Table 4: Location, diameter and system equivalent flux density (SEFD, from EVN Calculator: http://old.evlbi.org/cgi-bin/EVNcalc) of the observing antennas. SEFD is defined as the flux density of a radio source that doubles the system temperature. The lower the SEFD is, the more sensitive the antenna is.

7 Data reduction

To maximize the sensitivity in fringe search on ground–space baselines, it is necessary to coherently combine data on several such baselines, which requires a fully self–calibrated ground array and a source model constructed from the ground array data. As a result of this, calibration and imaging is first done for the higher signal-to-noise ratio data of the ground array, then the clean image of this step is used to find fringes for RadioAstron. The final image will consist of data from the whole array.

7.1 Calibration of the ground array

The calibration of the data was carried out in the National Radio Astronomy Observatory's Astronomical Image Processing System (`AIPS`, Greisen 2003). AIPS is a software that enables interactive calibration and editing of VLBI data, using the Fourier synthesis method. Calibration is crucial step in which one corrects for various instrumental and propagation effects affecting the measured visibility amplitudes and phases. In this step, the measured raw correlation coefficients (i.e., visibility amplitudes) are converted to physical units (i.e., correlated flux densities in Jy).

In `AIPS`, the more complex programs are incorporated as tasks where the inputs can be specified by the user by passing strings, numbers, arrays to adverbs. Verbs work in a similar manner, but they are smaller routines than tasks.

The calibration procedure (a typical example is presented in Zensus, Diamond & Napier (1995) and in the `AIPS` CookBook) starts with uploading the UV-FITS data to AIPS using the `FITLD` task. This creates the first calibration or CL table, which contains default calibration parameters for the amplitude (usually unity), phase, and single-band delay (usually zero) for each IF of the sources involved in the observation, as a function of time. It also contains polynomial coefficients that allows the user to recompute delay and phase models established at the correlator. During the calibration procedure, higher versions of the CL table are created to incorporate more and more calibration effects into the phase, delay, and amplitude entries.

The next step is to run `VLBAUTIL`, that defines procedures for the reduction of data collected with the VLBA, and which can be in many cases used for other VLBI arrays as well. `VLBAFIX` is one of such tasks. It sorts the data, creates an index table - containing the list of scans, antennas and sources - and a CL table. After these procedures one can view the antenna table and scans with `VLBASUMM`.

The task `ANTAB` reads in auxiliary data necessary for amplitude calibration, such as system and antenna temperatures and gain curves, and creates the first system temperature and gain curve tables, both of which will be used later on for amplitude calibration. Since the system temperature table sometimes contains erroneous measurements, one has to go through the editing of these outliers in the interactive window of `SNEDT`.

The parallactic angle (the angle between the vertical at the antenna and the direction of north at the observed point) corrections defined in `VLBAPANG` should be applied before any other phase corrections are done. This step is necessary because for antennas with altazimuth mounts tracking the source in hour angle, the parallactic angle varies with the hour angle, causing the antenna response pattern to rotate on the sky. In VLBI, the great distances between antennas result in different parallactic angles at different

stations, which must be taken into account. For circularly polarized feeds, antenna rotation only rotates the RL and LR visibilities, whereas RR and LL visibilities are unaffected. Since Stokes I (total intensity) and V parameters require only parallel hand correlations, they are not affected by the different parallactic angle at the antennas. For linearly polarized feeds, however, both parallel and cross–hand correlations change as a function of parallactic angle.

The `VLBACCOR` procedure applies digital sampling corrections to the calibration table. Digital samplers sample the voltages of the analog signals at periodic intervals, then quantize the sampled value of the voltages with a small number of bits. The small bit number quantization results in a quantization noise, for example due the loss of sensitivity in digitizing the analog signal (`AIPS` CookBook). `VLBACCOR` runs `ACCOR` to calculate cross–correlation amplitudes for imperfect samplers. `ACCOR` determines amplitude corrections from autocorrelation spectra mean values of all antennas in a VLBI network. The correlator of EVN at the Joint Institute for VLBI ERIC (JIVE) opposed to the correlator of the VLBA, performs this calibration prior to writing out the data. For VLBA, this correction needs to be applied during calibration. `ACCOR` creates a solution (SN) table containing the amplitude errors of digital sampling, then smooths the table with `SNSMO`, and finally runs `CLCAL` to apply the solutions to the calibration table.

To perform phase corrections, one has to choose a reference antenna which preferably is present throughout the whole timerange of the observation. In addition, one needs a strong calibrator scan where all the antennas of the array are present. In the absence of such an antenna/scan two suitable scans are needed, and the reference antenna should be present in both of those scans. In this dataset Badary, Metsähovi and Svetloe covered the whole timerange of the observation, but they only contain noise in a significant part of the scans, probably due to unfavorable weather conditions. As a result of this, the reference antenna was selected to be Effelsberg, present in both the primary and secondary calibration scan. The secondary scan is needed to include the VLBA antennas in the calibration. After identifying these scans, I run `VLBAMPCL` to correct for instrumental phases and delays. Single-band delays and phase offsets between IFs arising from signal-propagation through the receiver and backend electronics are corrected by `FRING`, then the corrections are applied to a CL table by `CLCAL`.

`APCAL` uses the system temperature tables and gain curves loaded earlier by `ANTAB` to generate amplitude gain calibration information, stored in a solution or SN table. SN tables, similarly to the calibration tables contain antenna delay, rate, phase, and amplitude corrections solved for by various tasks. `APCAL` also uses weather data stored in the weather (WX) table to correct for atmospheric opacity. However, in this case the weather table was not added to the FITS-IDI at the correlator, so it had to be uploaded to `AIPS` from an external file. The correlated flux density, $V_{\rm ij}$, of a source is calculated as:

$$V_{\rm ij} = \sqrt{\frac{T_{\rm sys,i} T_{\rm sys,j}}{G_{\rm i} G_{\rm j}}} \times \rho_{\rm ij}, \tag{48}$$

where $T_{\rm sys,i}$ is a total on-source system temperature, and $G_{\rm i}$ is the antenna gain at a station, and $\rho_{\rm ij}$ is the correlation amplitude. The resulting SN table is applied to a CL table with `CLCAL`.

Even after removing instrumental phase offsets and single-band delays from each IF, the data will still contain residual frequency and time dependent phase variations, that are due to an imperfect correlator model and that we have to account for. `FRING` is used to determine the group delay (phase derivative with respect to frequency) and phase rate (phase derivative with respect to time) calibration, and apply

it to the visibility data given a model of the source. If the source model is not provided, `FRING` will assume a point source, whereas 3C 84 has an extended structure. As a result, the corrections `FRING` finds will not correct the data perfectly and, once we apply all the calibration, it will be necessary to do self-calibration to get the best images. `FRING` will also move the brightest spot of the source to the phase center, that is the coordinate position of the target used in the correlation. For the ground array, the signal-to-noise ratio (SNR) cutoff is at 5 σ. At this point we do not search for fringes to RadioAstron. After fringe-fitting and smoothing the output solution table with smoothing time of 1 hour, the delays and rates are applied to each integration period and spectral channel by `CLCAL`.

Since `FRING` only corrects for RR and LL, i.e., parallel hand delay difference between antennas, `RLDLY` has to be run to correct for delay offset between left and right polarization, by using observations of RL and LR correlations. After `RLDLY` there still remains an overall R-L phase offset, adding an overall rotation to the linear polarization position angle. Since polarization is not analyzed in this work, this does not affect our results.

After completing these steps, the calibrated data of the ground array can be written to a FITS (Flexible Image Transport System) file, and one can proceed to imaging.

7.2 Imaging with the ground array

Imaging of the ground array data was carried out in `Difmap` (Differential Mapping, Shepherd 1997). This interactive software offers a user-friendly interface for continuum VLBI data imaging and model fitting. In `Difmap` it is only possible to work on the data of one source at a time.

`Difmap` utilizes CLEAN, an iterative algorithm which deconvolves a sampling function (dirty beam) from an observed brightness distribution (dirty map) of a given radio source. The algorithm was introduced by Ian Högbom in 1974.

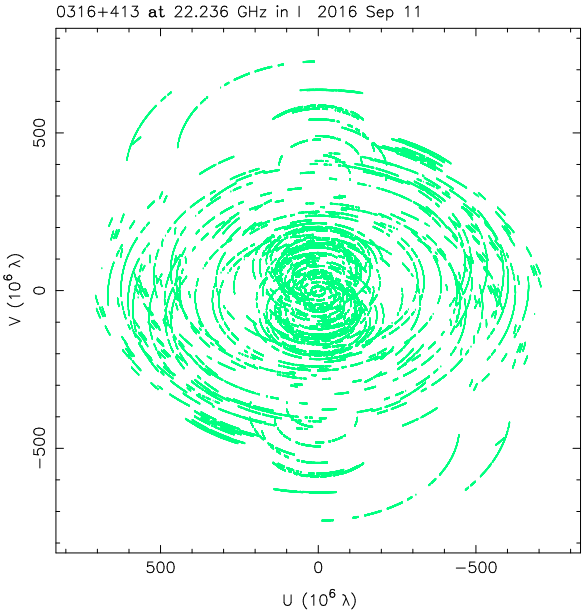

Figure 18: (u,v) coverage of the observations carried out on September 11-12, 2016 with the Global VLBI Network, not including RadioAstron.

Since VLBI arrays sample the (u,v) plane at discrete locations (see the (u,v) coverage of this observation in Fig. 18), the Fourier transform of the source intensity distribution is not completely known. The measured visibility data represents the true distribution in the(u,v)plane, denoted as V(u,v) multiplied by a sampling function, S(u,v). Based on the convolution theorem, the inverse Fourier transform of the sampled distribution (the dirty map: I_D, Fig. 19) is equal to the convolution of the inverse Fourier transform of the true source visibility distribution (the true image: I) and the inverse Fourier transform of the sampling function (the dirty beam, B_0):

$$I_D(l,m) = I(l,m) * B_0(l,m) \rightleftharpoons V(u,v) \times S(u,v) \tag{49}$$

where $*$ indicates convolution, and $\rightleftharpoons$ denotes the Fourier transform. In an ideal case, with a fully sampled (u,v) plane, the beam would be perfect, that is a delta function, whose Fourier transform is constant. However, since the (u,v) plane is not fully sampled, the beam consists of the main beam and sidelobes (i.e., it is a dirty beam), which the deconvolution algorithm attempts to remove from the image. In the undersampled regions, where the algorithm is guessing at the visibilities, modulations or stripes can occur, that can be eliminated by using a more accurate source model. CLEAN will eventually converge to a solution, although this may not be the correct one, since there is no unique solution to the convolution equation. There exists a solution if the beam is symmetric, the Fourier transform of the dirty beam is non-negative, and there are no spatial frequencies present in the dirty map which are not present in the dirty beam as well (Schwarz 1978). Once finished with deconvolving the image, we end up with the model of our source, or clean image, that is a collection of delta functions. Deconvolution is followed by a restore step, when the model is convolved with a Gaussian that matches the main lobe of the dirty beam, i.e. the clean or restoring beam. As a final step, the convolved image is added to the residual image.

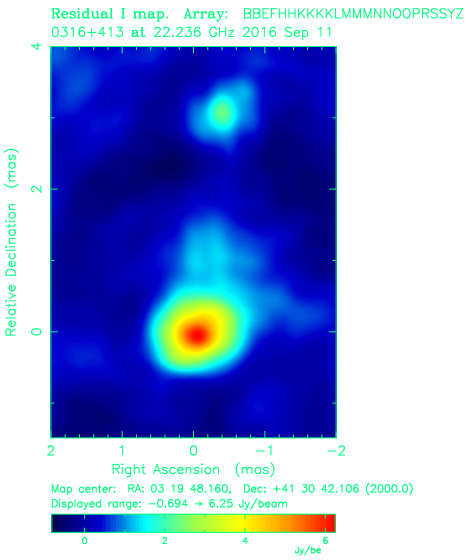

Figure 19: Convolution of the true brightness distribution with the interferometer beam or dirty map of the ground array data. The hotspot, C3 (image center), and the radio core is already visible on the image.

But how does clean operate? The algorithm looks for the brightest pixel (clean component) in a user specified region of the image, that should include all the real emission in the image (clean window). For Stokes I images ideally only positive components would be encountered. However noise, errors in previous clean iterations and calibration errors mean that eventually components with negative peak brightness will be found. Having found the peak pixel, clean subtracts a small, few percent fraction (loop gain) of the dirty beam from the dirty map at the location of that brightest pixel. This subtracted image is called the residual image. The search and subtraction loop is repeated until the sidelobes in the image are reduced to below the noise level. For extended sources, one can think of the emission as a collection of point sources (Taylor, Carilli & Perley, 1999).

For sufficiently bright radio sources clean can be supplemented with the self-calibration of the participating antennas. Even after the calibration procedure in `AIPS`, there still remains an unknown station-based phase-term, because each station has its own atmosphere and own frequency reference, a hydrogen maser. Self-calibration uses the model of the target source to achieve better calibration for the antenna-based complex gains, phases and amplitudes, as a function of time, by finding antenna gains, $g_{\rm i}$, which minimise the difference between the measured visibilities, $V_{\rm ij}$, and the model visibilities, $\hat{V}_{\rm ij}$:

$$\epsilon^2 = \sum |V_{\rm ij} - g_{\rm i} g_{\rm j}^* \hat{V}_{\rm ij}|^2. \tag{50}$$

For this, one needs an approximate image of the source, usually obtained by a deconvolution algorithm, like clean. Self-calibration can be performed when the number of baselines is higher than the number of antennas in the array. This creates a redundancy, because for N antennas in our array we measure N(N-1)/2 visibilities, and after the calibration only N amplitude gains and N-1 phase gains are needed to describe the complete calibration of the data (Taylor, Carilli & Perley, 1999). Another requirement for self-calibration is that the signal-to-noise ratio on each baseline be of the order of at least 5. Weak sources usually require a long solution interval, within which, the gains are assumed to be constant. This sometimes can degrade image quality. At 22 GHz one has to correct gains on the timescale of less than a minute.

In order to achieve the best results, the clean algorithm, that provides the trial image, and the self-calibration, that corrects the gains, are iterated several times until the solution converges and the image noise does not improve anymore. In an ideal situation the image noise should be close to the expected thermal noise level.

Before all this, the data has to be edited, so that stations with untrustworthy amplitudes, outlier points, mostly in the beginning of each scan, are flagged in `vplot`. Starting from the dirty map (Fig. 19), I first constructed a reliable source model by cleaning as much flux density as can be deduced from the short baselines in `radplot`, which is ∼28-29 Jy. After obtaining a good model, I performed the first amplitude calibration with `gscale true`, so allow the amplitude factors of the telescopes to float freely. This was necessary because of the poor amplitude calibrations of a few antennas, especially Badary. After determining the single amplitude correction factors for each antenna, I proceeded with iterating the clean algorithm and self-calibration. Phases were calibrated after each cleaning, but amplitude self-calibration was only performed when the root mean square (rms) residual value of the phase calibration stopped decreasing.

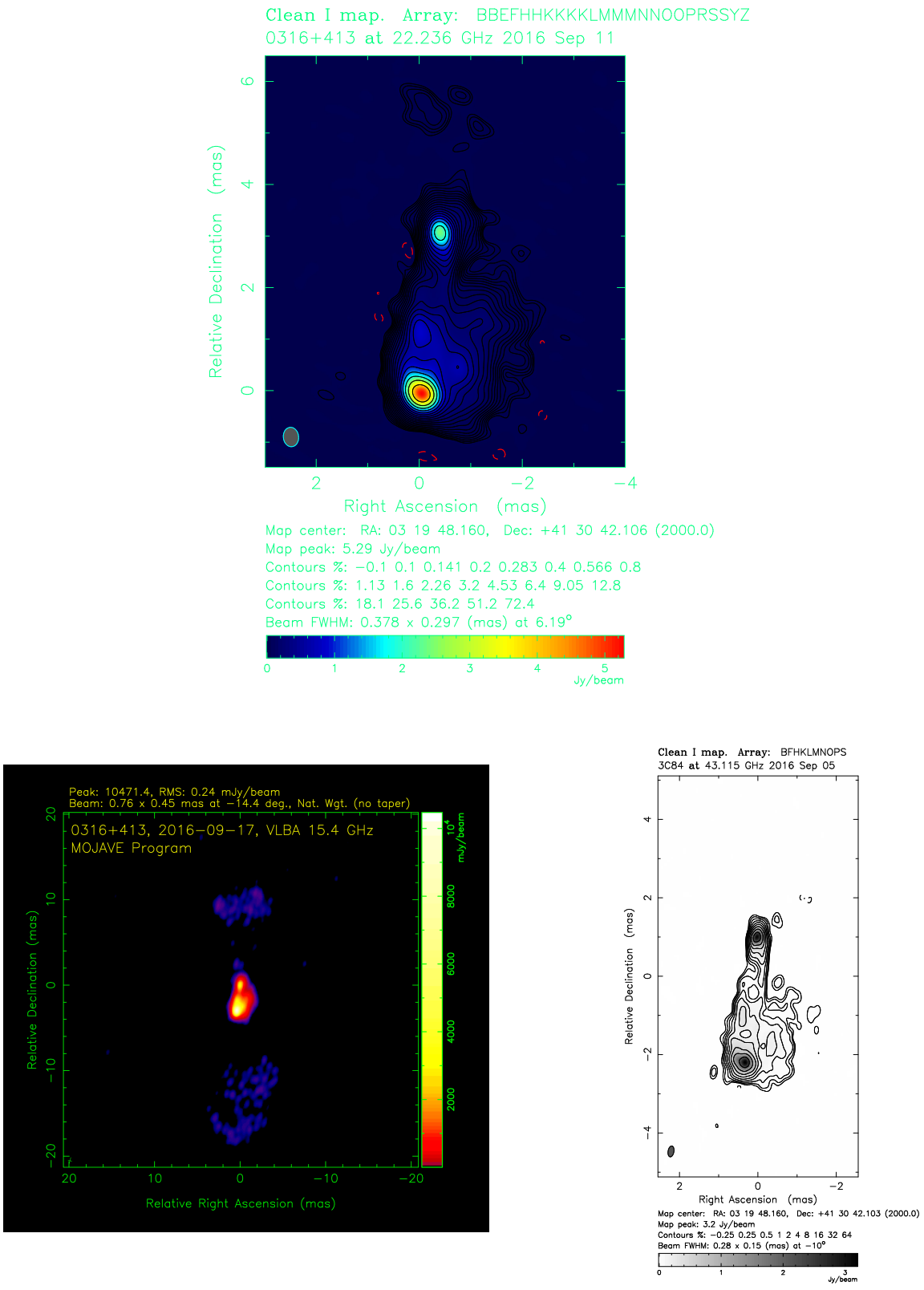

Figure 20: Images of 3C 84 in September 2016. The upper panel shows the 22 GHz image made with the Global VLBI Array, the lower left panel presents a 15 GHz VLBA image of the MOJAVE Group (Lister et al., 2018), and the lower right panel shows the 43 GHz image of the Boston University Blazar Group (Jorstad & Marscher, 2016, Jorstad et al., 2017). The central region of 3C 84 is similar in all three images, showing the usual emission features: C3, C2 and the core. At 22 and 43 GHz the lobes are too faint to be detected.

The final source model in the left panel of Fig. 20 contains 9065 clean components, and has the flux density of 28.1± 0.3 Jy. The beam size is 0.353 × 0.277 mas at PA=6.19°. The dynamic range – the ratio between the peak brightness and the rms noise – of the final image is The rms noise level was , with The weighting scheme was natural, with gridding weights scaled by visibility errors raised to the power -1. The structure of the source is similar to the one seen in previous observations. The brightest feature on the image is the hotspot at the end of the restarted jet, followed by the radio core. The more diffuse features involve C2 and the counterjet emission located northward from the core. The lobes located ∼20 mas from the center are too faint to be detected, but they are present at the 15 GHz VLBA image made by the MOJAVE Group (Lister et al., 2018) a few days apart from the observations presented in this work. The central source structure, on the other hand, is in agreement with the MOJAVE data.

The results obtained from the calibration of the ground array data enable us to proceed to the calibration of the Space Radio Telescope.

7.3 Calibration of RadioAstron

To involve RadioAstron in the calibration, it was necessary to start again from correcting the single-band delays and phase offsets between IFs, since the low signal-to-noise ratio data of the satellite was filtered out at this step. As mentioned earlier, `VLBAMPCL` runs `FRING` and `CLCAL` twice to manually calibrate the phase based on two scans that contain a common reference antenna. `VLBAMPCL` sets the SNR cutoff in `FRING` to 5 – a relatively high value –, and in `CLCAL` only calibrated data is applied to the CL table. In order to properly adjust parameters for the RadioAstron data, these steps have to be run separately. Unfortunately, I was only able to detect fringes to RadioAstron with a low signal-to-noise ratio, so I decided to pass through the RadioAstron data without performing instrumental phase calibration, and only calibrate the ground array data.

The calibration (fringe fitting and self–calibration) was first performed on the ground array data so later, during the second round of fringe search we would be able to maximize the sensitivity when looking for signal on the space–Earth baselines. This is necessary because of the exceptionally long baselines to RadioAstron, and the small diameter of the antenna, as well as the complex source structure. This method described in Kogan (1996) enables us to use longer integration time to further improve sensitivity of the fringe search. Integration time can be as long as $\gtrsim$10 min instead of 1 min (in this case, it was $\sim$ 15 min), since atmospheric phase fluctuations are removed by self–calibration for the ground array, and for the space–borne telescope we do not need to worry about atmospheric effects.

The earlier, coarse fringe search performed at the correlator with the VLBI processing software, `PIMA` (Petrov et al., 2011) revealed fringes between the Effelsberg 100 meter telescope and RadioAstron in four 15–minute scans, between 23:15–00:15 UT, so these scans were the first target for fringe fitting. The signal was detected in all four scans, albeit sometimes with a low signal-to-noise ratio. Robust detections were made in two scans: in one scan, averaging bands and polarizations led to a detection with SNR=3.3, and in the next scan, fringes were found with SNR=4.1 for polarization 1 at zero rate. In the remaining scans the low SNR detections are justified by the `PIMA` results and the smooth change in rates and delays, and are summarized in Table 5. The RadioAstron scans not containing signal between the satellite and the ground array telescopes were flagged in `Difmap` before imaging.

Scan	Time (UT)	Phase (°)	Rate (mHz)	Delay (ns)
58	0/23:15:00 – 0/23:30:00	54.4	-1.16	9.77
59	0/23:30:30 – 0/23:45:00	-65.9	-0.24	0.0
60	0/23:45:30 – 0/23:59:59	30.5	1.47	-3.91
61	1/00:00:30 – 1/00:15:00	30	11.11	-15.62

Table 5: Fringe detections between 23:15–00:16 UT. The fringes are centered at zero, and rates and delays change smoothly over time.

After these results are applied to the previous CL table using `CLCAL`, `RLDLY` is run to correct for delay offset between the two polarizations. Finally, the calibrated data of 3C 84 is written to a FITS file for imaging.

7.4 Imaging with RadioAstron

Imaging of the RadioAstron data is done in a similar fashion as previously with the ground array – using the `clean` algorithm and `selfcal` in `Difmap` – but with small modifications due to the involvement of the Space Radio Telescope.

After editing the data, imaging started from the dirty map shown in Fig. 22. Throughout imaging I used super-uniform weighting – `uvw 5,-1` – to down-weight shorter baselines, and give baselines to RadioAstron more significance, hence improving the angular resolution of the final image.

During phase self-calibration, I first fixed the weights for all antennas, then calibrated phases with 1 minute solution interval. In the second round of phase calibration, I only calibrated the ground array data with 10 second solution interval. This sequence was required because self–calibrating the low signal–to–noise ratio data of RadioAston, especially when the satellite is located at the end of long and narrow baseline–triangles, would create additional flux density from the noise, and could lead to false detections when fake source components are created (Martí–Vidal & Marcaide, 2008). In the case of amplitude self-calibration, after obtaining normalization factors with `gscale` only the ground array needs to be calibrated, since RadioAstron observes outside of the Earth's atmosphere.

The first amplitude calibration was performed after obtaining a good model of the source with $\sim$ 28 Jy flux density. However, since the involvement of the incredibly long baselines of RadioAstron and the super-uniform weighting, the surface brightness sensitivity of the array decreased, and after amplitude calibration flux density dropped to $\sim$ 26 Jy.

The final model is shown in Fig. 23. It contains 13660 clean components with the total flux density of 26.2$\pm$0.3 Jy. The beam is quite elongated because of the extremely long space baselines. Its FWHM is 0.217$\times$ 0.0752 mas at PA=-49.6°. The rms noise level is 0.91 mJy/beam. The image shows the well-known structure of the central region of the galaxy, consisting of the radio core, the C2 and C3 features. Compared to the image in the previous stage of calibration, here the parsec-scale jet and counter–jet are resolved, indicating a limb-brightened structure. Since the shorter baselines are down-weighted, the extended structure of 3C 84, the lobes are not detected.

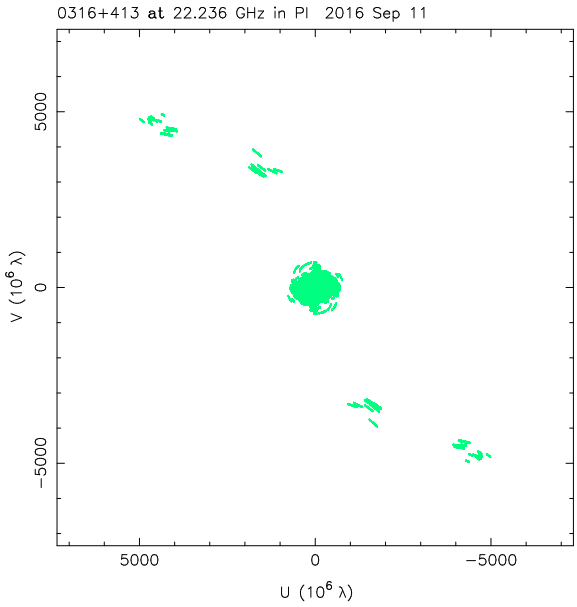

Figure 21: (u,v) coverage of the observations carried out on September 11-12, 2016 with the Global VLBI Network supplemented by the Space Radio Telescope. The center of the (u,v) plane is traced by the ground array telescopes, whereas RadioAstron baselines extend up to $5{\times}10^9$ λ.

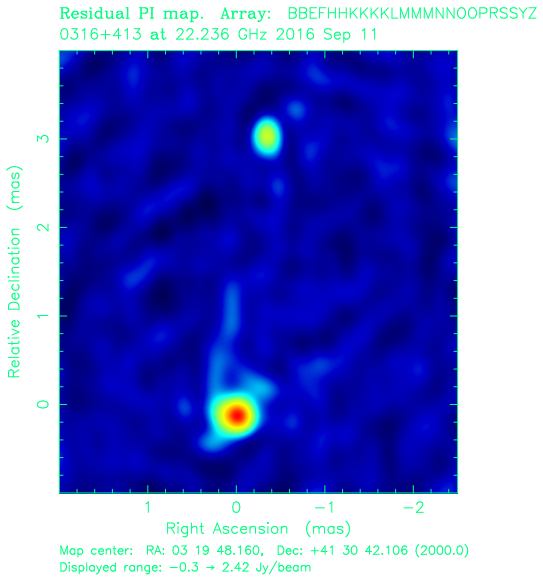

Figure 22: dirty map of the observation. Similarly to the dirty map of the ground array imaging, the image shows the C3 hotspot (image center) and the radio core.

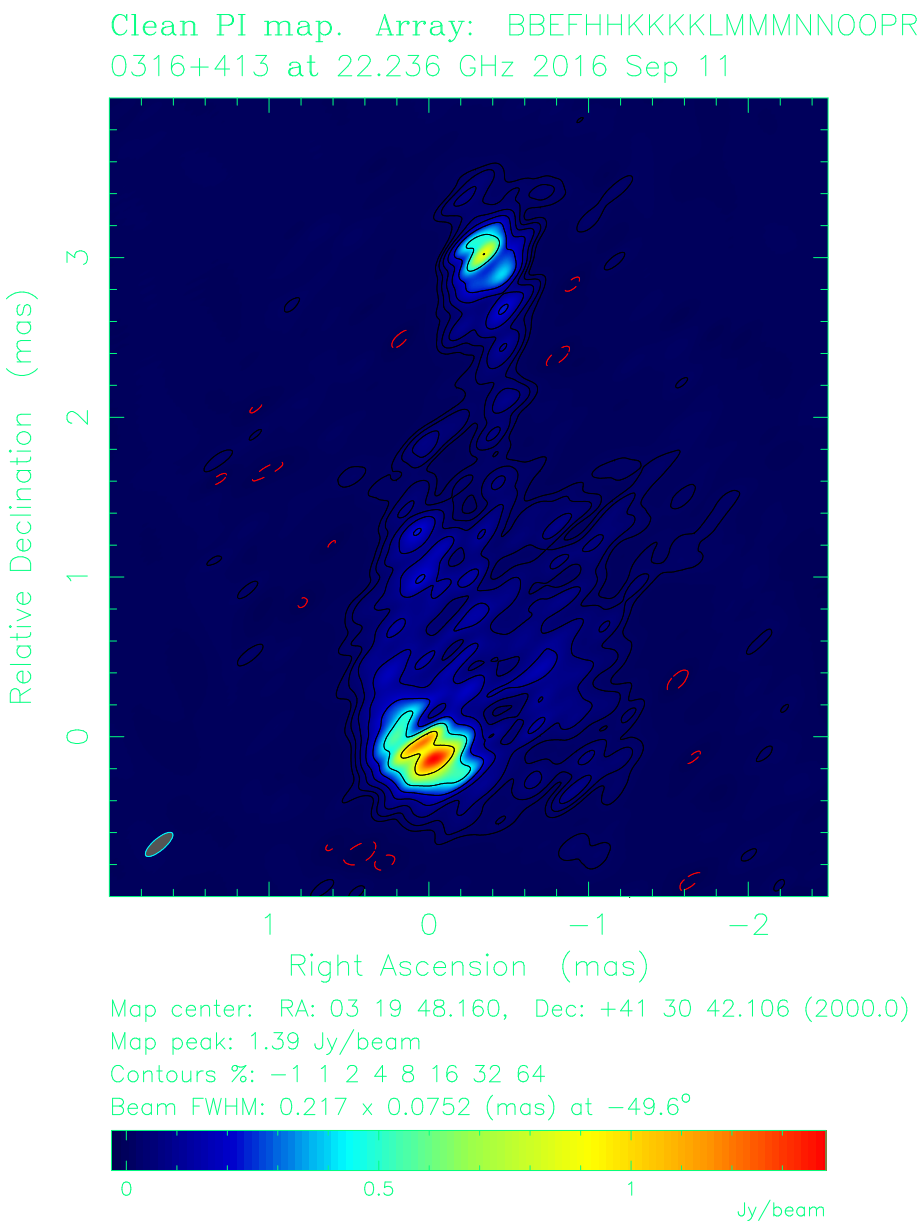

Figure 23: Image of the central parsec region of 3C 84 from the 22 GHz observations on September 11, 2016, obtained by the Global VLBI Network, supplemented by the Space Radio Telescope, RadioAstron. Contours are at 1.39 Jy/beam × (-1, 1, 2, 4, 8, 16, 32, 64), where 1.39 Jy/beam is the peak intensity, and the rms noise level is 0.91 mJy/beam. The restoring beam is highly elliptical, 0.217×0.0752 mas at -49.6°. The total flux density is 26.2±0.3 Jy. The increased angular resolution due to the involvement of RadioAstron lead to the detection of the edge–brightened jet and counter–jet, and a double–peaked structure in the hotpot at the jet head.

8 Results

8.1 Evolution of the jet

The images obtained by Giovannini et al. (2018) and this work (Fig. 25) show the central parsec region of 3C 84. The structure has changed significantly in the three years separating the two observations. Both images show the same emission features – the radio core, C2, C3, the parsec–scale jet and the counter–jet – but several differences can be noticed. The hotpot or C3 has moved from the center of the feature to its edge, and the jet itself appears a little longer and notably straighter than before. Limb-brightening is also confirmed not only in the parsec-scale jet, but in the counter–jet as well.

Images of the jet-core region (Fig. 24) restored with nearly circular beams show the limb-brightened structure of the jets starting from the radio core. One can also notice a big change in the jet orientation between the two epochs, which was measured by obtaining slices along the jet spine near the core. The measured change was 20°±1.0.

The hotspot's position has advanced by ∼ 1 mas further from the core during these three years. To determine the change in distance, and the yearly advance of the jet, I fitted Gaussian components on the radio core and the hotspot in `Difmap`, and determined the distance between the center of the components. I performed a similar analysis for the image from the paper of Giovannini et al. (2018). Here, I fitted the Gaussian components with the `JMFIT` task in `AIPS` to determine their distance. This time I fitted three components, one on the radio core, and two components on the two brightest features in the hotspot (see Figure 25). Depending on which component is taken into account, the jet advances with the apparent velocity of $\beta_{\rm C3}$ = 0.315±0.006 mas/yr ∼ 2.91c±0.04 or by $\beta_{\rm C3,dim}$ = 0.24±0.01 mas/yr ∼ 2.2c±0.3 for the brighter and dimmer spots, respectively. The projected speed of these features is $\beta_{\rm C3}$ = 0.945c± 0.002 and $\beta_{\rm C3,dim}$=0.92c± 0.01.

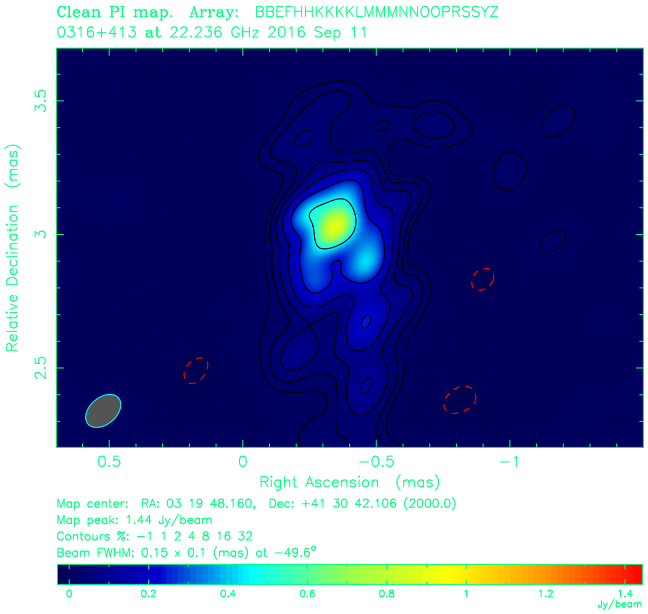

Figure 24: The core of 3C 84 restored with a 0.15×0.1 mas beam. The edge-brightened jet is visible all the way to the radio core, as in Giovannini et al. (2018). Contours are at 1.44 Jy/beam × (-1, 1, 2, 4, 8, 16, 32, 64).

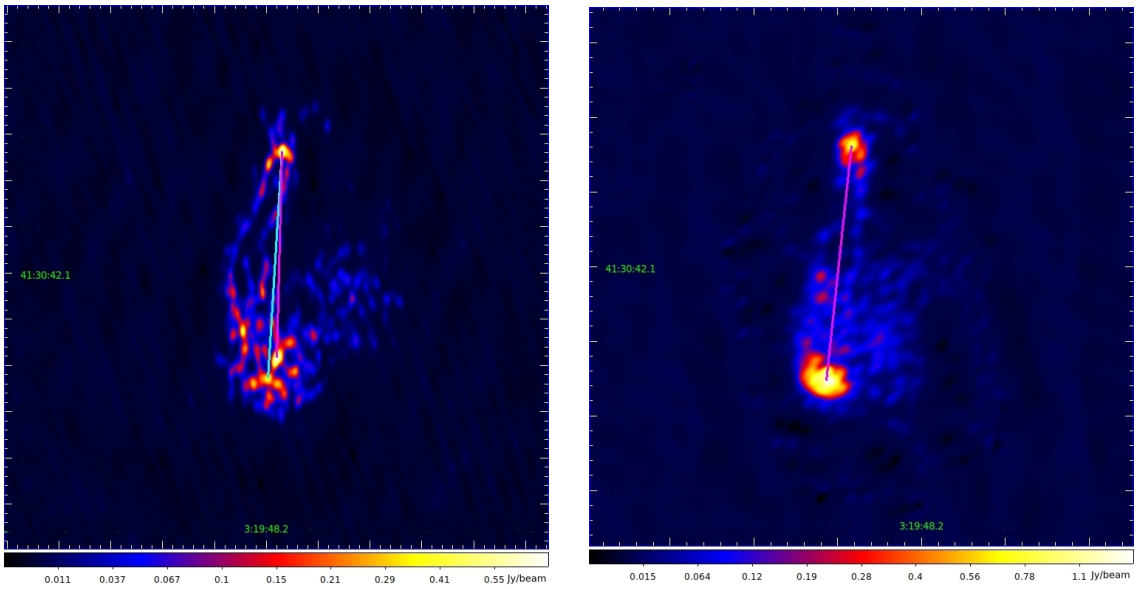

Figure 25: The central parsec region of 3C 84. Panel a, shows the image from Giovannini et al. (2018) obtained from the observations on September 21, 2013, and Panel b, shows the image from this work, from data recorded on September 11, 2016. The structure of the source has slightly changed in the three years between the observations. The cyan and magenta lines show the distance between the center of the fitted Gaussian components at the radio core and the hotspot.

8.2 Brightness temperature measurement

Based on the total flux density, S_ν and size of the `modelfit` components fitted on the final self-calibrated data in `Difmap`, the $T_{\rm b,obs}$ brightness temperature of the emission features can be estimated. Brightness temperature is defined as the temperature needed for a blackbody, i.e. thermal radiator to produce the same specific intensity as the observed, usually non-thermal source. It is given as $T_{\rm b,obs} = I_\nu c^2/2k_{\rm B}\nu$, where ν, $k_{\rm B}$, and c denotes the observing frequency, the Boltzmann constant, and the speed of light, but for an elliptical Gaussian component it can be obtained from the following equation:

$$T_{\rm b,obs}[{\rm K}] = 1.22 \times 10^{12} \Big(\frac{S_\nu}{\rm Jy}\Big)\Big(\frac{\nu}{\rm GHz}\Big)^{-2}\Big(\frac{d_{\rm maj} \times d_{\rm min}}{\rm mas^2}\Big)^{-1}(1+z), \tag{51}$$

where $d_{\rm maj}$ and $d_{\rm min}$ denote the FWHM of the major and minor axis of the fitted Gaussian component, and z is the redshift of the object, and the $(1+z)$ factor takes into account the effect of the cosmological redshift. Since 3C 84 has a rather complicated structure, the source was described by 9 model components with the total flux density of 25.8±0.1 Jy. The model parameters and the obtained brightness temperatures are listed in Table 6, and the fitted model is shown in Fig 26.

Since the original clean image shows a double-peaked structure in C3, I modeled the hotspot with an other method as well. Starting from the clean image, I removed clean components in the area of approximately 10 beam sizes centered at C3, and fitted two Gaussian components there (see Figure 27). Their parameters and the obtained brightness temperatures are shown in Table 7. The total flux density of the two components is ∼1 Jy higher than the flux density of the previously fitted single component's.

From the Gaussian components fitted on the image plane of the clean model in Giovannini et al. (2018), I calculated the brightness temperatures for the radio core and the brightest spot in C3. The obtained model parameters are summarized in Table 8. Comparing these temperatures to the ones measured in this work, it can be seen that the brightness temperature of these features have decreased significantly, by ∼70% in the core, and by ∼50% in the hotspot. In the case of the jet, this is explained by the expansion of the feature, whereas in the case of the core it can be connected to the flux variations during the ejection of a new radio component (Savolainen et al. 2002).

Intrinsic brightness temperature, $T_{\rm b,int}$ of the radio core and the hotpot is calculated as:

$$T_{\rm b,int} = \frac{T_{\rm b,obs(1+z)}}{\delta}, \tag{52}$$

where $\delta = (1-\beta^2)^{-1/2}/(1-\beta\cos\theta)$ is the Doppler factor. β is the flow velocity in the units of c, and θ is the jet inclination angle. β is assumed to be the measured velocity of C3, $\beta_{\rm C3} = 0.945$ with jet inclination of θ=18°, which gives the Doppler factor, δ=3.23±0.03. For the 2013 observations, the same δ is adopted. The intrinsic temperatures were calculated based on the entries in Table 6 and Table 8. For the core, $T_{\rm core,2016} = 3.8\pm0.1 \times 10^{10}$ K and $T_{\rm core,2013} = 1.3\pm0.07 \times 10^{11}$ K, and for the hotpot $T_{\rm C3,2016} = 7.3\pm0.07 \times 10^{10}$ K and $T_{\rm C3,2013} = 1.3\pm0.01 \times 10^{11}$ K.

Component	S_ν (Jy)	Stdev (mJy)	$d_{\rm maj}$ (mas)	Stdev (10^{-7} arcsec)	$d_{\rm min}$ (mas)	Stdev (10^{-7} arcsec)	$T_{\rm b,obs}$ (K)
Core	2.457	1.5	0.2537	1	0.1961	1.5	$1.2\pm0.04 \times 10^{11}$
C3	7.468	2.8	0.336	0.61	0.2388	0.96	$2.3\pm0.04 \times 10^{11}$
Core extended	2.277	1.6	0.8362	3.1	0.3102	8.4	$2.2\pm0.001 \times 10^{10}$
C3a	2.117	2.8	0.5035	2.2	0.1952	5.6	$5.4\pm0.02 \times 10^{10}$
C3b	4.093	7.5	1.539	7.8	0.5841	21	$1.1\pm0.05 \times 10^{10}$
C3c	0.916	1.7	0.5613	4.3	0.1576	15	$2.6\pm0.004 \times 10^{10}$
C3d	2.579	5.1	1.267	7.2	0.4782	19	$1.1\pm0.003 \times 10^{10}$
C2a	1.534	3.6	0.7061	5.6	0.3603	11	$1.5\pm0.02 \times 10^{10}$
C2b	2.374	6.9	1.245	17	0.8729	27	$5.5\pm0.0 \times 10^{9}$

Table 6: Model parameters and the obtained brightness temperatures. The corresponding Gaussian components are displayed in Fig. 26.

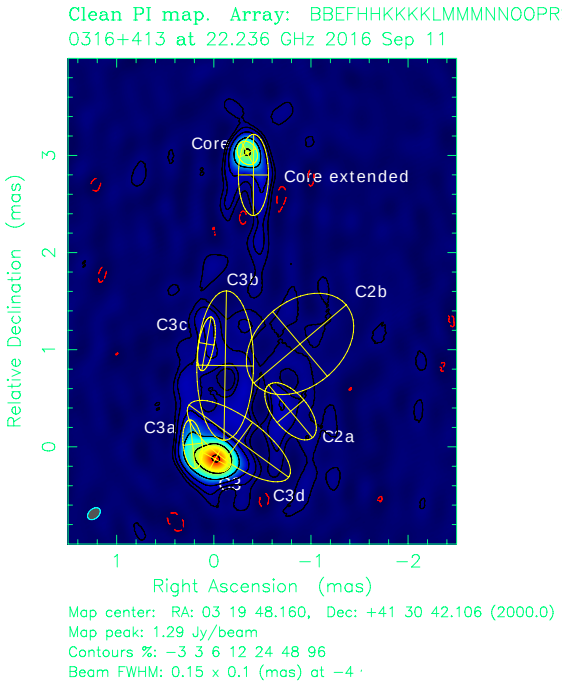

Figure 26: Model obtained by fitting Gaussian components on the self-calibrated data. The model contains 9 components with the total flux density of 25.8 ± 0.1 Jy. Contours are at 1.29 Jy/beam × (-3, 3, 6, 12, 24, 48, 96) at PA -49.6 °.

Component	S_ν (Jy)	Stdev (mJy)	$d_{\rm maj}$ (mas)	Stdev (10^{-7} arcsec)	$d_{\rm min}$ (mas)	Stdev (10^{-7} arcsec)	$T_{\rm b,obs}$ (K)
Component 1	4.454	4.5	0.2067	0.94	0.1947	1.3	$2.7\pm0.01 \times 10^{11}$
Component 2	4.021	4.5	0.3287	0.92	0.2156	1.5	$1.4\pm0.01 \times 10^{11}$

Table 7: Model parameters and the obtained brightness temperatures for the C3 component. The corresponding Gaussian components are displayed in Fig. 27.

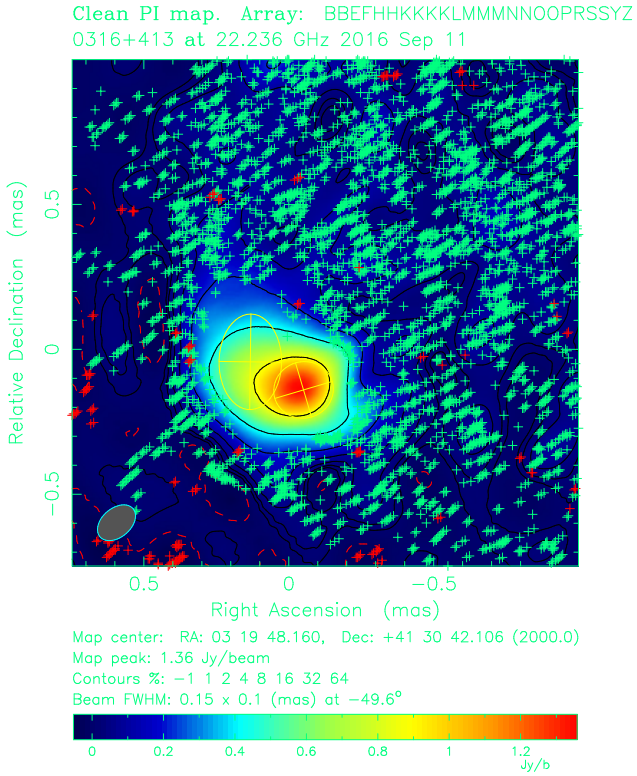

Figure 27: Gaussian model components fitted on the hotspot. The green and red crosses represent the clean components. Contours are at 1.29 Jy/beam × (-3, 3, 6, 12, 24, 48, 96) at PA -49.6 °, and the model contains 26.2±0.3 flux density.

Component	S_ν (Jy)	Stdev (mJy)	$d_{\rm maj}$ (mas)	Stdev (10^{-7} arcsec)	$d_{\rm min}$ (mas)	Stdev (10^{-7} arcsec)	$T_{\rm b,obs}$ (K)
C3	1.286	3.2	0.1486	2.4	0.05	8.3	$4.3\pm0.05 \times 10^{11}$
Core	0.903	2.7	0.1069	1.89	0.05	0.89	$4.2\pm0.04 \times 10^{11}$

Table 8: Model parameters and the obtained brightness temperatures for the core and the C3 component in the image plane of the clean image in Giovannini et al. (2018). Brightness temperatures are ∼3 times higher than measured in this work.

8.3 Collimation profile measurement

The collimation profile, $W(z)$ describes the jet width as a function of the distance from the core along the jet, z. It provides information on the formation and the collimation of the jet. Detailed collimation profile measurements are available for several nearby AGN – M87: Asada & Nakamura (2012), Cygnus A: Boccardi et al. (2016) , Centaurus A: Janssen et al. (2021), NGC 4261 Nakahara et al. (2018), NGC 6251: Tseng et al. (2016), etc.

Following the analysis carried out by Giovannini et al. (2018), I calculated collimation profiles for three different cases of black hole mass and jet inclination. The broadband SED reproduced with the spine-layer model of Tavecchio & Ghisellini (2014) suggests an inclination smaller than 20°, so Giovannini et al. (2018) adopted an inclination of 18°for their analysis. The corresponding black hole mass assumption was $2\times\ 10^9$ $M_\odot$. On the other hand, a large inclination of 45°is also realistic based jet–to–counter–jet ratio analysis. Based on near-IR integral field spectroscopic observations, Scharwächter et al. (2013) determined the black hole mass as 8×10^8 $M_\odot$, with lower limit of 5×10^8 $M_\odot$ for a disk inclination of 45°±10°.

For the analysis, I used the image with 0.00495 mas pixel size restored with a 0.15×0.1 mas beam (PA=-49.6°). First, I obtained slices perpendicular to the jet direction with the `AIPS` task `SLICE`. The slices are perpendicular to the straight line connecting the peak brightness position of the core and the hotspot. The first slice is located at 0.01 mas distance from the core, corresponding to ∼1190 r_g (M_{BH}=2 × 10^9 $M_\odot$, θ=18°). The first two slices measure the width of the swinging jet base, and the following slices are obtained at every 0.15 mas in the length of the jet. Out of the twelve slices made, eleven showed the double-peaked structure typical of edge-brightening. The one slice where limb-brightening was visible only on one side of the slice, was omitted from the analysis. The slices and an example of a slice profile are shown in Figure 28.

In the ΛCDM cosmology (H_0 = 70.7 km s^{-1} Mpc^{-1}, Ω_M= 0.27, Ω_Λ = 0.73) the angular scale at redshift z = 0.0176 is 0.354 mas/pc (CosmoCalc: Wright, 2006). I calculated the $r_g = GM_{BH}/c^2$ gravitational radii for the three black hole masses, as well as the conversion factor between gravitational radius and mas (see Table 9).

M_{BH} ($M_\odot$)	Jet inclination (°)	r_g (pc)	r_g (mas)	1 mas (r_g)
$2\times\ 10^9$	18	9.5738×10^{-5}	1.7033×10^{-4}	3.6991×10^3
$8\times\ 10^8$	45	3.8295×10^{-5}	1.0818×10^{-4}	9.2439×10^3
$5\times\ 10^8$	45	2.3925×10^{-5}	6.7585×10^{-5}	1.47962×10^4

Table 9: Scaling parameters for the three different black hole masses assumed for 3C 84.

The slice profiles were fitted with two 1-D Gaussian components with the `AIPS` task `SLFIT`. Then the jet width profile was fitted as $r \propto A z_{obs}^a$, where r is the jet width, z_{obs} is the de–projected distance from the core, given as $z_{obs} = z/\sin\theta$, and A and a are constants. The jet width profile fit (Fig. 29) resulted in a less cylindrical profile than seen previously in Giovannini et al. (2018) –a = 0.17 – and Nagai et al. (2014) – a = 0.25±0.03 – with a= 0.31±0.002. The errors for the jet width were estimated from the fit parameters, whereas the error for the distance measurement from the core was taken to be 2 pixels.

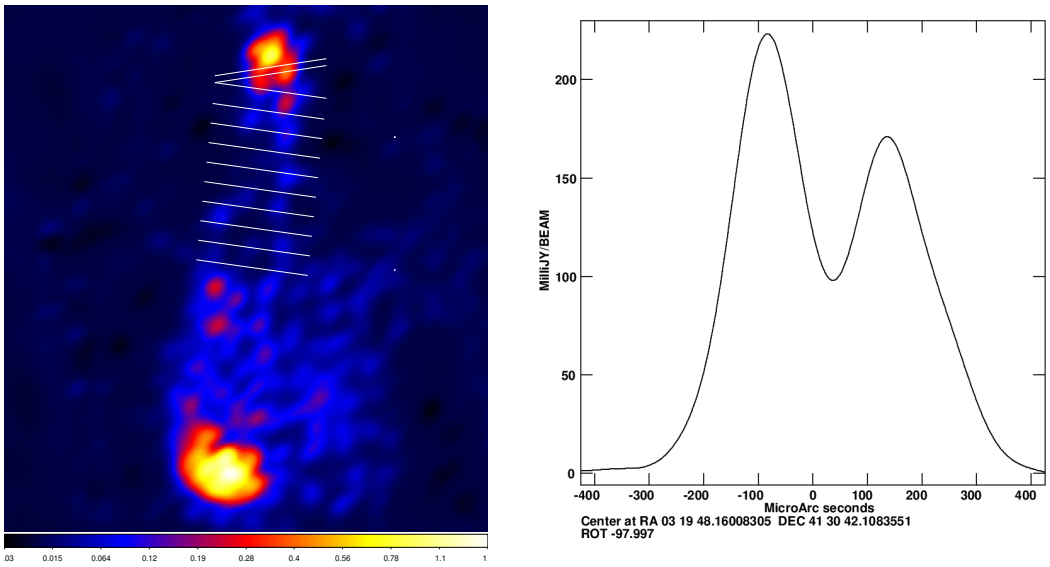

Figure 28: The left panel shows slices made at ∼0.15 mas starting from 0.01 mas from the core, extending to 1.6 mas. Out of the twelve slices obtained, ten jet width measurements were carried out in AIPS. A slice profile with a double-peaked structure indicating edge-brightening is shown in the right panel.

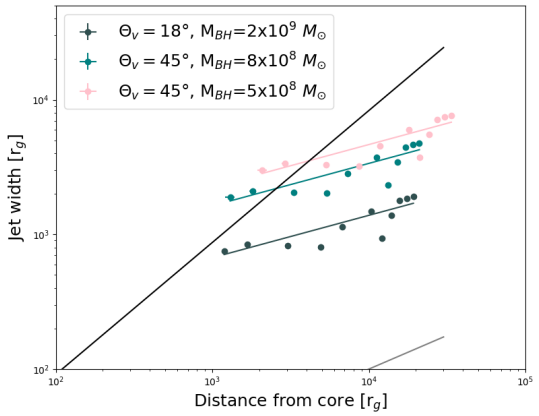

Figure 29: Jet width profile of 3C 84. The dots represent the jet width measurements from the 22 GHz RadioAstron data, and lines are the corresponding collimation profiles. The profiles describe a cylindrical streamlines with $r \propto z_{\rm obs}^{0.31\pm0.002}$. The black and gray lines represent quasi-conical ($r \propto z_{\rm obs}^{0.98}$) and parabolic ($r \propto z_{\rm obs}^{0.5}$) profiles, respectively.

9 Discussion

The 22 GHz RadioAstron observation presented in this work allows us to investigate the evolution of the restarted jet that first appeared in 2003 (Suzuki et al. 2012). The results were compared with previous observations carried out with RadioAstron (Giovannini et al. 2018). The most noticeable changes and results, such as the flip of the hotpot's position, the lengthening of the jet and the edge-brightened structure were briefly mentioned before, but let's explain them in more detail.

The new image confirms the existence of the limb-brightened jet, as well as the limb-brightened counter-jet that were visible in 2013. This confirmation is important, because although the detection edge-brightened jet was robust, the same was not true for the limb-brightened counter–jet, since the (u,v) coverage on the space baselines was very one-dimensional in 2013. This property of the space baselines could have created image artifacts that were noted as detection. Although the same can be said about the 2016 observations, the different orientation of the space–baselines in the (u,v) plane, which are nearly perpendicular to that in 2013, result in the same structures, making the detections reliable. In the 2016 image, however, one of the jet limbs is not visible in the full length of the parsec–scale jet. The jet also appears straight on the 2016 image, that can be explained based on the paper of Kellermann et al. (2004), who has shown that new jet components tend to follow the already existing flow direction rather than continue on ballistic trajectories originating from the core.

Comparing the images of the jet-core region (Fig. 24) restored with nearly circular beams, the limb-brightened structure in the jet and counter-jet are visible at both epochs. However, the jet orientation at the base has changed by $20°\pm1.0$ between the two observation, meaning a $\sim$7°change per year. Jet precession has been suggested in previous papers of Dominik et al. (2021) and Britzen et al. (2019) with the period of 25-30, and 40 years, based on VLBI maps, respectively. Britzen et al. (2019) suggests two explanations for the jet precession. There may be a binary black hole at the center of the NGC 1275 galaxy based on the observed double spiral galaxy structure of the source. This would cause a precession of the accretion disc (Katz et al. 1997). On the other hand, a disc instability warping a disk can also lead to a precessing jet (Pringle 1997). In the 1990s, the jet base was pointing towards the C2 feature, then its direction changed, and during the launching of the parsec–scale jet it moved towards west (Suzuki et al., 2012). In the 2016 observations it moved towards the East again. This suggests that the jet precesses with a $\sim 30 - 40$ year period.

Between 2013 and 2016, the hotspot's position has advanced by $\sim$ 1 mas. The speeds were calculated for the brightest and a dimmer emission feature of the hotpot. The projected speed of these features is $\beta_{\rm C3} = 0.945c\pm$ 0.002 and $\beta_{\rm C3,dim}$=$0.92c\pm$ 0.01. These values are significantly higher than the ones calculated in Nagai et al. (2010) – $\beta = 0.23 \pm 0.01$ c between 2007 and 2009 – but they are consistent with the velocity of $0.943c$ measured in Giovannini et al. (2018), meaning that the jet has been accelerating since its appearance in 2003.

Another notable feature is that the hotspot has moved from the center of the jet head to the leading edge. Kino et al. (2018) date the flip in the hotspot's position to fall between August and September, 2015. This flip was predicted in the AGN feedback simulations of Wagner & Bicknell (2011), who proposed that the flip is caused by the interaction between the jet and the cold, dense clumps of the nonuniform

surrounding medium. An alternative explanation for the flip can be the precession of the jet. However, the enhanced polarized emission reported by Nagai et al. (2017), as well as the suggests the former. After the flip in September, the peak position of C3 – that coincides with the reverse shock at the jet head – has decelerated, and wobbled for a few months, then started to accelerate to velocities nearing the speed of light. The peak intensity has also increased by a factor of 4 during the observations, coinciding with the restarted propagation. The estimated number density of the clump falls between 4×10^3 cm$^{-3} < n_{\rm cl} < 2 \times 10^5$ cm^{-3}, placing it in the narrow–line region of the AGN or in a denser part of an intergalactic molecular cloud.

Brightness temperature measurements show a 70%, and 50% drop between 2013 and 2016 in the core and the hotspot, respectively. The former can indicate the ejection of a new radio component (Savolainen et al. 2002), and the latter can be explained by the expanding jet head, which advanced ∼1 mas in three years. The intrinsic brightness temperature of the core and the hotpots in 2016 are $T_{\rm core,2016}$ = 3.8±0.1 × 10^{10} K and $T_{\rm C3,2016}$ = 7.3±0.07 × 10^{10}. These values do not exceed the ≈10^12 K limit of the inverse Compton catastrophe (Kellerman & Pauliny-Toth, 1969). Inverse Compton catastrophe is a rapid Compton cooling that arises when photon energy density exceeds the magnetic energy density, which happens when the intrinsic brightness temperature of the source exceeds ≈10^{12} K. Since $T_{\rm core,2016}$ and $T_{\rm C3,2016}$ are below this limit, both the core and C3 are in a steady state,and their the incoherent synchrotron emission originates from electrons with a power-law energy distribution. However, $T_{\rm core,2016}$ is below the equipartition brightness temperature (Readhead, 1994), $T_{\rm eq} \sim 5 \times 10^{10}$ K, and $T_{\rm C3,2016}$ does not exceed this value significantly either. This suggests that in the core magnetic energy dominates over particle energy, and in the hotspot particle energy gives a a bigger contribution to the total energy.

Jet width measurements were obtained between de–projected distance 1400 and 19000 $r_{\rm g}$. Similarly to the results in Giovannini et al. (2018), the calculated jet width profiles are significantly wider than the parabolic Blandford–Znajek type profile with $r \propto z_{\rm obs}^{0.5}$, but here they cross the line of the quasi-conical profile with $r \propto z_{\rm obs}^{0.98}$. 2016 observations record a less cylindrical profile than it was measured in 2013, with $r \propto z_{\rm obs}^{0.31\pm0.002}$. This is still in contrast with the previously calculated parabolic ones of M87 (Nakamura et al., 2018) –$r \propto z_{\rm obs}^{0.56\pm0.01}$ measured between 200 and 4×10^4 $r_{\rm g}$– and Cygnus A (Boccardi et al., 2016) –$r \propto z_{\rm obs}^{0.55\pm0.07}$ between 500 and 10^4 $r_{\rm g}$.

The closest point to the apex was located at $z_{\rm obs} \approx 1200$ $r_{\rm g}$ with $r \approx 750$ $r_{\rm g}$. This measurement does not fall as close to the core as the 2013 one, so it cannot confirm the wide jet base at 350 $r_{\rm g}$. The new results support the conclusion of the previous paper that the jet may be launched from the accretion disk, or it requires a quick lateral expansion on a scale of 10^3 $r_{\rm g}$ in the case it is ergosphere–launched.

The external pressure and density gradients are given as $p_{\rm ext} \propto z^{-4a} = z^{-k+1} = z^{-1.24}$ and $\rho_{\rm ext} \propto z^{1-4a} = z^{-k} = z^{-0.24}$. The decreasing density and pressure profiles of the external medium and the less cylindrical profile obtained from the 2016 observations suggests that the jet is surrounded by an external cocoon, formed by the interaction between the jet and the ambient medium (see first numerical simulations, Rayburn 1977). As the jet propagates through the cocoon material, the pressure of the latter decreases, and cannot collimate the jet as efficiently as it did closer to the core, hence the widening of the cylindrical shape.

10 Conclusions

This thesis work has presented 22 GHz observations carried out with the Global VLBI Network together with the late Space Radio Telescope, RadioAstron. Based on the analysis of the final image, the following conclusions can be drawn on the evolution of the parsec-scale jet:

1. The morphology of the central parsec region of 3C 84 has not changed in several aspects between 2013 and 2016:
   - The edge–brightened structure is confirmed both in the parsec–scale jet and the counter–jet.
   - The jet base has moved by $\sim$20°between the observations, which may be due to the precession suggested by Dominik et al. (2021) and Britzen et al. (2019). The jet pointed towards C2 in the 1990s, then moved westwards when the jet appeared, and now it is moving towards its original position. This suggests a precession period of $\gtrsim$30 years, in agreement with the above mention studies.
   - The position of the hotspot has moved to the jet head from the center of the feature, (also observed by Kino et al. 2018), in agreement with numerical simulations of AGN jets propagating through non–uniform ambient medium, performed by Wagner & Bicknell (2011).
   - The jet has advanced by $\sim$1 mas, indicating a propagation velocity of $\beta_{\rm C3}{\approx}0.945c$, so it has accelerated slightly since 2013.
2. Brightness temperature decrease in the core and the hotspot indicate an ejection of a new component, and an expanding source, respectively. Intrinsic brightness temperature of the core falls below the equipartiton brightness temperature ($\approx5{\times}10^{10}$ K), here magnetic energy dominates. The hotspot's intrinsic brightness temperature is slightly above this, so here particle energy dominates.
3. The jet width profile measurements between 1400 and 19000 $r_{\rm g}$ capture a different, less cylindrical profile of $r \propto z_{\rm obs}^{0.31}$ compared to the quasi-cylindrical one presented in Giovannini et al. (2018) with $r \propto z_{\rm obs}^{0.17}$. The most likely explanation is that there is an external cocoon surrounding the source, whose pressure decreases as the jet propagates through its material, and cannot confine it further from the core.
4. The closest jet width measurement is take at the de–projected distance of 1200 $r_{\rm g}$, so it cannot confirm the wide jet base calculated in Giovannini et al. (2018) at 350 $r_{\rm g}$. Here, the jet width is 750 $r_{\rm g}$ at the closest point to the apex, which does not contradict the conclusion that the jet may be launched from the accretion disk, or it requires a quick lateral expansion on a scale of 10^3 $r_{\rm g}$ in the case it is ergosphere–launched.

The first generation of space VLBI missions, including RadioAstron, showed that it is possible to reach truly high resolution data in the cm wavelengths on baselines exceeding out planet's diameter. However, there are some issues, like the low sensitivity of the observations, that will need to be addressed in future missions. As for the studies of AGN jets, the Event Horizon Telescope (Johnson et al., 2015) is venturing into ultra-high resolution in the mm and sub-mm wavelengths. On the other hand, long–term

programs such as the MOJAVE (Lister et al., 2018), TANAMI (Kadler et al., 2007) and the work of the Boston University Blazar Group (Jorstad & Marscher, 2016, Jorstad et al., 2017) enable us to study the evolution if these objects.

References

[1] Pauliny-Toth, I. I. K. & Kellermann, K. I.(1966): Variations in the Radio-Frequency Spectra of 3c 84, 3c 273, 3c 279, and Other Radio Sources. *Astrophysical Journal, vol. 146, p.634.*

[2] https://dept.astro.lsa.umich.edu/datasets/umrao.php This research has made use of data from the University of Michigan Radio Astronomy Observatory which has been supported by the University of Michigan and by a series of grants from the National Science Foundation, most recently AST-0607523.

[3] Jorstad, S. & Marscher, A. (2016): The VLBA-BU-BLAZAR Multi-Wavelength Monitoring Program. *Galaxies 2016, 4(4), 47.*

[4] Jorstad, S. G.; Marscher, A. P.; Morozova, D. A.; Troitsky, I. S.; Agudo, I.; Casadio, C.; Foord, Adi; G., José L.; MacDonald, N. R.; Molina, S. N.; Lähteenmäki, A.; Tammi, J.; Tornikoski, M. (2017): Kinematics of Parsec-scale Jets of Gamma-Ray Blazars at 43 GHz within the VLBA-BU-BLAZAR Program *The Astrophysical Journal, Volume 846, Issue 2, article id. 98, 35 pp.*

[5] Lister, M. L.; Aller, M. F.; Aller, H. D.; Hodge, M. A.; Homan, D. C.; Kovalev, Y. Y.; Pushkarev, A. B.; Savolainen, T. (2018): MOJAVE. XV. VLBA 15 GHz Total Intensity and Polarization Maps of 437 Parsec-scale AGN Jets from 1996 to 2017. *The Astrophysical Journal Supplement Series, Volume 234, Issue 1, article id. 12, 6 pp.*

[6] Nagai, H. ; Orienti, M.; Kino, M. ; Suzuki, K. ; Giovannini, G.; Doi, A. ; Asada, K. ; Giroletti, M. ; Kataoka, J. ; D'Ammando, F. ; Inoue, M. ; Lähteenmäki, A. ; Tornikoski, M. ; León-Tavares, J.; Kameno, S. ; Bach, U. (2012): VLBI and single-dish monitoring of 3C 84 for the period 2009-2011. *Monthly Notices of the Royal Astronomical Society: Letters, Volume 423, Issue 1, pp. L122-L126.*

[7] Nesterov, N. S.; Lyuty, V. M.; Valtaoja, E. (1995): Radio and optical evolution of the Seyfert galaxy NGC 1275. *Astronomy and Astrophysics, v.296, p.628.*

[8] Abdo et al. (2009): Fermi Discovery of Gamma-ray Emission from NGC 1275. *The Astrophysical Journal, Volume 699, Issue 1, pp. 31-39.*

[9] Suzuki, K.; Nagai, H.; Kino, M.; Kataoka, J.; Asada, K.; Doi, A.; Inoue, M.; Orienti, M.; Giovannini, G.; Giroletti, M.; Lähteenmäki, A.; Tornikoski, M.; León-Tavares, J.; Bach, U.; Kameno, S.; Kobayashi, H. (2012): Exploring the Central Sub-parsec Region of the γ-Ray Bright Radio Galaxy 3C 84 with VLBA at 43 GHz in the Period of 2002-2008. *The Astrophysical Journal, Volume 746, Issue 2, article id. 140, 9 pp.*

[10] Nagai, H.; Suzuki, K.; Asada, K.; Kino, M.; Kameno, S.; Doi, A.; Inoue, M.; Kataoka, J.; Bach, U.; Hirota, T.; Matsumoto, N.; Honma, M.; Kobayashi, H.; Fujisawa, K. (2010): VLBI Monitoring of 3C 84 (NGC 1275) in Early Phase of the 2005 Outburst. *Publications of the Astronomical Society of Japan, Vol.62, No.2, pp.L11–L15.*

[11] Nagai, H.; Haga, T.; Giovannini, G.; Doi, A.; Orienti, M.; D'Ammando, F.; Kino, M.; Nakamura, M.; Asada, K.; Hada, K.; Giroletti, M. (2014): Limb-brightened Jet of 3C 84 Revealed by the 43 GHz Very-Long-Baseline-Array Observation. *The Astrophysical Journal, Volume 785, Issue 1, article id. 53, 6 pp.*

[12] Nagai, H.; Fujita, Y.; Nakamura, M.; Orienti, M.; Kino, M.; Asada, K.; Giovannini, G. (2017):Enhanced Polarized Emission from the One-parsec-scale Hotspot of 3C 84 as a Result of the Interaction with the Clumpy Ambient Medium. *The Astrophysical Journal, Volume 849, Issue 1, article id. 52, 7 pp.*

[13] Giovannini, G.; Savolainen, T.; Orienti, M.; Nakamura, M.; Nagai, H.; Kino, M.; Giroletti, M.; Hada, K.; Bruni, G.; Kovalev, Y. Y.; Anderson, J. M.; D'Ammando, F.; Hodgson, J.; Honma, M.; Krichbaum, T. P.; Lee, S. -S.; Lico, R.; Lisakov, M. M.; Lobanov, A. P.; Petrov, L. Sohn, B. W.; Sokolovsky, K. V.; Voitsik, P. A.; Zensus, J. A.; Tingay, S. (2018): A wide and collimated radio jet in 3C84 on the scale of a few hundred gravitational radii. *Nature Astronomy, Volume 2, p. 472-477.*

[14] M. Gendron-Marsolais et al.; S. Dagnello, NRAO/AUI/NSF; Sloan Digital Sky Survey.

[15] Kardashev, N. S. et al. (2013): "RadioAstron"-A telescope with a size of 300 000 km: Main parameters and first observational results. *Astronomy Reports, Volume 57, Issue 3, pp.153-194.*

[16] Urry, C. M. & Padovani, P. (1995):Unified Schemes for Radio-Loud Active Galactic Nuclei. *Publications of the Astronomical Society of the Pacific, v.107, p.803.*

[17] Fanaroff, B. L. & Riley, J. M. (1974): The morphology of extragalactic radio sources of high and low luminosity. *Monthly Notices of the Royal Astronomical Society, Vol. 167, p. 31P-36P.*

[18] Kellermann, K. I.; Sramek, R.; Schmidt, M.; Shaffer, D. B.; Green, R. (1989): VLA Observations of Objects in the Palomar Bright Quasar Survey. *Astronomical Journal v.98, p.1195.*

[19] Du, P. ; Wang, J.–M. ; Zhang, Z.-X. (2017): Hidden Broad-line Regions in Seyfert 2 Galaxies: From the Spectropolarimetric Perspective. *The Astrophysical Journal Letters, Volume 840, Issue 1, article id. L6, 5 pp.*

[20] Mo, H.; van den Bosch, F. C.; White, S. (2010): Galaxy Formation and Evolution. *Cambridge, UK: Cambridge University Press.*

[21] Beckmann, V. & Shrader, C. R. (2012): Active Galactic Nuclei. *ISBN-13: 978-3527410781. 350 pages. Wiley-VCH Verlag GmbH*

[22] Blandford, R. D. & Rees, M. J. (1978): Extended and compact extragalactic radio sources: interpretation and theory. *Niels Bohr Institut, Teknisk Videnskabelige Forskningsrad, and*

Nordisk Institut for Teoretisk Atomfysik, Symposium on Quasars and Active Nuclei of Galaxies, Copenhagen, Denmark, June 27-July 2, 1977. Physica Scripta, vol. 17, Mar. 1978, p. 265-274.

[23] Padovani, P. & Giommi, P. (1995): The Connection between X-Ray- and Radio-selected BL Lacertae Objects. *Astrophysical Journal v.444, p.567.*

[24] Ulrich, M. H.; Maraschi, L.; Urry, C. M. (1997): Variability of active galactic nuclei. *Annu. Rev. Astron. Astrophys. 1997. 35:445–502.*

[25] VLA 20 cm image *NRAO/AUI 1999*

[26] VLA 6 cm image. *NRAO 1996.*

[27] Blandford, R. D. & Znajek, R. L. (1977): Electromagnetic extraction of energy from Kerr black holes. *Monthly Notices of the Royal Astronomical Society, Vol. 179, 433-456.*

[28] Blandford, R. D.; Netzer, H.; Woltjer, L.; Courvoisier, T. J.-L. (1990): Active Galactic Nuclei. *Mayor, M. Saas-Fee Advanced Course 20. Lecture Notes 1990. Swiss Society for Astrophysics and Astronomy, XII, 280 pp. 97 figs. Springer-Verlag Berlin Heidelberg New York*

[29] Blandford, R. D. (2001): Black Holes and Relativistic Jets. *Progress of Theoretical Physics Supplement, No. 143, pp. 182-201*

[30] Komissarov, S. S. & Porth, O. (2021): Numerical simulations of jets. *New Astronomy Reviews, Volume 92, article id. 101610.*

[31] Tchekhovskoy, A.; Narayan, R.; McKinney, J. C. (2011): Efficient generation of jets from magnetically arrested accretion on a rapidly spinning black hole. *Monthly Notices of the Royal Astronomical Society: Letters, Volume 418, Issue 1, pp. L79-L83.*

[32] Blandford, R. D. & Payne, D. G. (1982): Hydromagnetic flows from accretion disks and the production of radio jets. *Monthly Notices of the Royal Astronomical Society, Vol. 199, 883-903.*

[33] Spruit, H. C. (1996): Magnetohydrodynamic jets and winds from accretion disks. *Kluwer academic publishers. Evolutionary processes in binary stars, NATO ASI Series C., vol.477, p.249-286.*

[34] Begelman, M. C.; Blandford, R. D.; Rees, M. J. (1984): Theory of extragalactic radio sources. *Reviews of Modern Physics, Volume 56, Issue 2, April 1984, pp.255-351.*

[35] Martí, J. M. & Müller, E. (2015): Grid-based Methods in Relativistic Hydrodynamics and Magnetohydrodynamics. *Living Reviews in Computational Astrophysics, Volume 1, Issue 1, article id. 3, 182 pp.*

[36] Rayburn, D. R. (1977): A numerical study of the continuous beam model of extragalactic radio sources. *Monthly Notices of the Royal Astronomical Society, vol. 179, June 1977, p. 603-617.*

[37] Blandford, R. D.; Rees, M. J. (1974): A "twin–exhaust" model for double radio sources. *Monthly Notices of the Royal Astronomical Society, Vol. 169, 395-415.*

[38] Norman, M. L.; Winkler, K. –H. A.; Smarr, L.; Smith, M. D. (1982): Structure and dynamics of supersonic jets. *Astronomy and Astrophysics, Vol. 113, p. 285-302.*

[39] Sanders, R. H. (1983): The reconfinement of jets. *Astrophysical Journal, Vol. 266, p. 73-81.*

[40] Falle, S. A. E. G. ; Wilson, M. J. (1985): A theoretical model of the M 87 jet. *Monthly Notices of the Royal Astronomical Society, Vol. 216, 79-84.*

[41] Falle, S. A. E. G. (1991): Self-similar jets. *Monthly Notices of the Royal Astronomical Society, Vol. 250, 581-596.*

[42] Abramowicz, M.; Jaroszynski, M.; Sikora, M. (1978): Relativistic, accreting disks. *Astronomy and Astrophysics, Vol. 63, p. 221-224*

[43] Yu, Q. & Tremaine, S. (2002): Observational constraints on growth of massive black holes. *Monthly Notice of the Royal Astronomical Society, Volume 335, Issue 4, pp. 965-976.*

[44] McKinney, J. C. & Gammie, C. F. (2004): A Measurement of the Electromagnetic Luminosity of a Kerr Black Hole. *The Astrophysical Journal, Volume 611, Issue 2, pp. 977-995.*

[45] Fishbone, L. G. & Moncrief, V. (1976): Relativistic fluid disks in orbit around Kerr black holes. *Astrophysical Journal, vol. 207, Aug. 1, 1976, pt. 1, p. 962-976.*

[46] Balbus, Steven A.; Hawley, John F. (1991): A Powerful Local Shear Instability in Weakly Magnetized Disks. I. Linear Analysis. *Astrophysical Journal v.376, p.214.*

[47] Hirose, S.; Krolik, J. H.; De Villiers, J.-P.; Hawley, J. F. (2004): Magnetically Driven Accretion Flows in the Kerr Metric. II. Structure of the Magnetic Field. *The Astrophysical Journal, Volume 606, Issue 2, pp. 1083-1097.*

[48] Tchekhovskoy, A.; Narayan, R.; McKinney, J. C. (2011): Efficient generation of jets from magnetically arrested accretion on a rapidly spinning black hole. *Monthly Notices of the Royal Astronomical Society: Letters, Volume 418, Issue 1, pp. L79–L83.*

[49] Tchekhovskoy, A.; Narayan, R.; McKinney, J. C. (2010): Magnetohydrodynamic simulations of gamma-ray burst jets: Beyond the progenitor star. *New Astronomy, Volume 15, Issue 8, p. 749-754.*

[50] Gammie, C. F. (1999): Efficiency of Magnetized Thin Accretion Disks in the Kerr Metric. *The Astrophysical Journal, Volume 522, Issue 1, pp. L57-L60.*

[51] Tchekhovskoy, A. & McKinney, J. C. (2012): Prograde and retrograde black holes: whose jet is more powerful? *Monthly Notices of the Royal Astronomical Society: Letters, Volume 423, Issue 1, pp. L55-L59.*

[52] Ghisellini, G.; Tavecchio, F.; Foschini, L.; Ghirlanda, G.; Maraschi, L.; Celotti, A. (2010): General physical properties of bright Fermi blazars. *Monthly Notices of the Royal Astronomical Society, Volume 402, Issue 1, pp. 497-518.*

[53] Bisnovatyi-Kogan, G. S. & Ruzmaikin, A. A. (1974): The Accretion of Matter by a Collapsing Star in the Presence of a Magnetic Field. *Astrophysics and Space Science, Volume 28, Issue 1, pp.45-59.*

[54] Igumenshchev, I. V.; Narayan, R.; Abramowicz, M. A. (2003): Three-dimensional Magnetohydrodynamic Simulations of Radiatively Inefficient Accretion Flows. *The Astrophysical Journal, Volume 592, Issue 2, pp. 1042-1059.*

[55] Begelman, M. C. (1985): Accretion disks in active galactic nuclei. *Astrophysics of active galaxies and quasi-stellar objects . Mill Valley, CA, University Science Books, 1985, p. 411-452.*

[56] Gammie, C. F.; McKinney, J. C.; Tóth, G. (2003): HARM: A Numerical Scheme for General Relativistic Magnetohydrodynamics. *The Astrophysical Journal, Volume 589, Issue 1, pp. 444-457.*

[57] Chakrabarti, S. K. (1985): The natural angular momentum distribution in the study of thick disks around black holes. *Astrophysical Journal, Part 1 (ISSN 0004-637X), vol. 288, Jan. 1, 1985, p. 1-6.*

[58] Narayan, R.; Sądowski, A.; Penna, R. F.; Kulkarni, A. K. (2012): GRMHD simulations of magnetized advection-dominated accretion on a non-spinning black hole: role of outflows. *Monthly Notices of the Royal Astronomical Society, Volume 426, Issue 4, pp. 3241-3259.*

[59] Casse, F. & Keppens, R. (2002): Magnetized Accretion-Ejection Structures: 2.5-dimensional Magnetohydrodynamic Simulations of Continuous Ideal Jet Launching from Resistive Accretion Disks. *The Astrophysical Journal, Volume 581, Issue 2, pp. 988-1001.*

[60] Casse, F. & Keppens, R. (2004): Radiatively Inefficient Magnetohydrodynamic Accretion-Ejection Structures. *The Astrophysical Journal, Volume 601, Issue 1, pp. 90-103.*

[61] Tzeferacos, P. ; Ferrari, A. ; Mignone, A. ; Zanni, C. ; Bodo, G. ; Massaglia, S. (2009): On the magnetization of jet-launching discs. *Monthly Notices of the Royal Astronomical Society, Volume 400, Issue 2, pp. 820-834.*

[62] Porth, O. & Fendt, C. (2010): Acceleration and Collimation of Relativistic Magnetohydrodynamic Disk Winds. *The Astrophysical Journal, Volume 709, Issue 2, pp. 1100-1118.*

[63] Contopoulos, I.; Gabuzda, D.; Kylafis, N. (2015): The Formation and Disruption of Black Hole Jets. *Astrophysics and Space Science Library, Volume 414. ISBN 978-3-319-10355-6. Springer International Publishing Switzerland.*

[64] Arnold, S. (2014): Getting Started in Radio Astronomy. *Getting Started in Radio Astronomy: Beginner Projects for the Amateur, The Patrick Moore Practical Astronomy Series, ISBN 978-1-4614-8156-0. Springer Science+Business Media New York.*

[65] Wilson, T. L.; Rohlfs, K.; Hüttemeister, S. (2013): Tools of Radio Astronomy. *Astronomy and Astrophysics Library. ISBN 978-3-642-39949-7. Springer-Verlag Berlin Heidelberg.*

[66] Taylor, G. B.; Carilli, C. L.; Perley, R. A. (1999): Synthesis Imaging in Radio Astronomy II. *A Collection of Lectures from the Sixth NRAO/NMIMT Synthesis Imaging Summer School. ASP Conference Series, Vol. 180.*

[67] Perley, R. A.; Schwab, F. R.; Bridle, A. H. (1989): Synthesis imaging in radio astronomy : a collection of lectures from the third NRAO synthesis imaging summer school. *ASP Conference Series, Vol. 6, edited by Richard A. Perley, Frederic R. Schwab, and Alan H. Bridle. Published by the Astronomical Society of the Pacific, San Francisco, CA LCCN 89-83682, ISBN 0-937707-23-6.*

[68] Titov, O.; Melnikov, A.; Lopez, Y. (2020): Resolving VLBI correlator ambiguity in the time delay model improves precision of geodetic measurements. *Publications of the Astronomical Society of Australia, Volume 37, article id. e050.*

[69] Zensus, J. A.; Diamond, P. J.; Napier, P. J. (1995): Very Long Baseline Interferometry and the VLBA. *NRAO Workshop No. 22. Astronomical Society of the Pacific Conference Series, Volume 82, Proceedings of a Summer School held in Socorro, New Mexico, 23-30 June 1993, San Francisco: Astronomical Society of the Pacific (ASP).*

[70] Zensus, J. A.; Ros, E. (2014): European VLBI Network: Present and Future. *Proceeding of the 12th European VLBI Network Symposium and Users Meeting - EVN 2014, 7-10 October 2014, Cagliari, Italy. PoS(EVN 2014)001.*

[71] Tingay, S. (2003): A Possible Upgrade Path for the Australian Long Baseline Array. *New technologies in VLBI, Proceedings of a symposium of the International VLBI Service for Geodesy and Astrometry held in Gyeong-ju, Korea, 5-8 November 2002. Edited by Y.C. Minh. ASP Conference Series, Vol. 306. San Francisco, CA: Astronomical Society of the Pacific, 2003., p.361.*

[72] An, T.; Sohn, B. W.; Imai, H. (2018): Capabilities and prospects of the East Asia Very Long Baseline Interferometry Network. *Nature Astronomy, Volume 2, p. 118-125.*

[73] Johnson, Michael D.; Doeleman, Sheperd S.; Event Horizon Telescope Collaboration (2015): The Event Horizon Telescope: New Developments and Results. *IAU General Assembly, Meeting #29, id.2257792*

[74] Hirabayashi, H. et al. (1998): Overview and Initial Results of the Very Long Baseline Interferometry Space Observatory Programme. *Science, Vol. 281, Iss. 5384, p. 1825.*

[75] Sosa-Brito, Rafael M.; Tacconi-Garman, Lowell E.; Lehnert, Matthew D.; Gallimore, Jack F. (2001): Integral Field Near-Infrared Spectroscopy of a Sample of Seyfert and LINER Galaxies. I. The Data. *The Astrophysical Journal Supplement Series, Volume 136, Issue 1, pp. 61-98.*

[76] Kellermann, K. I.; Jauncey, D. L.; Cohen, M. H.; Shaffer, B. B.; Clark, B. G.; Broderick, J.; Rönnäng, B.; Rydbeck, O. E. H.; Matveyenko, L.; Moiseyev, I.; Vitkevitch, V. V.; Cooper, B. F. C.; Batchelor, R. (1971): High-Resolution Observations of Compact Radio Sources at 6 and 18 Centimeters. *Astrophysical Journal, vol. 169, p.1.*

[77] Walker, R. C.; Romney, J. D.; Benson, J. M. (1994): Detection of a VLBI Counterjet in NGC 1275: A Possible Probe of the Parsec-Scale Accretion Region. *Astrophysical Journal Letters v.430, p.L45.*

[78] Vermeulen, R. C.; Readhead, A. C. S.; Backer, D. C. (1994): Discovery of a Nuclear Counterjet in NGC 1275: A New Way to Probe the Parsec-Scale Environment. *Astrophysical Journal Letters v.430, p.L41.*

[79] Walker, R. C.; Dhawan, V.; Romney, J. D.; Kellermann, K. I.; Vermeulen, R. C. (2000): VLBA Absorption Imaging of Ionized Gas Associated with the Accretion Disk in NGC 1275. *The Astrophysical Journal, Volume 530, Issue 1, pp. 233-244.*

[80] León-Tavares, J.; Valtaoja, E.; Tornikoski, M.; Lähteenmäki, A.; Nieppola, E. (2011): The connection between gamma-ray emission and millimeter flares in Fermi/LAT blazars. *Astronomy & Astrophysics, Volume 532, id.A146.*

[81] Fujita, Y. & Nagai, H. (2017): Discovery of a new subparsec counterjet in NGC 1275: the inclination angle and the environment. *Monthly Notices of the Royal Astronomical Society: Letters, Volume 465, Issue 1, p.L94-L98.*

[82] Giovannini, G. (2003): The radio jet velocities at high resolution. *New Astronomy Reviews, Volume 47, Issue 6-7, p. 551-555.*

[83] Hovatta, T.; Valtaoja, E.; Tornikoski, M.; Lähteenmäki, A. (2009): Doppler factors, Lorentz factors and viewing angles for quasars, BL Lacertae objects and radio galaxies. *Astronomy and Astrophysics, Volume 494, Issue 2, 2009, pp.527-537.*

[84] Giroletti, M.; Giovannini, G.; Taylor, G. B.; Falomo, R. (2006): A Sample of Low-Redshift BL Lacertae Objects. II. EVN and MERLIN Data and Multiwavelength Analysis. *The Astrophysical Journal, Volume 646, Issue 2, pp. 801-814.*

[85] Piner, B. G.; Pant, N.; Edwards, P. G. (2010): The Jets of TeV Blazars at Higher Resolution: 43 GHz and Polarimetric VLBA Observations from 2005 to 2009. *The Astrophysical Journal, Volume 723, Issue 2, pp. 1150-1167.*

[86] Lister, M. L. (2001): Parsec-Scale Jet Polarization Properties of a Complete Sample of Active Galactic Nuclei at 43 GHz. *The Astrophysical Journal, Volume 562, Issue 1, pp. 208-232.*

[87] Sahayanathan, S. (2009): Boundary shear acceleration in the jet of MKN501. *Monthly Notices of the Royal Astronomical Society: Letters, Volume 398, Issue 1, pp. L49-L53.*

[88] Zakamska, N. L.; Begelman, M. C.; Blandford, R. D. (2008): Hot Self-Similar Relativistic Magnetohydrodynamic Flows. *The Astrophysical Journal, Volume 679, Issue 2, pp. 990-999.*

[89] Owen, F. N.; Hardee, P. E.; Cornwell, T. J. (1989): High-Resolution, High Dynamic Range VLA Images of the M87 Jet at 2 Centimeters. *Astrophysical Journal v.340, p.698.*

[90] Komissarov, S. S.; Vlahakis, N.; Königl, A.; Barkov, M. V. (2009): Magnetic acceleration of ultrarelativistic jets in gamma-ray burst sources. *Monthly Notices of the Royal Astronomical Society, Volume 394, Issue 3, pp. 1182-1212.*

[91] Nakamura, M. & Asada, K. (2013): The Parabolic Jet Structure in M87 as a Magnetohydrodynamic Nozzle. *The Astrophysical Journal, Volume 775, Issue 2, article id. 118, 11 pp.*

[92] Balmaverde, B.; Capetti, A.; Grandi, P. (2006): The Chandra view of the 3C/FR I sample of low luminosity radio-galaxies. *Astronomy and Astrophysics, Volume 451, Issue 1, May III 2006, pp.35-44.*

[93] Ajello, M.; Rebusco, P.; Cappelluti, N.; Reimer, O.; Böhringer, H.; Greiner, J.; Gehrels, N.; Tueller, J.; Moretti, A. (2009): Galaxy Clusters in the Swift/Burst Alert Telescope Era: Hard X-rays in the Intracluster Medium. *The Astrophysical Journal, Volume 690, Issue 1, pp. 367-388.*

[94] Reimer, O.; Pohl, M.; Sreekumar, P.; Mattox, J. R. (2003): EGRET Upper Limits on the High-Energy Gamma-Ray Emission of Galaxy Clusters. *The Astrophysical Journal, Volume 588, Issue 1, pp. 155-164.*

[95] Perkins, J. S.; Badran, H. M.; Blaylock, G.; Bradbury, S. M.; Cogan, P.; Chow, Y. C. K.; Cui, W.; Daniel, M. K.; Falcone, A. D.; Fegan, S. J.; Finley, J. P.; Fortin, P.; Fortson, L. F.; Gillanders, G. H.; Gutierrez, K. J.; Grube, J.; Hall, J.; Hanna, D.; Holder, J.; Horan, D. Hughes, S. B.; Humensky, T. B.; Kenny, G. E.; Kertzman, M.; Kieda, D. B.; Kildea, J.; Kosack, K.; Krawczynski, H.; Krennrich, F.; Lang, M. J.; LeBohec, S.; Maier, G.; Moriarty, P.; Ong, R. A.; Pohl, M.; Ragan, K.; Rebillot, P. F.; Sembroski, G. H.; Steele, D.; Swordy, S. P.; Valcarcel, L.; Vassiliev, V. V.; Wakely, S. P.; Weekes, T. C.; Williams, D. A.; VERITAS Collaboration (2006): TeV Gamma-Ray Observations of the Perseus and Abell 2029 Galaxy Clusters. *The Astrophysical Journal, Volume 644, Issue 1, pp. 148-154.*

[96] Kino, M.; Takahara, F.; Kusunose, M. (2002): Energetics of TeV Blazars and Physical Constraints on Their Emission Regions. *The Astrophysical Journal, Volume 564, Issue 1, pp. 97-107.*

[97] Finke, J. D.; Dermer, C. D.; Böttcher, M. (2008): Synchrotron Self-Compton Analysis of TeV X-Ray-Selected BL Lacertae Objects. *The Astrophysical Journal, Volume 686, Issue 1, pp. 181-194.*

[98] Georganopoulos, M. & Kazanas, D. (2003): Decelerating Flows in TeV Blazars: A Resolution to the BL Lacertae-FR I Unification Problem. *The Astrophysical Journal, Volume 594, Issue 1, pp. L27-L30.*

[99] Marscher, Alan P. (1999): The compact jets of TeV blazars. *Astroparticle Physics, Volume 11, Issue 1-2, p. 19-25.*

[100] Event Horizon Telescope Collaboration (2021): First M87 Event Horizon Telescope Results. VIII. Magnetic Field Structure near The Event Horizon. *The Astrophysical Journal Letters, Volume 910, Issue 1, id.L13, 43 pp.*

[101] Fernandes, C. A. C.; Jarvis, M. J. ; Rawlings, S. ; Martínez-Sansigre, A. ; Hatziminaoglou, E. ; Lacy, M. ; Page, M. J. ; Stevens, J. A. ; Vardoulaki, E. (2011): Evidence for a maximum jet efficiency for the most powerful radio galaxies. *Monthly Notices of the Royal Astronomical Society, Volume 411, Issue 3, pp. 1909-1916.*

[102] Hardcastle, M. (2015): Kiloparsec-Scale AGN Jets. *The Formation and Disruption of Black Hole Jets, Astrophysics and Space Science Library, Volume 414. ISBN 978-3-319-10355-6. Springer International Publishing Switzerland, 2015, p. 83*

[103] Boccardi, B.; Krichbaum, T. P.; Bach, U.; Mertens, F.; Ros, E.; Alef, W.; Zensus, J. A. (2016): The stratified two-sided jet of Cygnus A. Acceleration and collimation. *Astronomy & Astrophysics, Volume 585, id.A33, 9 pp.*

[104] Savolainen, T. (2018): RadioAstron imaging of nearby radio galaxies. *42nd COSPAR Scientific Assembly. Held 14–22 July 2018, in Pasadena, California, USA, Abstract id. E1.8–4–18.*

[105] Kovalev, Y. Y.; Lister, M. L.; Homan, D. C.; Kellermann, K. I. (2007): The Inner Jet of the Radio Galaxy M87. *The Astrophysical Journal, Volume 668, Issue 1, pp. L27-L30.*

[106] Giroletti, M.; Giovannini, G.; Feretti, L.; Cotton, W. D.; Edwards, P. G.; Lara, L.; Marscher, A. P.; Mattox, J. R.; Piner, B. G.; Venturi, T. (2004): Parsec-Scale Properties of Markarian 501. *The Astrophysical Journal, Volume 600, Issue 1, pp. 127-140.*

[107] Wagner, A. Y.; Bicknell, G. V.; Umemura, M. (2012): Driving Outflows with Relativistic Jets and the Dependence of Active Galactic Nucleus Feedback Efficiency on Interstellar Medium Inhomogeneity. *The Astrophysical Journal, Volume 757, Issue 2, article id. 136, 24 pp.*

[108] Taylor, G. B.; Gugliucci, N. E.; Fabian, A. C.; Sanders, J. S.; Gentile, G.; Allen, S. W. (2006): Magnetic fields in the centre of the Perseus cluster. *Monthly Notices of the Royal Astronomical Society, Volume 368, Issue 4, pp. 1500-1506.*

[109] Plambeck, R. L.; Bower, G. C.; Rao, R.; Marrone, D. P.; Jorstad, S. G.; Marscher, A. P.; Doeleman, S. S.; Fish, V. L.; Johnson, M. D. (2014): Probing the Parsec-scale Accretion Flow of 3C 84 with Millimeter Wavelength Polarimetry. *The Astrophysical Journal, Volume 797, Issue 1, article id. 66, 6 pp.*

[110] Narayan, R. & Yi, I. (1995): Advection-dominated Accretion: Self-Similarity and Bipolar Outflows. *Astrophysical Journal v.444, p.231.*

[111] Merloni, A. & Fabian, A. C. (2002): Coronal outflow dominated accretion discs: a new possibility for low-luminosity black holes? *Monthly Notices of the Royal Astronomical Society, Volume 332, Issue 1, pp. 165-175.*

[112] Fujita, Y.; Kawakatu, N.; Shlosman, I.; Ito, H. (2016): The young radio lobe of 3C 84: inferred gas properties in the central 10 pc. *Monthly Notices of the Royal Astronomical Society, Volume 455, Issue 3, p.2289-2294.*

[113] Osterbrock, D. E. (1991): Active galactic nuclei. *Reports on Progress in Physics, Volume 54, Issue 4, pp. 579-633.*

[114] O'Sullivan, S. P. & Gabuzda, D. C. (2009): Magnetic field strength and spectral distribution of six parsec-scale active galactic nuclei jets. *Monthly Notices of the Royal Astronomical Society, Volume 400, Issue 1, pp. 26-42.*

[115] Deller, A. T.; Tingay, S. J.; Bailes, M.; West, C. (2007): DiFX: A Software Correlator for Very Long Baseline Interferometry Using Multiprocessor Computing Environments. *The Publications of the Astronomical Society of the Pacific, Volume 119, Issue 853, pp. 318-336.*

[116] Deller, A. T.; Brisken, W. F.; Phillips, C. J.; Morgan, J.; Alef, W.; Cappallo, R.; Middelberg, E.; Romney, J.; Rottmann, H.; Tingay, S. J.; Wayth, R. (2011): DiFX-2: A More Flexible, Efficient, Robust, and Powerful Software Correlator. *Publications of the Astronomical Society of the Pacific, Volume 123, Issue 901, pp. 275.*

[117] Bruni, G. ; Anderson, J. ; Alef, W. ; Rottmann, H. ; Lobanov, A.; Zensus, J. (2016): The RadioAstron Dedicated DiFX Distribution. *Galaxies, vol. 4, issue 4, p. 55.*

[118] Lavochkin Association

[119] Greisen, E. W. (2003): AIPS, the VLA, and the VLBA. *Information Handling in Astronomy - Historical Vistas. Edited by André Heck, Strasbourg Astronomical Observatory, France. Astrophysics and Space Science Library, Vol. 285. Dordrecht: Kluwer Academic Publishers, 2003., p.109.*

[120] AIPS Cookbook, *NRAO 2020.* Available at: http://www.aips.nrao.edu/CookHTML/CookBook.html

[121] Lee, S.-S. Byun, D.-Y.; Oh, C. S.; Kim, H. R.; Kim, J.; Jung, T.; Oh, S.-J.; Roh, D.-G.; Jung, D.-K.; Yeom, J.-H. (2015): Amplitude Correction Factors of Korean VLBI Network Observations. *Journal of the Korean Astronomical Society, vol. 48, no. 5, pp. 229-236*

[122] Shepherd, M. C. (1997): Difmap: an Interactive Program for Synthesis Imaging. *Astronomical Data Analysis Software and Systems VI, A.S.P. Conference Series, Vol. 125, 1997, Gareth Hunt and H. E. Payne, eds., p. 77.*

[123] Högbom, J. A. (1974): Aperture Synthesis with a Non-Regular Distribution of Interferometer Baselines. *Astronomy and Astrophysics Supplement, Vol. 15, p.417.*

[124] https://www.atnf.csiro.au/computing/software/miriad/userguide/node100.html

[125] Schwarz, U. J. (1978): Mathematical-statistical Description of the Iterative Beam Removing Technique (Method CLEAN). *Astronomy and Astrophysics, Vol. 65, p. 345.*

[126] Thompson, A. Richard; Moran, James M.; Swenson, George W., Jr. (2017): Interferometry and Synthesis in Radio Astronomy. *Interferometry and Synthesis in Radio Astronomy, 3rd ed. Springer.*

[127] Kogan, L. (1996): Global Ground VLBI Network as a Tied Array for Space VLBI. *VLBA Scientific Memo.*

[128] Martí-Vidal, I. & Marcaide, J. M. (2008): Spurious source generation in mapping from noisy phase-self-calibrated data. *Astronomy and Astrophysics, Volume 480, Issue 1, March II 2008, pp.289-295.*

[129] Petrov, L.; Kovalev, Y. Y.; Fomalont, E. B.; Gordon, D. (2011): The Very Long Baseline Array Galactic Plane Survey—VGaPS. *The Astronomical Journal, Volume 142, Issue 2, article id. 35, 23 pp.*

[130] Kellermann, K. I. ; Lister, M. L. ; Homan, D. C. ; Vermeulen, R. C. ; Cohen, M. H. ; Ros, E. ; Kadler, M. ; Zensus, J. A. ; Kovalev, Y. Y. (2004): Sub-Milliarcsecond Imaging of Quasars and Active Galactic Nuclei. III. Kinematics of Parsec-scale Radio Jets. *The Astrophysical Journal, Volume 609, Issue 2, pp. 539-563.*

[131] Asada, K. & Nakamura, M. (2012): The Structure of the M87 Jet: A Transition from Parabolic to Conical Streamlines. *The Astrophysical Journal Letters, Volume 745, Issue 2, article id. L28, 5 pp.*

[132] A Janssen, M., Falcke, H., Kadler, M. (2021): Event Horizon Telescope observations of the jet launching and collimation in Centaurus A. *Nat Astron*

[133] Nakahara, S. ; Doi, A. ; Murata, Y. ; Hada, K. ; Nakamura, M.; Asada, K. (2018): Finding Transitions of Physical Condition in Jets from Observations over the range of 10^3–10^9 Schwarzschild Radii in Radio Galaxy NGC 4261. *The Astrophysical Journal, Volume 854, Issue 2, article id. 148, 11 pp.*

[134] Tseng, C.–Y.; Asada, K.; Nakamura, M. ; Pu, H.–Y.; Algaba, J.–C. ; Lo, W.–P. (2016): Structural Transition in the NGC 6251 Jet: an Interplay with the Supermassive Black Hole and Its Host Galaxy. *The Astrophysical Journal, Volume 833, Issue 2, article id. 288, 8 pp.*

[135] Tavecchio, F. & Ghisellini, G. (2014): On the spine–layer scenario for the very high-energy emission of NGC 1275. *Monthly Notices of the Royal Astronomical Society, Volume 443, Issue 2, p.1224-1230.*

[136] Scharwächter, J. ; McGregor, P. J. ; Dopita, M. A. ; Beck, T. L. (2013): Kinematics and excitation of the molecular hydrogen accretion disc in NGC 1275. *Monthly Notices of the Royal Astronomical Society, Volume 429, Issue 3, p.2315-2332.*

[137] Dominik, Rune M. ; Linhoff, L.; Elsässer, D. ; Rhode, W. (2021): 3C 84: a possibly precessing jet in 43-GHz observations. *Monthly Notices of the Royal Astronomical Society, Volume 503, Issue 4, pp.5448-5454.*

[138] Britzen, S. ; Fendt, C.; Zajaček, M. ; Jaron, F. ; Pashchenko, I. ; Aller, M. F. ; Aller, H. D. (2019): 3C 84: Observational Evidence for Precession and a Possible Relation to TeV Emission. *Galaxies, vol. 7, issue 3, p. 72.*

[139] Katz, J. I. (1997): A Precessing Disk in OJ 287? *The Astrophysical Journal, Volume 478, Issue 2, pp. 527-529.*

[140] Pringle, J. E. (1997): Self-induced warping of accretion discs: non-linear evolution and application to AGN. *Monthly Notices of the Royal Astronomical Society, Volume 292, Issue 1, pp. 136-147.*

[141] Kino, M. ; Wajima, K. ; Kawakatu, N. ; Nagai, H.; Orienti, M.; Giovannini, G.; Hada, K.; Niinuma, K. ; Giroletti, M. (2018): Evidence of Jet-Clump Interaction: A Flip of the Radio Jet Head of 3C 84. *The Astrophysical Journal, Volume 864, Issue 2, article id. 118, 9 pp. (2018).*

[142] Wagner, A. Y.; Bicknell, G. V. (2011): Relativistic Jet Feedback in Evolving Galaxies. *The Astrophysical Journal, Volume 728, Issue 1, article id. 29, 9 pp.*

[143] Savolainen, T.; Wiik, K. ; Valtaoja, E. ; Jorstad, S. G. ; Marscher, A. P. (2002): Connections between millimetre continuum variations and VLBI structure in 27 AGN. *Astronomy and Astrophysics, v.394, p.851-861.*

[144] Kellermann, K. I. & Pauliny-Toth, I. I. K. (1969): The Spectra of Opaque Radio Sources. *Astrophysical Journal, vol. 155, p.L71.*

[145] Readhead, A. C. S. (1994): Equipartition Brightness Temperature and the Inverse Compton Catastrophe. *Astrophysical Journal v.426, p.51.*

[146] Wright, E. L. (2006): A Cosmology Calculator for the World Wide Web. *The Publications of the Astronomical Society of the Pacific, Volume 118, Issue 850, pp. 1711-1715.*

[147] Nakamura, M.; Asada, K.; Hada, K.; Pu, H.–Y.; Noble, S.; Tseng, C.; Toma, K.; Kino, M.; Nagai, H.; Takahashi, K.; Algaba, J.–C.; Orienti, M.; Akiyama, K.; Doi, A.; Giovannini, G.; Giroletti, M.; Honma, M.; Koyama, S.; Lico, .; Niinuma, K.; Tazaki, F. (2018): Parabolic

Jets from the Spinning Black Hole in M87. *The Astrophysical Journal, Volume 868, Issue 2, article id. 146, pp.*

[148] Blandford, R. D. & Begelman, M. C. (1999): On the fate of gas accreting at a low rate on to a black hole. *Monthly Notices of the Royal Astronomical Society, Volume 303, Issue 1, pp. L1-L5.*

[149] Blandford, R. D. & Begelman, M. C. (2004): Two-dimensional adiabatic flows on to a black hole – I. Fluid accretion. *Monthly Notices of the Royal Astronomical Society, Volume 349, Issue 1, pp. 68-86.*

[150] Ulvestad, J. S. (2000): The ARISE space VLBI mission. *Adv. SPace Res. 26, 735–738.*

[151] Murphy, D. ; Preston, R. ; Fomalont, E. ; Romney, J. ; Ulvestad, J. ; Greenhill, L. ; Reid, M. (2005): iARISE: A Next-Generation Two-Spacecraft Space VLBI Mission Concept. *Future Directions in High Resolution Astronomy: The 10th Anniversary of the VLBA, ASP Conference Proceedings, Vol. 340. Edited by J. Romney and M. Reid. San Francisco: Astronomical Society of the Pacific, 2005., p.575*

[152] Hagiwara, Y. ; Fomalont, E. ; Tsuboi, M. ; Yasuhiro, M. (2009): Approaching Micro-Arcsecond Resolution with VSOP-2: Astrophysics and Technologies. *Approaching Micro-Arcsecond Resolution with VSOP-2: Astrophysics and Technologies ASP Conference Series, Vol. 402, proceedings of the conference held 3-7 December, 2007, at ISAS/JAXA, Sagamihara, Kanagawa, Japan. Edited by Yoshiaki Hagiwara, Ed Fomalont, Masato Tsuboi, and Yasuhiro Murata.*

[153] Kadler, M.; Ojha, R. ; Tingay, S.; Lovell, J. ; TANAMI Collaboration (2007): The TANAMI Program: Southern-Hemisphere VLBI Monitoring of Relativistic Jets in Active Galaxies. *American Astronomical Society, AAS Meeting #211, id.04.13; Bulletin of the American Astronomical Society, Vol. 39, p.732*